UCRL-TR-211853

LAWRENCE
LIVERMORE
NATIONAL
LABORATORY

Laser Program Annual Report - 1979 Unclassified Excerpts

J. D. Lindl

April 29, 2005

Disclaimer

This work was performed under the auspices of the U.S. Department of Energy by University of California, Lawrence Livermore National Laboratory under Contract W-7405-Eng-48.

Laser Program
Annual Report - 1979 (U)
Excerpts

Scientific Editor: Lamar W. Coleman

General Editor: John R. Strack

Manuscript date: November 1980

LAWRENCE LIVERMORE LABORATORY
University of California • Livermore, California • 94550

Excerpts From The 1979 ICF Annual Report

Pages 1-1 through 1-4

Pages 2-10 through 2-14

Pages 2-28 through 2-30

Pages 2-37 through 2-46

Pages 4-8 through 4-11

Pages 5-1 through 5-31

Pages 5-62 through 5-88

Pages 5-91 through 5-96

These pages have been cited as unpublished references in the Book "Inertial Confinement Fusion" by John D. Lindl. They are reprinted here for the convenience of the reader.

"Inertial Confinement Fusion" citations that pertain to the 1979 Annual Report are:
Chapter 2, references 34,37,41,43,50
Chapter 3, references 7,11
Chapter 7, reference 3
Chapter 10, reference 2
Chapter 11, reference 3
Chapter 13, reference 6.

Laser Program Overview

1

The objective of the Lawrence Livermore National Laboratory (LLNL) Inertial Confinement Fusion (ICF) program is to demonstrate the scientific feasibility of ICF for military applications (to develop and utilize the capability to study nuclear weapons physics in support of the weapons program) and for energy-directed uses in the civilian sector. The demonstration of scientific feasibility for both military and civilian objectives will require achieving gains on the order of 10 to 100 in fusion microexplosions. Our major near-term milestones include the attainment of high compression, one-hundred to one-thousand times (100 to 1000×) liquid D-T density in the thermonuclear fuel and ignition of thermonuclear burn.

In 1979, our laser fusion experiments and analysis programs focused on two important areas related to achieving this goal: conducting x-ray-driven implosions of a variety of D-T-filled fuel capsules to unprecedented high densities ($\lesssim$50× liquid D-T density) and the determination of the scaling of hot electrons and thermal radiation in hohlraums.

By operating the Shiva facility in the short-pulse (100 ps), high-power (20 to 30 TW) regime, we achieved final fuel densities of 10 to 20× with directly irradiated electron conduction-driven targets. The density was diagnosed by x-ray imaging and neutron-activation techniques. Increasing the pulse length to ~1 ns and focusing 8 to 12 kJ into miniature high-Z hohlraums, x-radiation driven, plastic-coated, D-T-filled glass microspheres have attained fuel densities in excess of 50× liquid D-T density. Experiments performed in late 1979 and evaluated in early 1980, using an improved, double-shell Apollo target, have achieved densities in excess of 100×. In all cases, the final compressed state was determined by use of our radiochemistry techniques. Figure 1-1 shows our ICF results on the

Fig. 1-1. Fuel density at burn time versus neutron yield for experiments on the Shiva laser.

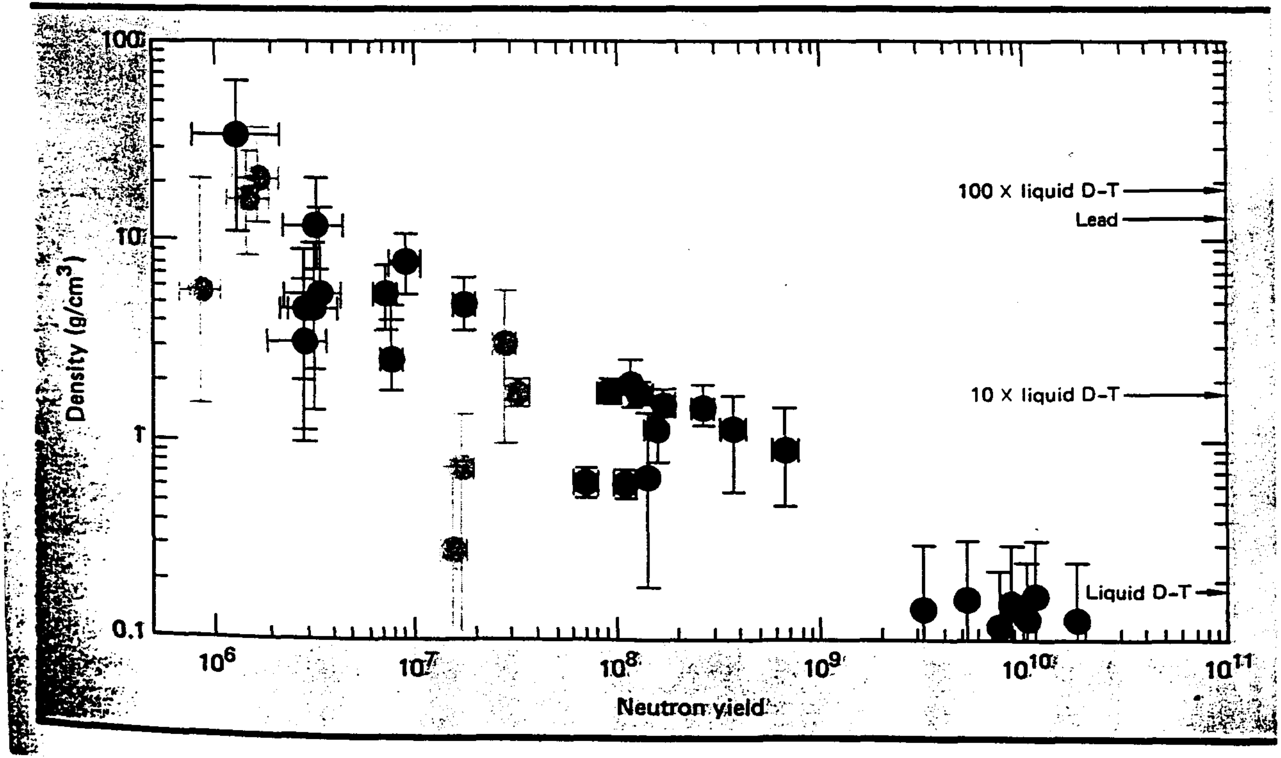

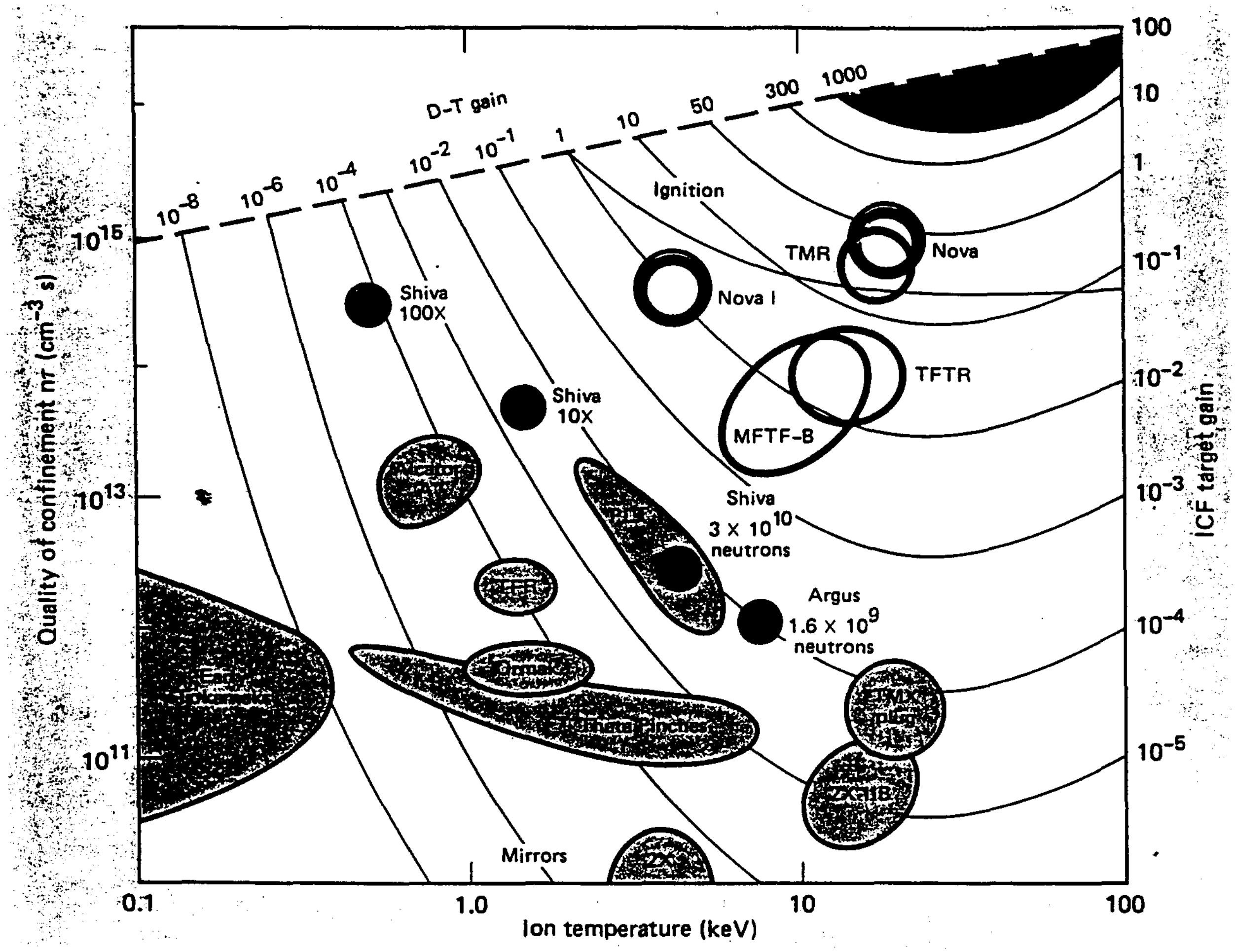

Fig. 1-2. Thermonuclear conditions achieved in fusion experiments.

Shiva laser plotted as a function of final compressed density and neutron yield (the latter being strongly dependent on D-T temperature). The slope of the line is the boundary of attainable conditions with the Shiva laser. Operating at 20 to 30 TW and 100-ps pulses, exploding pusher targets have obtained 3×10^{10} neutrons and 5 to 6 keV ion temperature, albeit at the expense of final fuel density. The other extremes are the 100X, ~0.5-keV experiments discussed above. The various colors represent various hohlraum and direct-irradiation targets.

We made important progress in understanding and predicting the processes involved in producing the plasma conditions in our miniature hohlraums. Measurements of the radiation temperature and diagnostic hole closure, and hot electron and x-ray preheat experiments, as well as initial experiments designed to measure the ablation pressure, are in good agreement with theoretical models. We also performed a variety of experiments designed to determine the origin and scaling of hohlraum suprathermal electrons. The effects of confinement of the plasma generated in the hohlraum, laser-pulse duration, hohlraum size, and incident laser energy on the hot electron environment were all studied, and a scaling model has been developed.

The 200- to 300-kJ Nova facility, now under construction, is expected to move us into the region of ignition and the possible achievement of gains as high as unity. The conditions we expect to achieve with Nova are presented in Fig. 1-2, which shows quality of confinement (density × confinement time) and D-T ion temperature for various fusion experiments. The Nova facility will have 20 beams emanating from 46-cm-diam phosphate glass disk amplifiers. In this configuration, Nova will produce about 300 kJ at 3 ns. The full facility has been authorized by Congress as a two-phase $195M line

Fig. 1-3. Ignition margin is enhanced by Nova harmonic conversion.

Input = 150 kJ
yield = 400 kJ

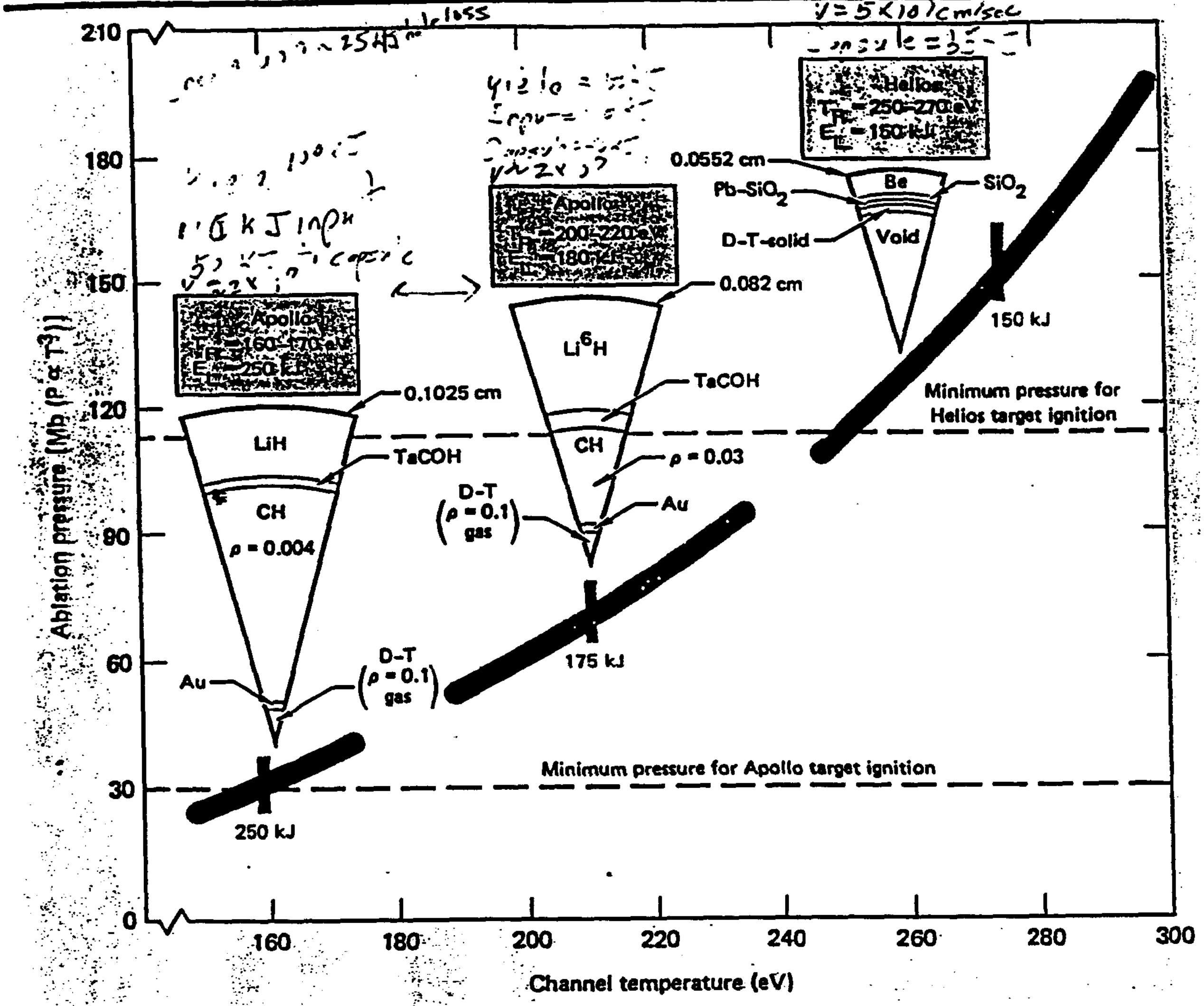

item, and at the present rate of funding, we anticipate completion by 1985.

Theoretical calculations predict that absorption of laser light increases dramatically with decreasing laser wavelength. Other effects, such as the generation of hot electrons, also improve as the wavelength decreases. We have begun a series of experiments at Argus at 0.53 μm (2ω) wavelength to study and quantify this wavelength scaling. Consequently, we have requested DOE to approve funds to add second- and third-harmonic capability to the Nova system. The importance of this flexibility is demonstrated by Figs. 1-3 and 1-4, which show the wavelength dependence of target gain and performance, as well as the fraction of energy in hot electrons that are generated while heating a miniature hohlraum to 160 eV.

Author: E. Storm

Fig. 1-4. Fraction of energy into suprathermals vs laser energy for a hohlraum-drive temperature of 160 eV.

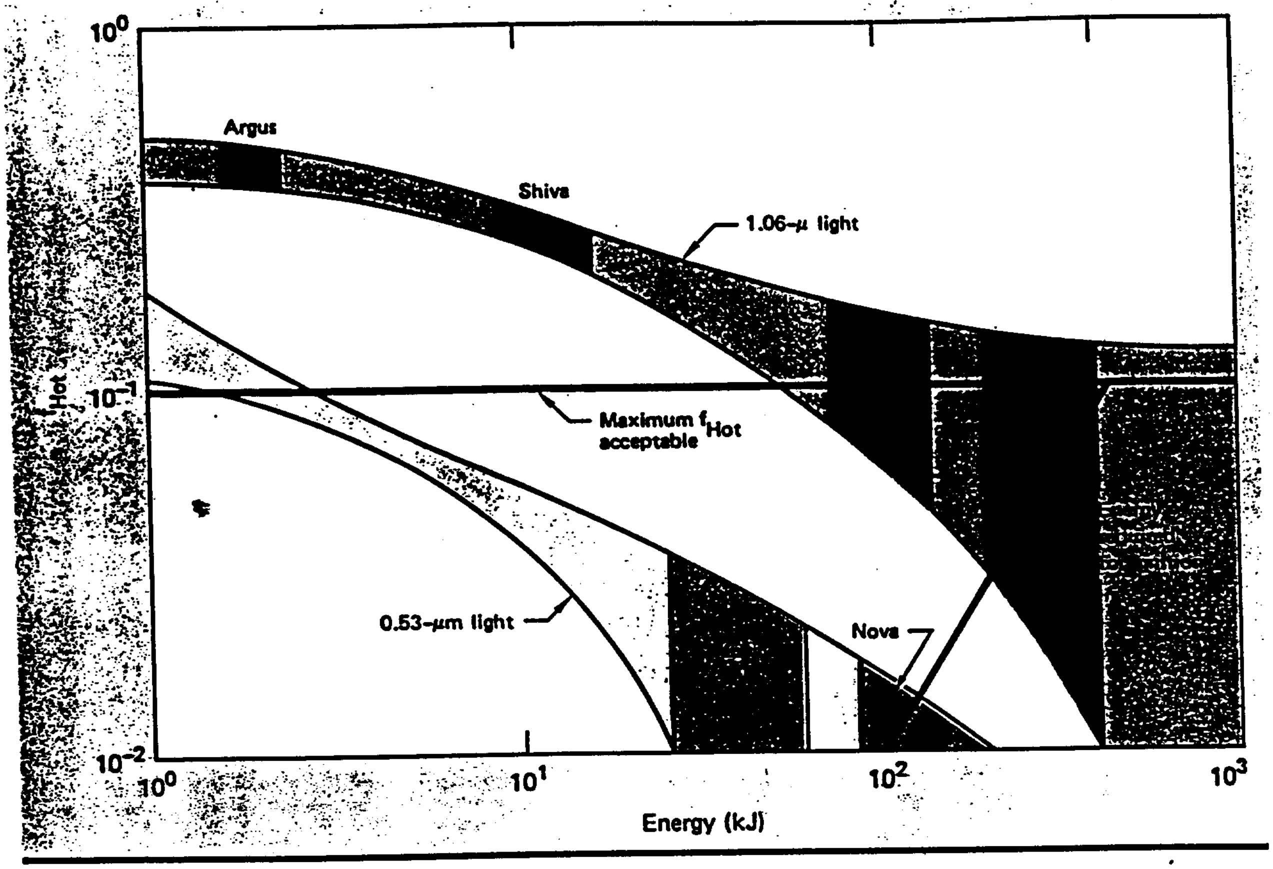

Reactor Target Gain and Symmetry Calculations

We have examined, first, the impact of various non-ideal effects on achieving the ignition conditions required for different inertial confinement fusion (ICF) targets and, second, the impact of these effects on the gain obtained from such targets. We have also studied the effects of various geometries and numerical transport techniques on implosion symmetry.

In earlier work,[2-4] we discussed calculations of the gain possible from reactor-scale single- and double-shell targets driven by short-wavelength (λ about 0.25 μm) lasers. Similar kinds of targets can be imploded with a heavy-ion driver. Figure 2-18 is a canonical double-shell target. A single-shell target would have a very similar outer shell structure but

Fig. 2-18. Sector of a high-gain double-shell target with split-fuel mass.

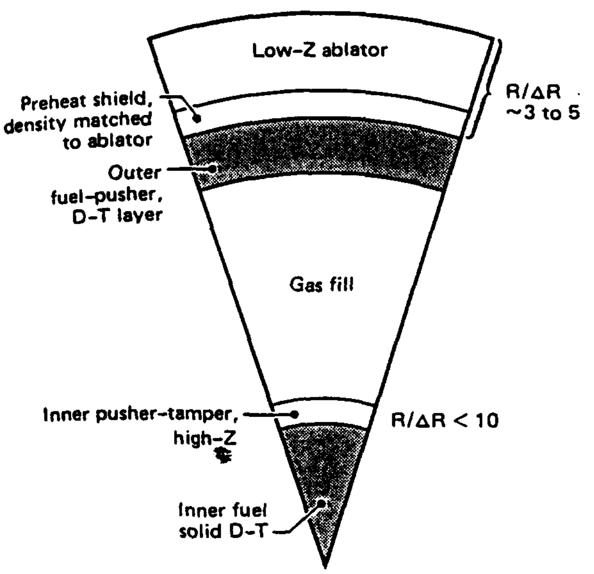

Fig. 2-19. Target gain as a function of driving energy for single- and double-shell targets.

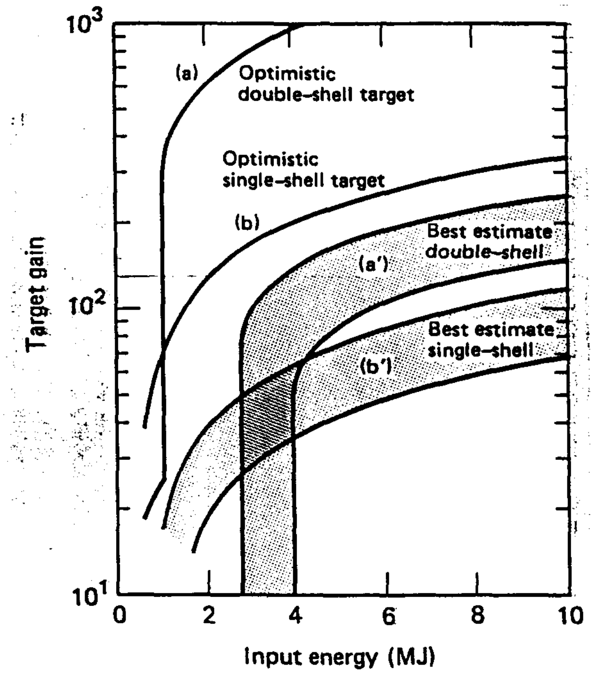

no central igniter. Such targets can be driven either by direct illumination or by first converting the laser energy into soft x rays on a high-Z radiation case and then using these x rays to drive the ablation process. The x-ray-driven approach is currently favored, largely because of symmetry considerations. If we use wide vacuum channels and an appropriate geometry, smoothing occurs for both small-scale ripple on the beams and for large-scale variations caused by laser-beam geometry effects. In the direct-illumination approach, achieving the required symmetry will probably require a sequential variety of wavelengths with long wavelengths of about 2 μm used early in the pulse and short wavelengths used during the high-power end of the pulse. Most of the detailed design work on reactor targets has been for the x-radiation-driven approach.

Calculating Gains for Single- and Double-Shell Targets

The gain data obtained for these two types of targets was based on 1-D LASNEX computer calculations with marginal fuel-ignition conditions and is shown in Fig. 2-19. For these calculations, a KrF laser ($\lambda = 0.25\,\mu m$) was absorbed on a spherical uranium-gold case with a radius 2.4 times that of the capsule. Under these assumptions, absorption is essentially 100% and about 75% of the incident laser energy couples to this capsule. Although optimized designs for direct illumination were not done, similar gains would be expected.

Single- and double-shell targets have fundamentally different ignition modes, which result in the different shapes for the gain curves. In a single-shell design, a very precise pulse shape is used to produce high entropy near the inner surface of the fuel region while keeping the majority (≥99%) of the fuel within a factor of two of the Fermi degenerate pressure. The dense fuel then acts as a pusher to compress and heat the fuel near the inner surface and to ignite a propagating burn into the majority of the fuel. The double-shell target makes use of the velocity multiplication occurring during the collision of the shells to reduce the outer-shell velocity required for ignition.

The high-Z inner pusher also acts to contain radiation from the fuel, which thereby lowers the temperatures required for ignition. These two combined effects result in a three- to four-fold improvement in peak gain for the double shell. The outer fuel in a double shell ignites as a result of a shock propagated through the high-Z pusher when the central fuel burns. However, the final imploded state of double-shell fuel regions must satisfy two requirements that result in an energy threshold for achieving high gain. First, the igniter must have enough yield to ignite a $\rho r \lesssim 0.5$ in the outer fuel. Second, the outer fuel must have a $\rho r \geqslant 1$ for good burn efficiency. Below the break in the curve for double-shell targets (see Fig. 2-19), these two conditions cannot be satisfied simultaneously and only the inner fuel ignites. Below this energy, the peak gain from single-shell targets exceeds that of double-shell targets. The energy at which this break occurs is design dependent. For example, with increased power late in the pulse, outer fuel compression and ρr could be increased so that the minimum ρr required might be achieved with less fuel and laser energy.

Curves (a) and (b) of Fig. 2-19 represent the upper limit to gains expected for these classes of targets. Although it may be possible to eventually approach these gains, a variety of non-ideal effects will probably increase the required driving energy and reduce the calculated yield. The requirement for increased driving energy can come from a variety of defects that are hard to model in a computer simulation. These include:

- Fabrication and assembly defects.
- Fluid instability.
- Imperfect implosion symmetry.

A reduction in yield can come from a mix of high-Z pusher material with the D-T fuel, an effect which lowers burn efficiency.

Increasing Implosion Symmetry

Because of their large convergence ratio, inertial-fusion capsules require 1% or better spatial uniformity of the implosion. Several techniques are available for improving implosion symmetry. Capsule shimming, in which capsule dimensions are varied to counteract impressed asymmetries of the driver, is primarily useful for long-wavelength non-uniformity. For direct illumination targets, electron-conduction smoothing can reduce short-wavelength perturbations. Our calculations indicate[5,6] that if the critical surface is maintained at a radius twice that of the ablation surface, conduction will smooth variations of ±10% in laser intensity. Such variations might arise because of beam irregularity or from non-uniformity of beam overlap in multibeam systems. Maintaining this 2:1 ratio early in time requires use of wavelengths longer than the 0.25-μm light assumed for the later high-power part of the pulse. The early part of the implosion could require wavelengths of 2 to 4 μm with shifts to shorter wavelengths occurring as the low-density corona develops.

With the radiation-driven approach, we know that case geometry, ratio of case-to-ball radii, and a variety of absorbing foils between the laser and the capsule can effectively modify the implosion symmetry. Results of detailed calculations using this approach follow.

Capsule shimming, electron conduction smoothing, or increased case-to-capsule radii and absorbing foils all result in increased driving energy. Shimming generally increases target mass without increasing fuel mass. Long-wavelength lasers have a lower ablation efficiency[6–7] than short-wavelength lasers. Increasing the case-to-ball radius increases the case losses. Absorbing foils increase heat capacity. The use of any of these techniques to produce a symmetric implosion would result in a 25 to 50% increase in driving energy or increased complexity for the driver and target factory.

For double-shell targets, the boundaries between the inner gold pusher and both the igniter and main fuel are hydrodynamically unstable during the implosion. The main fuel-pusher boundary is unstable during acceleration of the pusher. The mix that can occur reduces the calculated yield. The boundary between the igniter and the pusher is unstable during deceleration of the pusher by the igniter. The resulting mix here can cause radiative cooling of the igniter. This either prevents its ignition or results in ignition of such a small fraction that there is insufficient yield to ignite the main fuel.

In one-dimensional calculations, the igniter fuel continues being heated as long as the PdV work being done on the fuel by the pusher exceeds the radiation losses and electron-conduction losses from the fuel. For reactor-size capsules, the PdV work exceeds these losses up until the time the pusher has almost stopped. If the capsule just exceeds the ignition threshold, it will ignite at this point. On the other hand, the pusher-igniter fuel interface becomes unstable as soon as the pusher starts decelerating. In a worst case for the Rayleigh–Taylor instability, spikes of material in the pusher will penetrate the fuel (instead of being decelerated by the fuel) as soon as the fuel pressure exceeds that generated by the pusher. Such an event could occur if large amplitude perturbations are fed to the inside surface of the pusher from the outside surface.

The projection of the pusher location that is based on its peak velocity is called the fall line. By the time this trajectory has reached 0.80 of the fuel-pusher interface in one-dimension (1-D), half of the fuel could be mixed with the pusher. If the fuel has not ignited by this time, serious degradation of the igniter yield is possible. To achieve ignition after this time, one must rely on the finite growth time of the Rayleigh–Taylor instability and on having a very small amplitude of perturbations fed through from the outside of the pusher. To achieve the earlier time and more conservative ignition condition requires about a two-fold increase in driving energy over that for marginal ignition.

The outside surface of the gold pusher is unstable during its acceleration by the main fuel. Gold when mixed into the outer fuel region reduces the calculated gain, because the fuel mixed with high-Z material is radiatively cooled and burns inefficiently. Calculations indicate a 10 to 50% reduction in yield from this effect. Here one must rely on the finite growth times of the Rayleigh–Taylor instability or the effect could be even larger. For instance, if an amplitude as large as 1 to 10 μm were fed through the main fuel region from the ablator, the effective amplitude on the gold would be 0.1 to 1 μm. This amplitude is large enough to cause total penetration of the gold and probable target failure. On the other hand, low Z liners on this pusher, or pushers of lower-Z material might result in a capsule which gives full calculated yield. The effect of fluid instabilities clearly has a large impact on attainable target gain and will require substantial study. Here again, there is some corroborative evidence from the weapons program. Devices that have an outer fuel region often give lower than calculated yield, with reductions being as large as twofold.

Energy Penalty Incurred to Achieve Symmetry

If one (a) includes a 50% penalty on driving energy for symmetry, (b) requires ignition before the fall line reaches 0.8 of the pusher-igniter interface, and (c) reduces yield to 70% of the calculated value, the resulting double-shell-capsule gains for a variety of drivers will fall within the conservative band (a') in Fig. 2-19.

For single shells, the energy penalty incurred to achieve symmetry is about the same as for a double-shell target. The margin of safety required for ignition is less straightforward. If ignition occurs, the calculated yield should be close to the actual yield because no high-Z mix problem is present. To achieve the 1-D marginal ignition gains, we must control the pulse shape to about 1% in power or timing. Also, less than 1% of the fuel mass ignites for a ρr of about 0.5 g/cm^2. To relax these stringent requirements on pulse-shape accuracy to about 10% with a larger ρr igniting will require about a two-fold increase in energy. This results in the conservative band (b') shown in Fig. 2-19. Capsules driven by UV light from a KrF laser are expected to have gains near the top of the band. Gains from longer wavelength laser-driven capsules would fall lower in the band. Improved understanding of the factors affecting the drive that is required for ignition, symmetry, and yield may enable us to approach the ideal double-shell gain curves in Fig. 2-19.

Gains expected from double-shell capsules driven with heavy ions also fall within the band. Gains for such a driver depend on the ion kinetic energy (range), focal spot size, and total beam energy. For example, a beam of 10-GeV heavy ions focused to a 5-mm spot directed at such a target should produce gains near the lower edge of the band at an input energy of 4 MJ. Reducing the kinetic energy or the spot size or raising the total energy would place the expected gain higher in the band.

We have examined some 2-D symmetry questions for reactor-size ICF targets driven by 0.25-μm-wavelength laser light. The least complicated design that uses an Apollo[4] double-shell capsule is shown in Fig. 2-20. The double-shelled, radiation-driven Apollo capsule is placed at the center of a spherical hohlraum. A conical bundle of laser pulses enters the hohlraum through a hole at each pole of the spherical case. Initially, the laser light is absorbed in a band around the equator of the case. The hot equatorial band is the source of radiation that fills the hohlraum and drives the capsule by ablating its outer layer. Stringent conditions on spherical symmetry are required to achieve the high compression necessary for efficient thermonuclear burn. The localization of the radiation source translates to an asymmetric flux on the ablator surface and, hence, an asymmetric ablation pressure. We have examined the magnitude of this asymmetry, the method by which LASNEX calculates the asymmetry, and ways to minimize the asymmetry.

Fig. 2-20. Schematic of an Apollo double-shell reactor target.

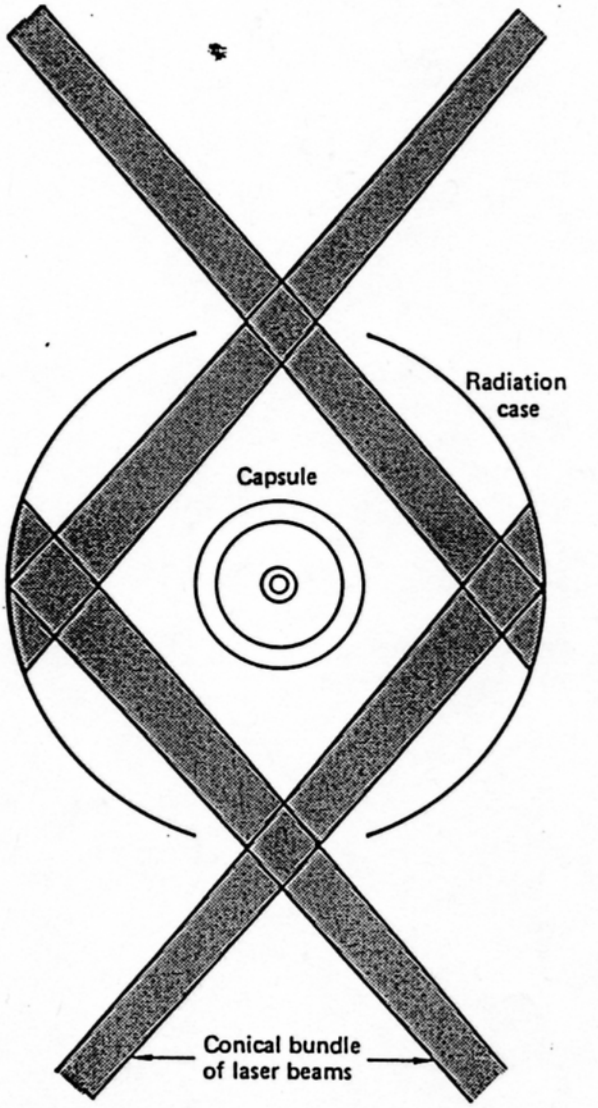

Radiation-Driven Targets for Heavy-Ion Fusion

Radiation-driven targets offer a number of advantages for heavy-ion fusion. The most obvious advantage is symmetrization by radiation flow. So far, however, all radiation-driven targets still require beam irradiation from at least two sides to obtain sufficient symmetry. A typical target concept is illustrated in Fig. 2-33(a). In an alternative concept, both beams come from one side [see Fig. 2-33(b)]. Here, the 3-D aspects present calculational difficulties, but the concept is in principle possible. The main reason for considering such a possibility is that it may simplify accelerator and reactor design. For example, a schematic of a typical unclassified induction linac is shown in Fig. 2-34(a). By using the illumination scheme shown in Fig. 2-33(b), we can eliminate the high-current bends, thereby simplifying design and reducing costs [see Fig. 2-34(b)].

Other advantages of the radiation-driven approach are the insensitivity to variations in beam uniformity and details of ion-energy deposition. The principal disadvantage is the loss of energy associated with radiation conversion and absorption in the hohlraum walls.

For any radiation approach to be feasible, high conversion efficiency from beam energy to thermal x rays is necessary. This requirement imposes certain constraints on ion-beam parameters. The conversion efficiency, η, must satisfy the inequality,

$$\eta < \frac{E_b - E_c}{E_b} = \frac{\epsilon_b - \epsilon_c}{\epsilon_b} \quad , \tag{3}$$

Fig. 2-33. Two target design concepts for irradiation of capsule. (a) Beam irradiation from two sides. (b) Beam irradiation from one side.

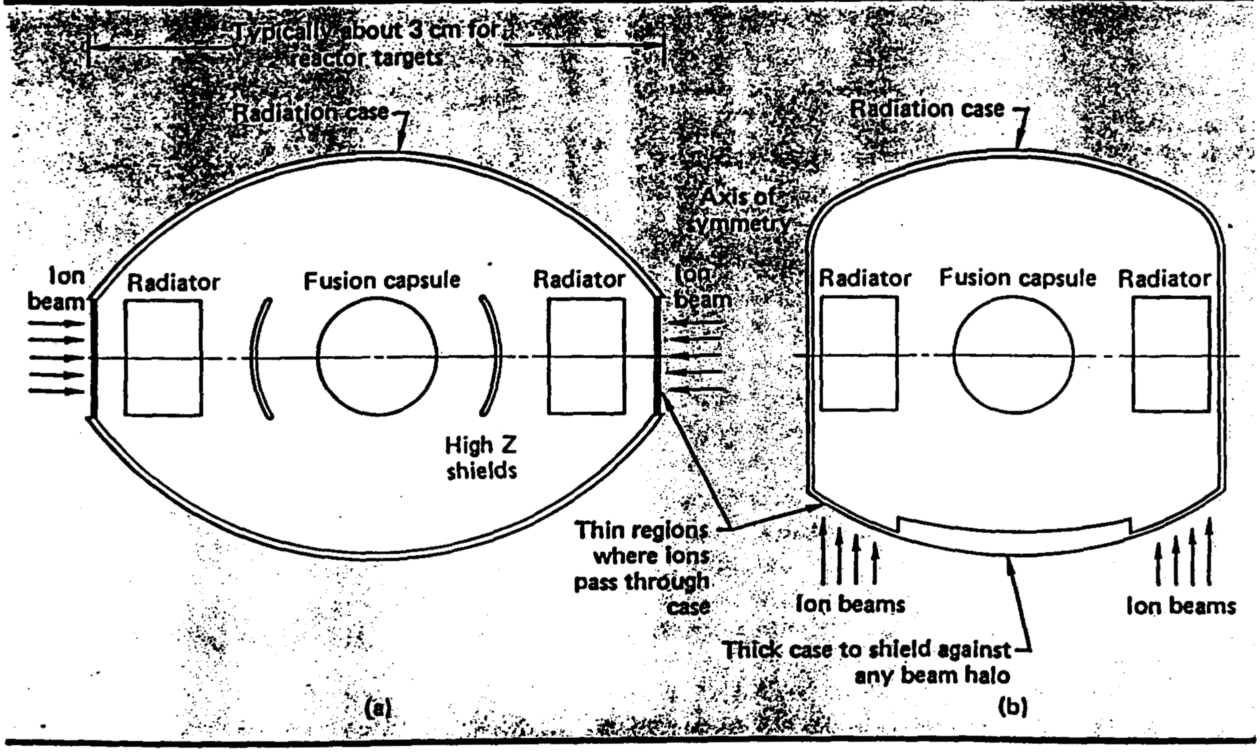

Fig. 2-34. Two induction linac configurations.

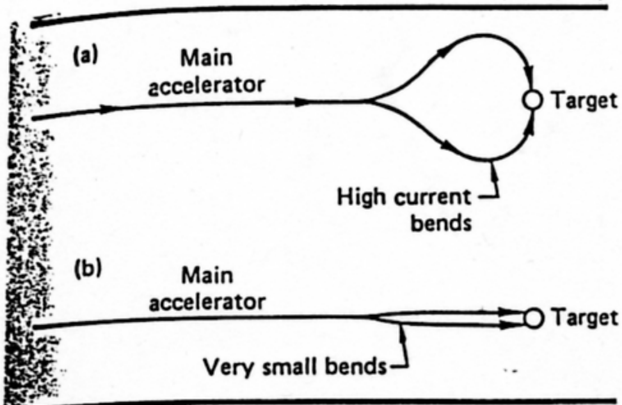

where E_b is the total beam energy and E_c is the energy required to heat the radiating material. This is expressed in terms of specific energy ϵ_b by dividing by the radiating mass.

If one considers beams incident on the ends of n cylindrical radiators of radius r, the specific energy is given by

$$\epsilon_b = E_b/n\pi r^2 R \quad , \tag{4}$$

where R is the ion range in terms of areal density, e.g., grams per square centimeter. If the radiator is to be effective, r cannot be so small that the radiator disassembles in a time short compared to the capsule implosion time. Furthermore, the radiating materials must have proper radiation transport properties, and it is important that not too much energy be lost as kinetic energy.

Fig. 2-35. Simple radiation generator that employs a high-Z tamper to prevent radial expansion.

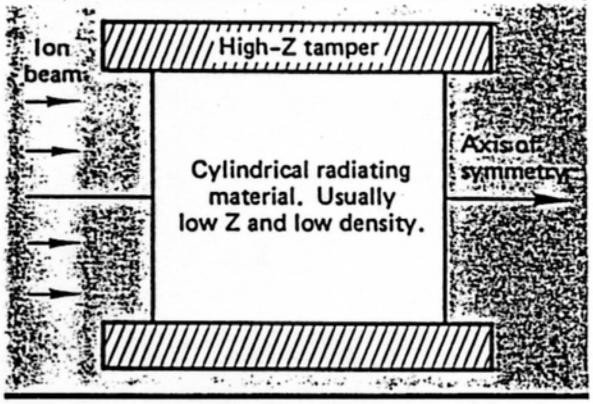

Fig. 2-36. Efficiency of conversion of ion energy to x-ray energy as a function of areal density of the radiating material. Typical curve calculated by LASNEX. A beryllium radiator 5 mm in diameter and with a density of 0.185 g/cm^3 was assumed.

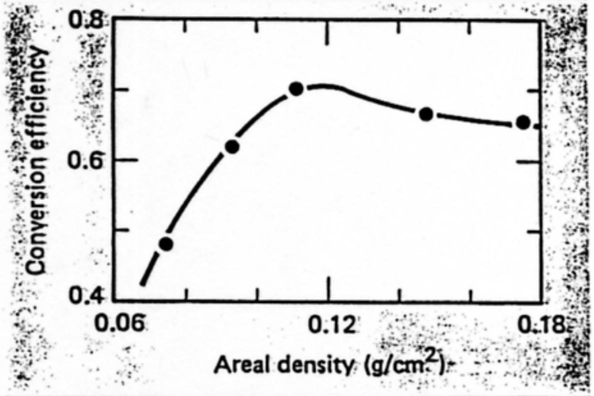

One way to hold the radiator together for a sufficient length of time is shown in Fig. 2-35. The high-Z tamper surrounding the radiating materials prevents radial expansion. Axial expansion is less serious because the areal density is independent of length. Of course, some radial expansion will occur if the radiating material expands beyond the tamper. For this reason, we vary the areal density of radiating material to optimize the conversion efficiency as calculated by LASNEX. Results of typical LASNEX calculations are shown in Fig. 2-36. The incident power was a very modest 42 TW for 50 ns, giving a total energy of 2.1 MJ. Equation 3 gives a maximum conversion efficiency of about 0.85, compared to 0.7 for the LASNEX calculation.

These calculations show that the conversion efficiency can be very good. Even higher efficiencies are possible if shorter ranges, smaller focal-spot sizes, or higher powers are assumed. The efficiency is expected to be somewhat lower when the radiators are placed in a hohlraum, because a higher radiator temperature is required to achieve adequate radiation transport into a hot hohlraum than into free space.

Two-dimensional calculations performed on the design concept shown in Fig. 2-33(a) show that it is possible to conservatively design heavy-ion targets with gains lying within the band shown in Fig. 2-19. We have not yet optimized the target designs, and improvements seem possible. The calculations should be quite reliable because of the simplicity of the beam-target interaction in ion-beam fusion.

Author: R. O. Bangerter

Theoretical Modeling

A classified Inertial Confinement Fusion (ICF) target is a complicated, multicomponent structure. A laser pulse enters an enclosure (can) from each end, scatters around, and absorbs on the interior walls of the can. Sometimes scattering cones are inserted in the can to meet the laser and scatter it. The soft x radiation produced in this hohlraum impinges on a target ball in the center of the enclosure, ablating the outer layer of the ball and imploding the rest of it. Suprathermal electrons produced by laser plasma interactions also impinge on the ball, causing preheat. In this article, we present analytic calculations for all these processes.

The resulting, simple, scaling models should be of use to all target designers; not only to help them find the right places in parameter space for their designs but also to enhance their understanding of the physics involved in the design. We compare these models with test problems run on LASNEX. (Comparison with experiment will be made in "Investigations of ICF Target Physics: Preheat, Shock, and T_R Scaling Experiments with Half-Cairn Hohlraums.") We first derive scaling laws for the radiation temperature (T_R) produced in the hohlraum. These are followed by laws for the pressure (*P*) imposed on a target ball as a result of this radiation. Next we will discuss such suprathermal-electron issues as their transport in a complex geometry (i.e., around scattering cones). Finally, we will apply all of these "ingredients" to a simple implosion model.

Scaling Law for Radiation Temperature

The physical picture we consider is that of a laser absorbing on the interior walls of a can (typically gold). These walls act like gold disks and convert some of the absorbed light into a soft x-ray spectrum. The conversion efficiency (C.E.) scales roughly as

$$\text{C.E.} \sim 0.33(I_{14})^{-0.15} \quad , \tag{5}$$

from gold disk experiments and LASNEX simulations, where I_{14} is the laser intensity in units of 10^{14}

W/cm^2. (However, quite a bit of uncertainty still exists for both the coefficient and exponent.) Thus, we have a source of radiation energy (E_R) as follows:

$$E_R = (C.E.)E_{ABS} = (C.E.)f_{ABS}E_{Inc} \quad . \tag{6}$$

where f_{Abs} is the absorption fraction. For most well-designed can and laser parameters, f_{Abs} is near or above 80%. Because C.E. is typically one-third (although it has been measured to rise as high as two-thirds), much energy remains unaccounted for. The rest of the absorbed laser energy goes into suprathermals (typically 1 to 30%) and into the kinetic energy of blowoff of ions (hydrodynamic motion). This motion does not significantly affect the heating that goes on deeper in the walls and can be neglected. The suprathermals, however, deposit deep within the walls (typically 2 μm into gold) and do contribute to heating the walls. Thus, neglecting their contribution is a serious defect of the model under conditions when E_R is the same order as E_{hot} (laser-converted energy into hot electrons).

We equate the radiation source, Eq. (6), with the energy sinks in the problem: The radiation eats through the inner part of the walls in a thermal diffusion (Marshak) wave, heating the wall up to an equilibrium temperature, $T_r = T_e$, where T_e is the electron temperature that we are trying to calculate. Some of the radiation escapes out of laser entrance holes and out of holes cut in the hohlraum for diagnostic purposes, and some of it diffuses into the target ball.

We first consider the wall-loss problem by solving (in 1-D) for the radiation diffusion into a material. The first law of thermodynamics states

$$\frac{d\epsilon}{dt} + \frac{Pd(1/\rho)}{dt} = Q \quad , \tag{7}$$

where ϵ is the specific internal energy, P is the pressure, ρ the matter density, t the time, and Q is an energy source. For radiation diffusion,

$$Q = \frac{1}{\rho}\frac{\partial}{\partial x} c\lambda_R \frac{\partial}{\partial x}(aT_r^4) \quad , \tag{8}$$

where $\lambda_R \equiv 1/K\rho$ is the Rosseland-averaged radiation mean free path, K is the Rosseland-averaged opacity, c is the speed of light, x the distance into the wall, and a is $4\sigma/c$, where σ is the Stefan–Boltzman constant. For slow subsonic heat penetration into a material that is simultaneously blowing off into vacuum, we can approximate pressure P as a constant at the heat front. In a Lagrangian sense then, with the mass variable

$$m \equiv \int_0^x \rho(x')dx' \quad , \tag{9}$$

Eqs. (7), (8), and (9) become

$$\frac{\partial h}{\partial t} \equiv \frac{\partial(\epsilon + P/\rho)}{\partial t} \equiv \frac{\partial}{\partial m}\left[\frac{c}{3K_R}\frac{\partial}{\partial m}(aT^4)\right] \quad , \tag{10}$$

where h is specific enthalpy (thus accounting for hydrodynamic blowoff energy of the radiatively heated matter as well as for the internal heating energy).

To solve Eq. (10) with a similarity solution, we set

$$h \equiv h_0T^{\ell}; K \equiv K_0\rho^R T^{-n}; \beta \equiv 4 + n + \frac{R\ell}{2} - \ell; w \equiv mt^{-Q} \quad ;$$

$$T \equiv T_0t^p f(w); \frac{\partial}{\partial\omega} \equiv (\ )'; \rho \approx m/c_st = m/c_{0,s}\,T^{\ell/2}t \quad ;$$

$$D \equiv \frac{c}{3K_0}\frac{a}{h_0}\frac{T_0^{\beta}4C_{0,s}^R}{\beta + \ell} \quad . \tag{11}$$

Because opacity may depend on density, we set the density to an average "ice-block" by dividing the mass by a product of sound speed C_s, and time (i.e., the change in volume of that blowoff mass . Thus, Eq. (10) becomes

$$\frac{D}{w^R}f^{(\beta+\ell)''} - \frac{RD}{w^{(R+1)}}f^{(\beta+\ell)'} + QW(f^{\ell})' - p\ell f^{\ell} = 0 \quad , \tag{12}$$

with

$$Q = (\beta p + 1 + R)/(2 + R) \quad . \tag{13}$$

Because we are anticipating a steep heat front of the form $f(w) = [1 - (w/w_0)]^{\epsilon}$, $\epsilon << 1$, we can solve Eq. (12) near the front by dropping the small second and fourth terms of Eq. (12). Then Eq. (12) is solved by

$$f(w) = \left[1 - (w/w_0)\right]^{1/\beta} \ ,$$

$$w_0^{(\alpha+R)} = \frac{D}{Q}\left(\frac{\beta+\ell}{\beta}\right) \ . \qquad (14)$$

For a constant driving temperature ($p = 0$) and for opacity independent of density ($R = 0$), we have the usual diffusive behavior: $Q = 1/2$ and the front progresses as $m_0 \approx w_0 t^{1/2}$. For typical materials, $n \approx 2$ and $\ell \approx 1$, giving $\beta = 5$ and

$$T = T_0 \left[1 - (m/m_0)\right]^{1/5} \ ,$$

as the shape of the steep self-similar heat front.

The last step of the calculation is to find the "wall-loss" now that we know the time and space behavior of the temperature. There are two approaches in this regard. First, we can integrate the enthalpy over space:

$$\begin{aligned} H_\ell &= \int_0^{m_0} h \, dm \\ &= h_0 (T_0 t^p)^{\ell} \int f^{\ell} \, dm \\ &= h_0 (T_0 \tau^p)^{\ell} \, m_0 \beta/(\beta + \ell) \ . \end{aligned} \qquad (15)$$

Second, we can integrate the flux at the boundary over time:

$$\begin{aligned} H_\ell &= \int_0^t F \, (dt) \\ &= \int_0^t \frac{ac \, T^n}{3K_0 \rho R} \ \frac{\partial a T^4}{\partial m} \, (dt) \\ &= \int_0^t \frac{ac}{3K_0 \rho^R} \ T_0^{n+4} \tau^{p(n+4)} f^n \, \frac{\partial f^4}{\partial m} \, (dt) \\ &= h_0 (T_0 t^p)^{\ell} \, m_0 \, Q/(Q + R + p\ell) \ . \end{aligned} \qquad (16)$$

Comparison of Eqs. (15) and (16) shows the two estimates are within 30% of each other under most conditions. We will use Eq. (15) for the wall loss per unit area.

As a concrete example, we consider gold. All quantities are now known, yielding

$$m_0(\mathrm{Au}) = 1.9 \times 10^{-3} \, T_r^{1.55} \, \tau^{0.57} \ (\mathrm{g/cm^2}) \ . \qquad (17)$$

where T_r is in hundreds of eV (hectovolts), and the radiation pulse length τ is in ns. The gold wall loss can be written as

$$A_w H_\ell = 0.44 \, T_r^{3.05} \, \tau^{0.57} \, A_w \ (\mathrm{hJ}) \ , \qquad (18)$$

where A_w is the can's wall area (in mm^2), τ is in nanoseconds, the radiation temperature T_r is in hectoelectron volts and the wall loss in hectojoules. These are natural hohlraum units because temperatures usually vary between 1 and 2 heV, can sizes for Shiva are between 5 and 10 mm^2, pulse lengths are of the order of 1 ns, and absorbed laser energies are between 6 and 60 hJ. In addition, the Stefan–Boltzman constant, σ, for these units equals one, which is convenient. Thus, losses out of laser entrance holes can be immediately written as

$$\text{Hole loss} = T^4 \tau A_{Leh} \text{ (hJ)} \quad . \qquad (19)$$

where A_{Leh} is the area (in mm^2) of the laser entrance holes.

To calculate target-ball losses, we must know the material involved. As an example, we take glass, where $K \approx 8\rho^{1/3} T^{-2.5}$ and $Z \approx 20 T^{1/2}$, and T is in keV. Proceeding as before we obtain

$$m_{0(g)} \approx 9 \times 10^{-4} T^{2.25} \tau^{0.57} \text{ (g/cm}^2) \quad ,$$

$$\text{Glass-ball loss} \approx 0.8 T^{3.75} \tau^{0.57} A_{Ball} \text{ (hJ)} \quad , \qquad (20)$$

with quantities expressed in hohlraum units (h.u.) as in Eqs. (17) and (18). Here A_{Ball} is the ball area in mm^2.

For present targets, A_B and A_{Leh} are both much smaller than A_w, so that to first order they may be neglected. Thus, equating sources to sinks, we find

$$\text{(C.E.)} \times E_{Abs} = \text{gold wall loss.}$$

Using Eq. (5) for C.E. and recalling that I in 10^{14} W/cm^2 equals 10 $E/A_w\tau$ in h.u., we find Eq. (18) leads to

$$T \approx (E_{Abs}/A_w \tau^{0.5})^{0.28} \quad . \qquad (21)$$

Equation (21) compares favorably with experiment (see Fig. 2-47 and "Investigations of ICF Target Physics: Preheat, Shock, and T_R Scaling Experiments with Half-Cairn Hohlraums" of this report). In general, we can derive the temperature iteratively, using Eq. (21) as a first approximation and then refining and lowering it, because the ball and hole-loss equations, (19) and (20), do contribute as extra sinks to balance the E_r source. While agreement with experiment is good, there are still uncertainties in the theory. It is crude in the sense of assuming a constant average temperature T_0 as the driving source (for a duration τ_L) rather than treating the actual temporal behavior. In addition, the conversion-efficiency scaling is still uncertain and is measured on a disk rather than inside a hohlraum. Also, as mentioned previously, in some of the shots as much energy was in hot electrons as in radiation, but this theory does not treat the hot-electron contribution to wall heating. Despite the caveats, Eq. (21) does seem to have general validity for the experiments done so far.

Fig. 2-47. Experimental radiation temperature (eV) vs the Marshak-wave figure of merit $((E_a(\text{hJ})/A_w(\text{mm}^2)\tau(\text{ns}))^{0.5}$. Solid line is theoretical prediction derived from Eq. (17).

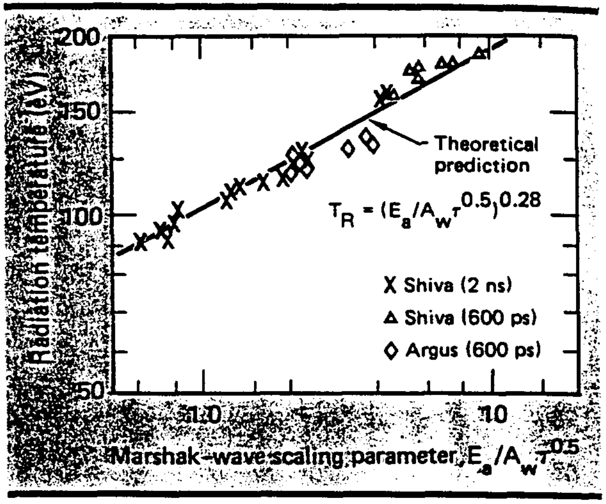

We will explore one more aspect of radiation-temperature-scaling law. Some hohlraums show true primary and secondary behavior:

- First, the laser scatters back off a cone and into a general primary region of the can where the radiation is produced.
- Second, the radiation diffuses through the annular region between the cone and cylinder walls to the general secondary region, where the target ball sits behind the cone.

This behavior can be modeled by equating sources and sinks in each region. In the primary,

$$E_R + T_s^4 A_{ps}\tau = 0.44\, T_p^{3.05} A_{wp}^{0.57} + T_p^4 A_{Leh}\tau + T_p^4 A_{ps}\tau$$

and in the secondary,

$$T_p^4 A_{ps}\tau = 0.44\, T_s^{3.05} A_{ws}\tau^{0.57} + T_s^4 A_{Diag}\tau$$
$$+ T_s^4 A_{ps}\tau + 0.8\, T_s^{3.75} \tau^{0.57} + A_{Ball}^{0.57} \quad .$$

Here T_p and T_s are the respective primary and secondary temperatures; $A_{w,ps}$ refers to the respective wall areas; A_{ps} is the area of the gap between the primary and secondary, A_{diag} is the area of diagnostic holes in the secondary. Because in practice, $A_{ws} << A_{wp}$ and $T_s^3 << T_p^3$, we can put these equations into a form amenable to solution by iteration. Adding the primary and secondary equations, we obtain

$$E_R = 0.44\,\tau^{0.57} A_{wp}\, T_p^{3.05} \left(1 + \frac{A_{ws}}{A_{wp}} \frac{T_s^{3.05}}{T_p^{3.05}} \right)$$

$$+ \tau(A_{Leh}\, T_p^4 + A_{1Diag}\, T_s^4) + 0.8\tau^{0.57}\, A_{Ball}\, T_s^{3.75} \quad , \qquad (22)$$

where the first term on the right-hand side is the dominant one. The secondary equation, rewritten is

$$\tau A_{ps}\, T_p^4 \left(1 - \frac{T_s^4}{T_p^4} \right) = 0.44\, A_{ws}\, \tau^{0.57}\, T_s^{3.05}$$

$$+ A_{Diag}\, T_s^4 + 0.8\, A_{Ball}\, \tau^{0.57}\, T_s^{3.75} \quad . \qquad (23)$$

Usually the first term on the right-hand side is the dominant one. Thus, Eqs. (22) and (23) can be used to predict primary-to-secondary differences.

In the early Argus experiments, both primary and secondary temperatures were measured. In general, T_p was about 1.5 heV and T_s about 1.1 heV. Equations (22) and (23) reproduce T_p as 1.5 but find $T_s \approx 1.25$, implying some anomalous losses of energy (two-fold) from the wall or problems with radiative transport. A third interesting possibility is that the channel closes as the heated cone expands outward and the heated wall implodes inward. Using sound speed, opacity, and density scaling laws for gold that were derived earlier, we indeed find A_{ps} may shrink to half its size. This halves the flux into the secondary and thus explains the anomalously low T_s. Further experiments (planned for Shiva) could shed light on some of these important issues.

Radiation-Driven Ablation Pressure Scaling Law

What pressure does a given radiation temperature impinging on a target ball apply to that ball? What velocity does the unablated portion of the pusher achieve?

Following the hydrodynamic theory of subsonic heat-wave penetration, we find that for a γ-law gas,

$$P_A = (\gamma - 1)W/\sqrt{\gamma C_s} \quad , \qquad (24)$$

where P_A is the ablation pressure produced by a heat front with flux W. Equation (24) is basically a heat flux balance, with the energy being carried off at the sound speed, C_s. The radiative heat flux is given in the parenthesis of Eq. (8) and can be rewritten as

$$W = (4/3)\, \sigma T^4/mK \qquad (25)$$

where m is defined in Eq. (9) and derived in Eqs. (11) and (14). Equation (25) simply states the heat flux is the radiative vacuum flux divided by the number of radiation mean free paths. In the discussion preceding Eq. (20), we presented the relevant formulae for glass. These combined with Eqs. (24) and (25) result in

$$P_A(\text{glass}) \approx 8\, T^3/\tau^{0.43}\ (\text{MB}) \quad , \qquad (26)$$

where T is in heV, τ in ns, and P in megabars. Because opacities differ with material, this expression for the pressure will vary greatly with material. For gold (high opacity), we find

$$P_A(\text{Au}) \approx 3.5\, T^{2.3}/\tau^{0.43}\ (\text{MB}) \quad , \qquad (27)$$

and for beryllium (low opacity) we find

$$P_A(\text{Be}) \approx 14\, T^{3.5}/\tau^{0.40}\ (\text{MB}) \quad . \qquad (28)$$

Thus, one of the interesting aspects of radiatively driven targets is the ability to tune the pressure profile simply by changing ablator material. One should be cautious, however, in that the lowest opacity materials (which provide the highest pressure) have such fast heat-front penetration that the reaction can become supersonic and thus inefficient. For example, consider LiD. We find that

$$m(\mathrm{LiD}) \approx 6 \times 10^{-3}\, T^{2.6}\, \tau^{0.64}\ (\mathrm{g/cm^2}) \quad . \tag{29}$$

Thus, for 0.8 density LiD, at 100 eV and 1 ns, the front moves 75 μm, giving a "speed" of 7.5×10^6 cm/s. But the sound speed C_s, at 100 eV, is 6×10^6 cm/s, so the heat front is supersonic. At higher temperatures or shorter times, it is even more so. (The pressure it could provide scales as $20\ T^{3.2}/\tau^{0.3}$ MB.)

Also of interest is the comparison of the energy requirements of a radiation-driven vs direct-illumination approach to getting the same pressure on a ball. Suppose the ablator is beryllium, then Eq. (29) combined with Eq. (21) yields

$$P_A(\mathrm{Be}) = 17(I_{13})^{0.9} = 135(I_{14})^{0.9}\ (\mathrm{MB}) \quad , \tag{30}$$

where $I_{13,14}$ is the laser intensity expressed in units of $10^{13,14}$ W/cm^2 and the intensity is the energy per unit time per unit of can area. A great deal of literature that exists on ablation pressure is taken from direct laser illumination studies. Roughly it scales as

$$P_\ell \approx 7.0(I_{14})^{0.7}\ (\mathrm{MB}) \quad , \tag{31}$$

independent of target material. Here I is the absorbed energy per unit time per unit ball area. Let us compare Eqs. (30) and (31) for SHIVA parameters (ball radius 100 μm, can size 6 mm^2, 1-ns pulse) assuming 30% absorption for direct illumination, and requiring 50 MB ablation pressure. The unclassified approach requires 6 kJ, compared to only 2 kJ for the classified approach. As we go to larger systems in which the area ratio of ball to can is larger, the classified approach looks even more promising.

Fig. 2-48. LASNEX scaling of pressure (P) and Marshak penetration depth (M) at two source temperatures (100 and 200 eV) as a function of time.

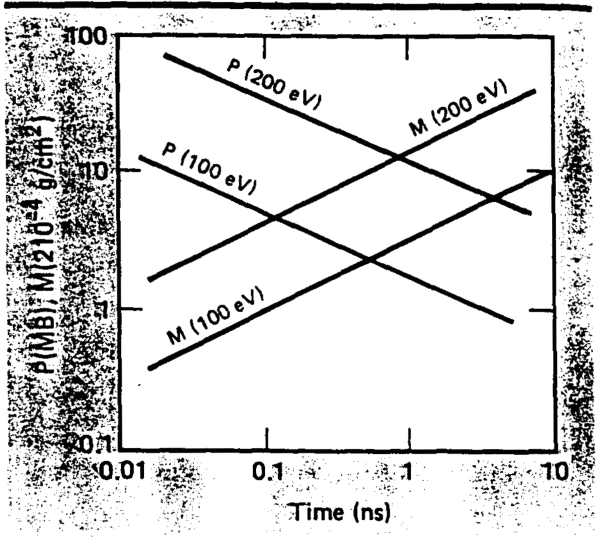

Table 2-10. Comparison of exponents obtained by theory and by LASNEX code for the front motion, m, and for the pressure, P_A, both for gold and glass.

Quantity	Exponents	
	LASNEX	Theory
$m(\mathrm{Au}) \sim T^{(\ )}$	1.7	1.6
$\tau^{+(\ )}$	0.54	0.57
$K_0^{-(\ )}$	0.45	0.43
$P_A(\mathrm{Au}) \sim T^{(\ )}$	2.4	2.3
$\tau^{-(\ )}$	0.41	0.43
$K_0^{-(\ )}$	0.48	0.43
$m(\mathrm{glass}) \sim T^{(\ )}$	2.3	2.3
$\tau^{(\ )}$	0.63	0.57
$P_A(\mathrm{glass}) \sim T^{(\ )}$	3.1	3.0
$\tau^{-(\ )}$	0.33	0.40

The scaling laws for the front motion m and for the pressure P_A were tested against multigroup LASNEX problems. We place a constant temperature souce next to a material and monitor the pressure and penetration of the front as a function of time. We vary (from problem to problem) the driving temperature, the opacity multiplier, and the material. Some curves for gold are shown in Fig. 2-48. We compare the exponents (i.e., the scaling) between theory and code for gold and glass in Table 2-10. Code-generated coefficients for the pressure are within 20% of the theoretical prediction.

Because the depth penetration is difficult to define in the code, it cannot be quantitatively compared with the theory.

Radiation-driven pressures were measured experimentally, in good agreement with the theory presented here. (This agreement will be demonstrated in "Investigations of ICF Target Physics: Preheat, Shock, and T_R Scaling Experiments with Half-Cairn Hohlraums" of this report.)

Finally, we answer the question about implosion velocities achieved. The shock of strength P_A propagates through the pusher at density ρ_0, at a speed V_s, given by

$$V_s = [(\gamma + 1)P_A/2\rho_0]^{1/2} \quad , \tag{32}$$

and jumps off into the low density D-T gas at about twice V_s, giving a pusher-interface velocity of

$$V_{p,int} \approx \frac{2}{\gamma + 1}(2V_s) \quad . \tag{33}$$

The rest of the unablated pusher has received an impulse from the pressure pulse P_A. Thus, setting the acceleration (a) equal to a force per mass (F/m), we find

$$[illegible] = a\tau = \frac{F\tau}{m} = \frac{P_A A\tau}{\rho_0 A\ell} = \frac{P_A\tau}{\rho_0\ell} \quad , \tag{34}$$

where ℓ is the unablated portion of the pusher,

$$\ell = \rho_0(\Delta R)_0 - m(T_r, \tau) \quad , \tag{35}$$

where ΔR_0 is the original pusher thickness. For mass, we can take m_g from Eq. (20) and P_A from Eq. (26) to find the unablated pusher velocity. This will be compared with experimental measurements in "Investigations of ICF Target Physics: Preheat, Shock, and T_R Scaling Experiments with Half-Cairn Hohlraums" and is again in good agreement. The treatment in this section was planer. Spherical effects allow the radiatively heated blowoff to lower its ρR (and thus its radiative mean free paths), thereby raising the ablation pressures perhaps by 30% under typical conditions). Also, the planer treatment does not account for speeding up the pusher as it implodes spherically. The experiments with which Eq. (34) will be compared are essentially planer.

Suprathermal Electron Transport and Preheat

In a complex geometry such as a Cairn can with a primary and secondary, a question exists as to how many of the suprathermals, which are produced in the primary, can transport around the cone, impinge on the target ball, and cause preheat. To model this problem, we assume the electrons are isotropic and collisionless within the volume of the can, simply bouncing randomly off the walls. For normalization purposes, let us assume 100 electrons (of average energy E_0) are in the primary. According to the area ratios $A_{ps}/A_{p,tot}$, $A_{w,p}/A_{p,tot}$, and $A_{Leh}/A_{p,tot}$, we transport them into the secondary, into the primary (and scattering cone) wall, and through the laser entrance holes, respectively. Here, A_{ps} is the area of the annular gap around the cone through which the electrons can pass into the secondary. Of the large fraction of electrons that hits the gold walls, half remain in the wall and half are reflected back into the primary with 0.7 E_0 of their energy. These numbers are based on published cold, gold albedoes. The electrons transported out the entrance hole are lost forever.

In the second iteration, those electrons in the secondary are now transported into the ball, into the secondary wall and back of the cone, or back to the primary, according to the area ratios $A_b/A_{s,tot}$, $A_{w,s}/A_{s,tot}$, and $A_{ps}/A_{s,tot}$, respectively. In this same second iteration, the electrons that were reflected off the primary walls in the first iteration are now transported by the same method as used for the original 100 electrons in the first iteration. This process is shown in Fig. 2-49 for a 1.4-size, half Cairn (with a sample glass disk rather than a target ball). For this case, the parameters are:

$A_{ps}/A_{p,tot} = 0.20$, $A_{w,p}/A_{p,tot} = 0.78$,

$A_{Leh}/A_{p,tot} = 0.02$; $A_{ps}/A_{s,tot} = 0.29$,

$A_{w,s}/A_{s,tot} = 0.65$, $A_b/A_{s,tot} = 0.06$.

Fig. 2-49. Example of a suprathermal-electron-transport estimate. The initial 100 electrons of energy (E_0) in the primary are transported either into the secondary or into the walls, depending on area ratios and wall reflectivities.

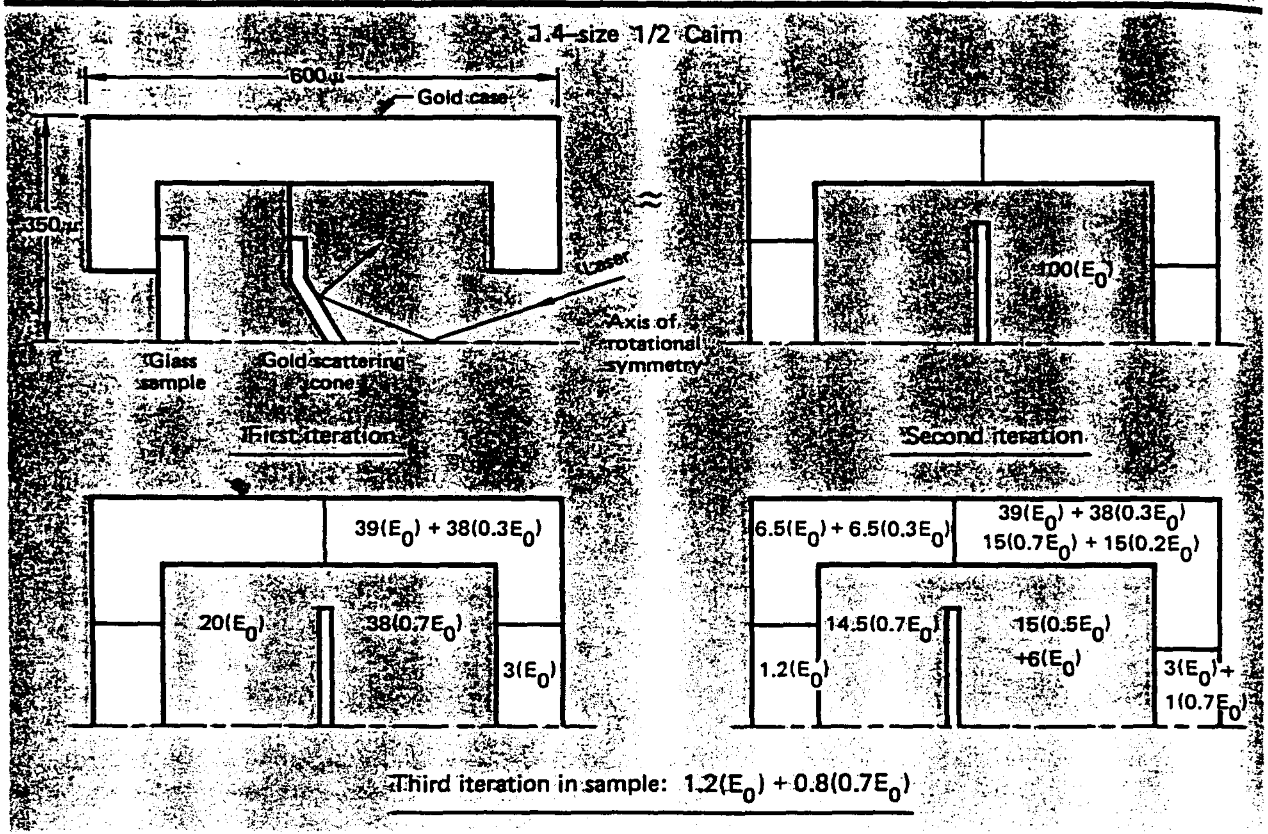

Finally (after just a few iterations), we see that the cone has shielded the ball. Had there been no cone, the same calculation, including the gold albedo of the wall, would result in three times more energy impinging on the ball, with $A_b/A_{tot} = 0.035$. Thus of the 100 electrons at E_0, 3.5 would get to the sample with energy E_0, 1.7 would have energy 0.7 E_0, and so on. This is about three times the energy getting to the sample $[1.2(E_0) + 0.8(0.7\ E_0)]$ in the cone-case.

This shielding factor will depend on geometry and size of the can, since it depends on the many area ratios mentioned above. From the measured suprathermal x-ray emission, we can deduce E_{hot}, the amount of energy in hot electrons and their mean temperature, T_{hot}. By transporting them as above, we can determine the preheat temperature caused in a sample. The calculation is done in detail in Section 5.8, and compares favorably with experiment. The scaling E_{hot} and T_{hot} with laser and can parameters is a subject now under intense investigation.

Scaling Laws Applied to a Simple Implosion Model

We can now apply the many "ingredients" thus far derived to a simple implosion model. Given laser parameters (E_L, τ_L), can parameters (size, area, cone or no cone, and the like), and ball parameters (radius R_0, pusher thickness ΔR_0, pusher material, D-T fill $\rho_{0,D\text{-}T}$), we can derive from first principles the target performance. From Eq. (21), we know T_R. Assuming a glass pusher, we know P_A from Eq. (26). This pressure wave transports through the glass and shocks the D-T, thus setting the adiabat. From Eq. (32) and the doubling of the shock as it breaks out of the glass pusher, we find

$$P_{(D\text{-}T)} = 4\rho_{0(D\text{-}T)}\,P_A/\rho_{0,p}\ . \qquad (36)$$

Typically, $\rho_{0(D\text{-}T)} = 0.01$ and thus $P_{(D\text{-}T)} \approx P_A/50$. We now compress the D-T isentropically to a final pressure, $P_{f(D\text{-}T)}$,

$$_{f(D\text{-}T)} = P_{(D\text{-}T)} \left[\rho_{f(D\text{-}T)}/4\rho_{0(D\text{-}T)}\right]^{5/3} \quad , \tag{37}$$

where we use the strong-shock relation to find the post-shock D-T density,

$$+ 1)/(\gamma - 1)\rho_{0(D\text{-}T)} = 4\rho_{0(D\text{-}T)} \quad .$$

for $\gamma = 5/3$.

The implosion will stop when the compressed D-T gas sends an impulse into the imploding pusher. Thus, equating the impulse force times Δt, Δt, with the change of pusher momentum, $\Delta(MV)$, we get

$$F(\Delta t) = \Delta(MV) \text{ or}$$

$$_{(D\text{-}T)} A(\Delta t) = \rho_p A(\Delta r) V_p \quad . \tag{38}$$

where V_p, ρ_p are the pusher implosion velocity and density, respectively. Because the impulse travels at the sound speed,

$$/\Delta t \sim C_s \sim (P_p/\rho_p)^{1/2} \quad , \tag{39}$$

Equations (38) and (39) thus yield

$$_{(D\text{-}T)} \sim \sqrt{\rho_p P_p}\,(V_p) \quad . \tag{40}$$

If we assume pressure continuity across the interface (since this is "turn-around" time), as well as temperature continuity because to conduction, the differing Z/A (ratio of charge to atomic number) for D-T and glass gives

$$_{(D\text{-}T)} \sim P_p,\ T_{(D\text{-}T)} \sim T_p,\ \rho_{f(D\text{-}T)} \sim 0.5\,\rho_p \quad , \tag{41}$$

which turns Eq. (40) into

$$_{(D\text{-}T)} \sim 2\,\rho_{f(D\text{-}T)} V_p^2 \quad . \tag{42}$$

Combining Eqs. (36), (37), and (42) gives an expression for the final density,

$$\rho_{f(D\text{-}T)}^{2/3} = \rho_{0,p} \left(4\rho_{0(D\text{-}T)}\right)^{2/3} \left(2V_p^2/P_A\right) \quad . \tag{43}$$

The "implosion" velocity V_p can be approximated by Eqs. (34) and (35). For a badly preheated implosion (the adiabat is raised), we naively replace the denominator of Eq. (43) with $P_A + P_{pre}$, where P_{pre} is the preheat pressure generated by the hot electrons on the inside of the pusher.

Currently, the experimental observables are implosion time, yield, and pusher ρR. The implosion time τ_{imp} can be modeled as

$$\tau_{imp} = \frac{\Delta R_0}{V_s} + \frac{R_0}{V_p} \tag{44}$$

where the shock velocity V_s is given by Eq. (32). The yield, Y, in neutrons (assuming hydrodynamic quenching of the reactions) is approximately

$$Y = 2 \times 10^{10}\, \rho_0^2\, R_0^4\, (\rho_f/\rho_0)^{2/3}_{(D\text{-}T)}\, (\sigma V/T^{1/2}) \tag{45}$$

where ρ_0 is in units of 5×10^{-3} g/cm^3, R_0 in 100 μ, and $(\sigma V/T^{1/2})$ in 10 keV. The pusher ρR can be related to the final D-T density through the "isothermal-isobaric" model [essentially the assumptions of Eq. (41) reported in Ref. 1], which yields

$$\rho R = \rho_{f(D\text{-}T)}^{2/3} \left(2\rho_{0(D\text{-}T)}^{1/3} R_0 \left\{\left[1 + M_p/2M_{(D\text{-}T)}\right]\right\}^{1/3} - 1\right) \quad , \tag{46}$$

where M_p and $M_{(D\text{-}T)}$ represent the unablated pusher mass and the D-T mass, respectively.

As an example, we compare the model with a Shiva experiment. The values used were as follows: Laser parameters, 8 kJ incident in 600 ps; can parameters, 2.0 scale-size Cairn (with cones), i.e., cylinder 1.6 mm long and 1 mm in diameter. For the glass target ball, R_0 was 70 μm, ΔR_0 was 16 μm, ρ_{op} was 2.2 g/cm^3, and $\rho_{0(D\text{-}T)}$ was 0.01 g/cm^3.

Equation (21) yields a T_R of 180 eV, as observed. Equation (26) implies P_A is 50 MB. Equation (20) gives a 10-μm penetration of the front, leaving ℓ equal to 6 μm. Equation (34) gives V_p as 2×10^7 cm/s. Equation (44) gives a 500-ps implosion time, as observed. Equation (43) gives ρ_f equal to 8 (or 40-times liquid density). Equation (46) gives ρR equal to 0.023, as observed. Equation (42) gives a T_I of 900 eV, so Eq. (45) gives a yield of 7×10^7, which is about 20 times the observed value. However, mix corrections were not applied.

As a second example, we consider the difference between a model H (no cones) and model B (cones) hohlraum design. As shown earlier, the target ball in the model B should be perhaps three times better protected from preheat than the model H. Thus, given the E_{hot} (30 to 50% of E_{Abs}) measured, we find a model H to be preheated to 40 eV, corresponds to P_{pre} equal to 35 MB. Thus, the adiabat is almost effectively doubled in the model H, which lowers $\rho^{2/3}_{f(D\text{-}T)}$ by one-half [Eq. (43)]. This lowers the observed ρR by one-half [Eq. (46)], thus yielding a $\rho R \approx 0.011$, as observed. The neutron yield should be the same, but because of its semi-exploding-pusher behavior, mix may not play a crucial role. Thus the yield prediction of 7×10^7 should remain uncorrected. If so, it indeed is within a factor of two of the experimental yield measurement for the model H; so essentially, the yield prediction is as observed.

Certain caveats should be considered at this point. The implosion process is quite complex. The D-T heating by shock and compression is enhanced by spherical convergence. As mentioned, mix can play a large role in the yield calculation. Ion thermal conduction, in addition to hydrodynamic expansion, plays a significant role in quenching the D-T reactions through cooling ($\sigma V \sim T_I^6$). Thus, further refinements of this simple implosion model are needed before it can be truly predictive. In the meantime, the "basic ingredients" scaling laws (for T_r and P_A) do seem to be in a useable form.

In conclusion, we have derived expressions for the radiation temperature in a laser-irradiated hohlraum [Eq. (21)], including primary-to-secondary transport corrections [Eqs. (22) and (23)]. We obtained expressions for the pressure generated by that radiation in typical target-ball-ablator materials [Eqs. (26) and (28)].

Author: M. D. Rosen

Reference

18. *Laser Program Annual Report—1979*, Lawrence Livermore National Laboratory, Livermore, Calif., UCRL-50021-79 (1980), pp.6-60 to 6-67.

Fig. 4-10. Apollo version B constructed for laser experiments during 1979.

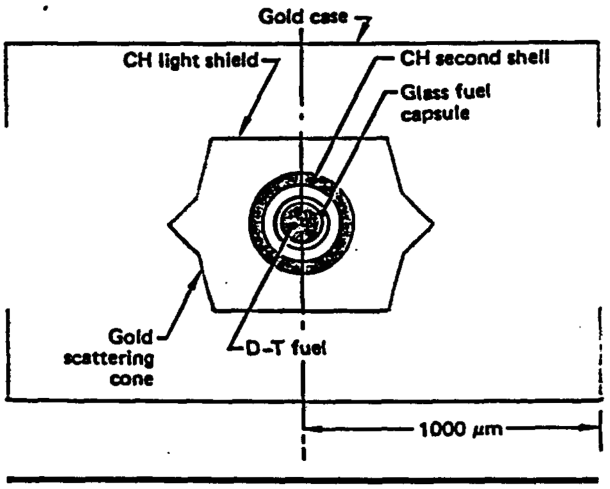

1979 Apollo Targets

The Apollo target configuration used in laser experiments this year is shown in Fig. 4-10. These targets yielded 10^6 to 10^7 neutrons and fuel density of over 20 g/cm^3 (100X liquid D-T density). The fuel capsules we used in these targets were 180-μm-diam 20-μm-thick hollow glass microspheres. These spheres must have no wall thickness variations or surface defects larger than 0.5 μm. The techniques for fabricating and characterizing these microspheres have been described in other reports.[5,6] We made the hemispheres for the second shell of the Apollo targets by micromachining a CH polymer applied over a copper mandrel. This technique is described in detail elsewhere.[7] These hemispheres are 360 μm in diameter with a 50-μm-thick wall that must be uniform to within 1 μm (2%). The two hemispheres in each target must be very closely matched to avoid an asymmetrical implosion. For these first versions of Apollo the thicknesses were matched within 1 μm and the diameters within 2 to 3 μm. The light shields, scattering cones, and radiation cases for the Apollo targets are modified versions of those used for the Cairn targets described earlier.

We assembled the Apollo targets using techniques similar to those described for the Cairn targets. We first sandwiched the fuel capsule between two ultrathin support films, which are held on a large wire loop (~7 mm diameter). The fuel capsule must be centered in the second shell with an accuracy of ±2 μm. To assure this centering we measure the sandwiched fuel capsule using reflection interferometry to determine whether the capsule is symmetrically located between the support

Fig. 4-11. Completed Apollo target. Outer shell and inner fuel capsule are visible through diagnostic hole.

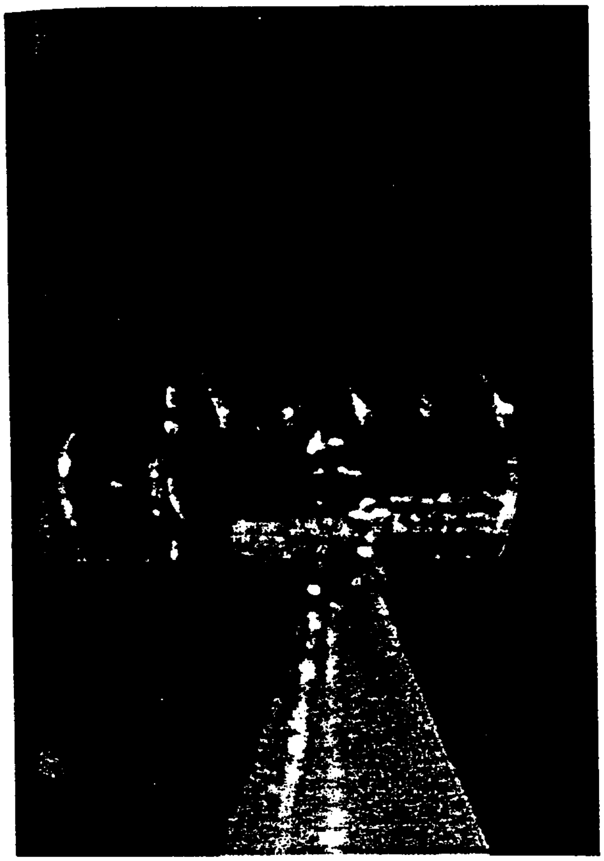

films. If the centering is not correct, the sandwich must be disassembled (which destroys the support films) and another attempt made.

If the fuel-capsule sandwich is satisfactory, we cement the hemispheres for the second shell to the support films around the sandwiched fuel capsule. At this point another reflection interferometry measurement is made to check the centering of the inner capsule. Measuring through the CH hemispheres, we determine the distance between the inner surface of the second shell and the outer surface of the fuel capsule at six points around the assembly.

If this assembly of hemispheres and fuel capsule meets the target specifications, the light shield, scattering cones and radiation case are cemented in place on the thin support films. The completed target is shown in Fig. 4-11.

A total of six Apollo targets were constructed and shot during 1979. Of these, three were the B version shown in Fig. 4-10. The other three targets were identical except that the light shield and the Au scattering cones were not installed in the radiation case. These targets are referred to as the H version.

Fig. 4-12. Improvements under development for second shell of Apollo target. Each item is expected to increase target performance.

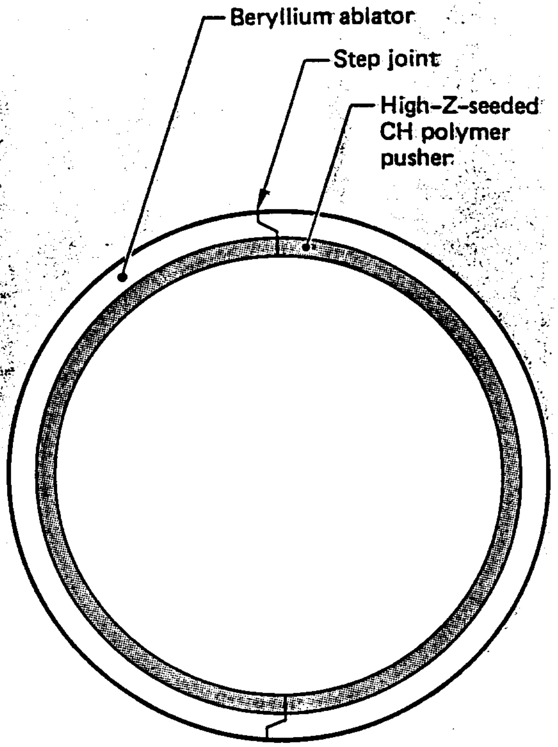

Improvements to Apollo Targets

A number of fabrication capability improvements for the Apollo targets that will increase their performance are under development. One key element in this development is replacing the CH second shell with a two-layer structure, as shown in Fig. 4-12. The inner layer would be seeded with high atomic number (high Z) material such as tungsten, tantalum, gold, or lead to provide greater preheat protection. Ideally the outer layer of ablator material would be beryllium, but the first versions will most likely use a CH ablator. Another anticipated improvement to the second shell (Fig. 4-12) is to assemble the two hemispheres with a step joint rather than simply a flat interface. This would reduce the effect of the joint on the symmetry of the

Fig. 4-13. Spherical Apollo case constructed from two gold hemishells. Hemishells are made by evaporating gold onto copper mandrel.

implosion. A third area for improving the Apollo target is to replace the glass fuel capsule with a high-Z material. This will provide more preheat protection and a more efficient tamper for the fuel. Finally, a spherical radiation case geometry is expected to improve the target performance. Spherical cases have been produced by evaporating gold onto a hemispherical mandrel in a process very similar to that used for making cylindrical cases. Figure 4-13 shows a spherical Apollo case made with two of these hemispheres.

We are actively pursuing all of these improvements. Machining of CH hemispheres with a step joint is being attempted and we expect the first hemispheres of this type in early 1980. We are also investigating the feasibility of machining beryllium coatings that have been vapor deposited on mandrels to provide a beryllium second shell. Studies are underway to identify candidate materials for a high-Z seeded polymer that can be used as the inner layer of a two-layer second shell. We are also developing high-Z coatings on thin glass microspheres as a step toward a high-Z fuel capsule. Very promising results have been obtained both with sputtering and electroplating. The details of these advances are described elsewhere.[8,9]

In addition to improving the materials used in the Apollo targets, we must develop techniques to increase the precision with which the targets are assembled.

More advanced versions of Apollo will require the hemispheres to be matched in thickness and diameter within a few tenths of a micrometer. The fuel capsule will have to be centered to approximately the same accuracy. Figure 4-14 shows an assembly station we are developing to improve the alignment of the hemispheres as they are assembled around the fuel capsule. The two hemispheres are held on opposing vacuum chucks and carefully aligned with each other before the fuel-capsule sandwich is inserted between them. Using high-power optical microscopes we are able to consistently reposition the hemispheres to within 1 μm. We are designing interferometric viewing optics that will allow us to position the surface of the second shell with an accuracy of about 0.1 μm during the assembly process.

Author: B. W. Weinstein

Major Contributors: J. B. Bryan, C. E. Durbin, E. Hagaman, C. W. Hatcher, G. W. Heaton, A. Hernandez, T. D. Jones, L. L. Lorensen, E. McCann, W. L. Ramer, and C. Walkup

References

5. *Laser Program Annual Report—1979*, Lawrence Livermore National Laboratory, Livermore, Calif., UCRL-50021-79 (1980), pp. 4-2 to 4-8.
6. R. L. Woerner, V. F. Draper, J. C. Koo, and C. D. Hendricks, *Fabrication of Glass Spheres for Laser Fusion Targets*, Lawrence Livermore National Laboratory, Livermore, Calif., UCRL-83395 (1979).
7. *Laser Program Annual Report—1979*, Lawrence Livermore National Laboratory, Livermore, Calif., UCRL-50021-79 (1980), pp. 4-29 to 4-35.
8. S. F. Meyer, E. J. Hsieh, and R. J. Burt, *RF Magnetron Sputtering of Thick Platinum Coatings on Glass Microspheres*, Lawrence Livermore National Laboratory, Livermore, Calif., UCRL-83532 (1979).
9. J. D. Illige, C. Yu, and C. W. Hatcher, *Electroplating for Laser Fusion Targets*, Lawrence Livermore National Laboratory, Livermore, Calif., UCRL-83356 (1979).

Fig. 4-14. (a) Assembly stations for improved alignment of Apollo target second shells. The hemispheres are first placed on the central flat vacuum chuck (b) to assure that their faces are parallel. They are then transferred to the two opposing vacuum chucks for assembly around the inner shell.

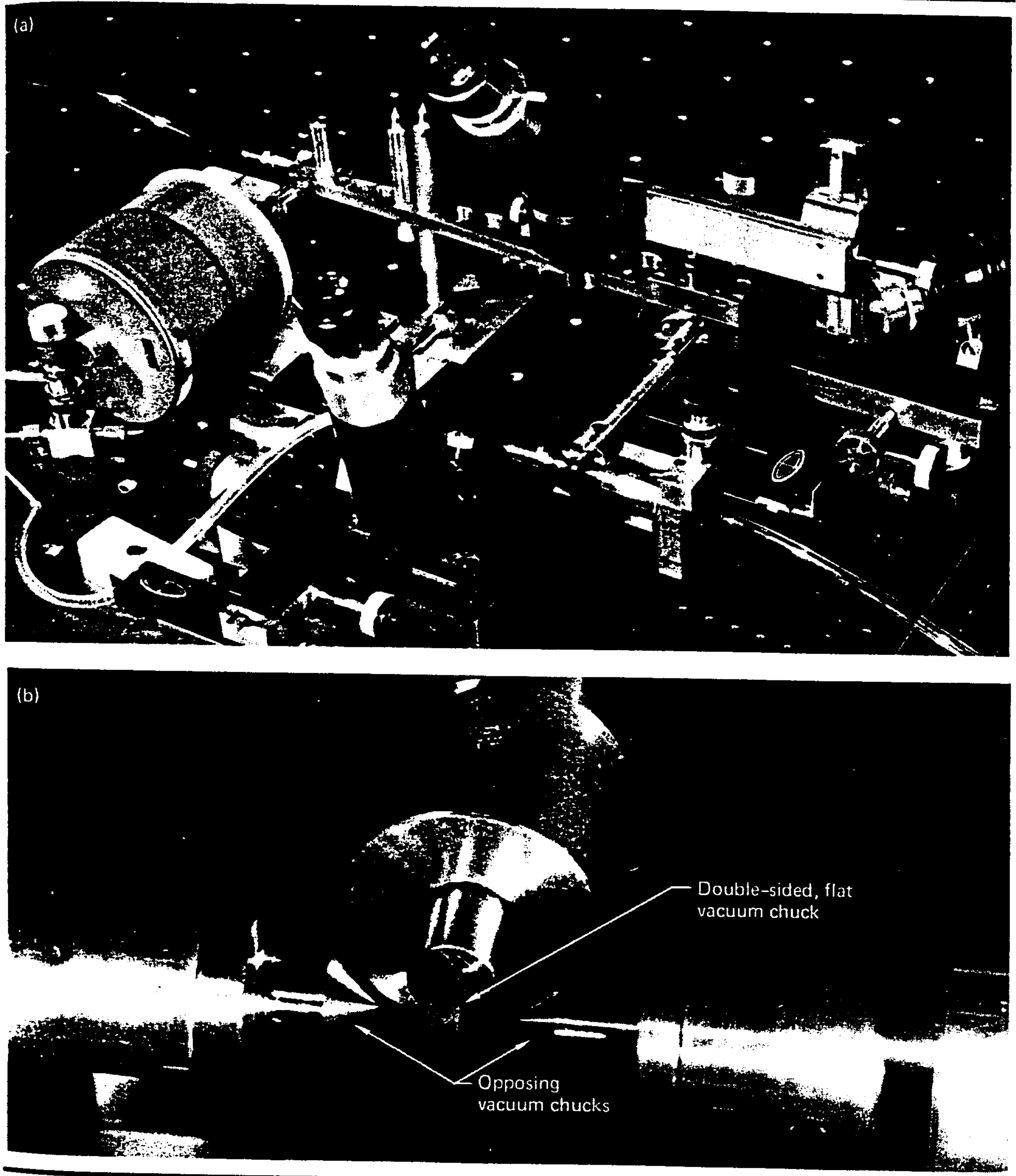

Fusion Experiments and Analysis 5

Introduction

In 1979, our program had two focuses: (1) radiation implosion of D-T to record high densities (50 to 100 times liquid D-T density) and (2) determination of the scaling of hot electrons and thermal radiation in hohlraums.

Shiva experiments in late 1978 saw the Cairn single-shell, radiation-imploded target achieve high enough neutron yields for the compressed D-T density to be inferred from radiochemical diagnostics of the glass pusher. When we performed these diagnostics in the first few months of 1979, we found that densities of at least 50 times liquid D-T density were being achieved.

We compared the densities inferred from radiochemical diagnostics with densities inferred from x-ray imaging diagnostics for a series of experiments in which the D-T was compressed to about 10 times (10×) liquid density. In general, agreement was good between the various density diagnostics.

In Shiva experiments performed in late 1979, two-shell Apollo targets achieved high enough neutron yields for radiochemical density diagnostics. Subsequent radiochemistry experiments with these targets in early 1980 gave densities greater than 100 times (100×) liquid D-T density.

We also made important progress in hohlraum physics. Our measurements of hohlraum temperature are in good agreement with Marshak scaling models. We have performed diagnostic hole-closure experiments to determine appropriate corrections for the hohlraum temperature measurements. The results of hohlraum experiments to determine ablation pressure, hot-electron and x-ray preheat, and the initial stage of the pusher motion are in good agreement with LASNEX calculations.

We performed various experiments to determine the origin and scaling of suprathermal electrons in the hohlraum. These experiments confirmed theoretical predictions that confinement of the plasma blowoff would substantially increase production of suprathermal electrons. We also explored the effects of pulse duration, hohlraum size, beam energy, and focusing strategy on the fraction of laser energy converted to hot electrons, on the hot-electron temperature, and on the time delay of the hot electrons relative to the laser pulse. We have developed a scaling model that is, in general, in good agreement with the data.

Authors: H. G. Ahlstrom and J. H. Nuckolls

10× and 100× Cairn Experiments

Introduction

Since the Shiva target-irradiation facility became operational late in 1978, over 40% of its experimental time has been devoted to the performance testing of a soft x-radiation-driven target design known as Cairn. It was for such experiments that Shiva's two-beam cluster design was originally chosen. According to LASNEX simulations, nonuniformities in the individual laser beams, energy imbalances between beams, and even differences of several percent in summed beam-cluster energies should be tolerable with the Cairn design.

Fig. 5-1. Cairn Mod B irradiation geometry. Here 20 beams—10 each from the upper and lower clusters of the Shiva facility—irradiate the target. [illegible] holds the fuel ball, while the five outer beams of each cluster [illegible] the laser energy [illegible] radiation case, heating [illegible] blackbody temperatures near 200 eV [illegible] radiation then passes through the [illegible] parylene cylinder [illegible] absorbed by the capsule ablator.

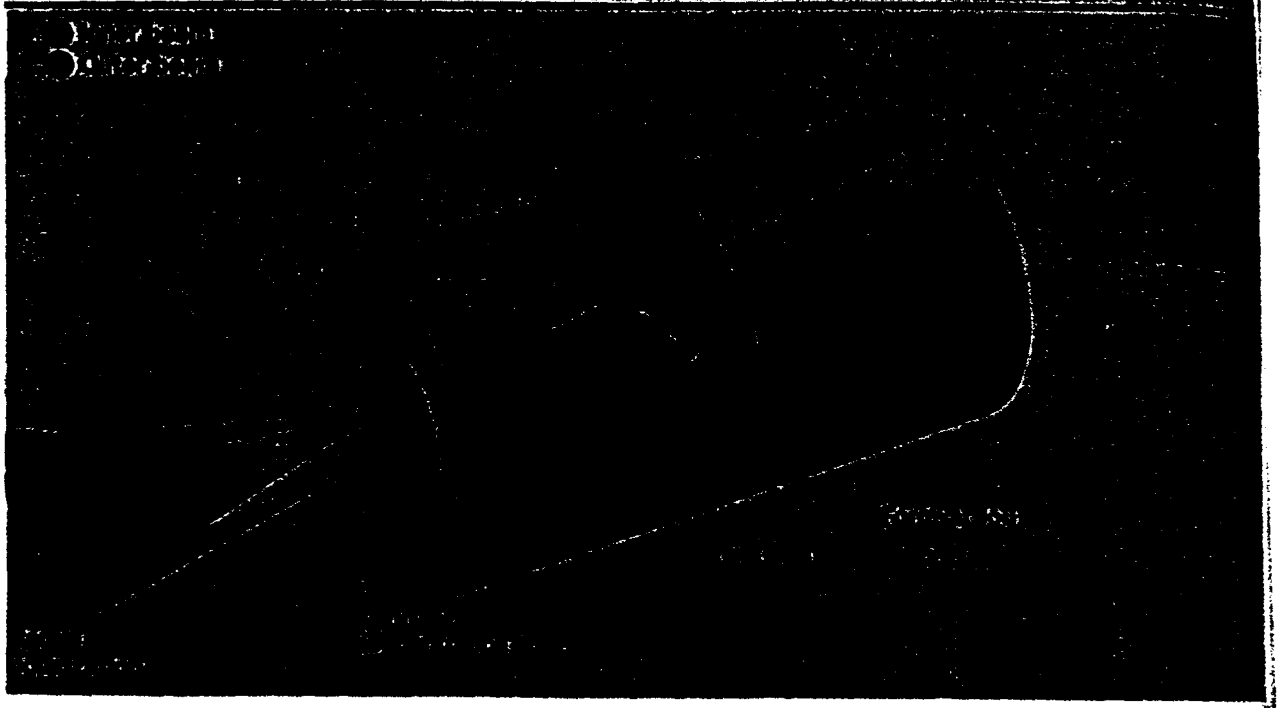

The first Cairn design to be tested extensively (Mod B) is shown in Fig. 5-1. In this design, laser energy is absorbed primarily in the gold walls of the radiation case, heating them to equivalent blackbody temperatures near 200 eV. Then this soft x radiation passes through the heated parylene cylinder surrounding the fuel ball and is absorbed by the capsule ablator.

Cairn B emerged from a November-December 1978 screening exercise as the most likely candidate to achieve at least 10 times liquid D-T density at the Shiva laser facility.[1] Its gold scattering cones intercept the inner cluster of five laser beams on each side of the radiation case, and a thin-walled (2 μm or less in thickness) parylene cylinder prevents laser light from illuminating the fuel ball directly (Fig. 5-1). Such shielding was intended to protect the radiation-driven capsule from hot "glints" of focused laser light that would cause deleterious asymmetries in the implosion. With this design, our primary density diagnostic, radiation chemistry, soon began giving us pusher $\rho_p\Delta R$ values consistent with final fuel densities of about 6 to 10 g/cm^3, or 30 to 50 times liquid D-T density.

Neutron yields from the Cairn B were marginal, however, and large experimental uncertainties clouded the data. To increase drive at the sacrifice of symmetry, we conceived the Cairn H design illustrated in Fig. 5-2—basically a Cairn B with the gold scattering cones and parylene light shield removed—and arranged Shiva's beams in a ring to avoid the fuel ball. Calculations indicated that a modest increase in neutron yield coupled with a slight decrease in final fuel density might be expected. Experimentally, however, the neutron yield jumped over a decade. Greatly improved counting statistics enhanced the quality of the experimental radiochemistry data, and the measured pusher $\rho_p\Delta R$ dropped by about a factor of two. LASNEX was initially unable to reconcile the differences between the two Cairn designs, so we obtained additional data on targets whose scale size was varied, on targets with different fuel balls, on Cairn designs having scattering cones and no parylene cylinder (Mod J), and on Cairn designs with a parylene cylinder and no scattering cones (Mod I). By year's end, we had found a set of model assumptions that reproduced the bulk of the observations. This article summarizes the experimental data and provides a theoretical framework for understanding the central results.

Fig. 5-2. Cairn Mod H irradiation geometry. Basically a Cairn B target, the Cairn H has no parylene cylinder or scattering cones. Thus, Shiva's beams must be arranged in a ring to avoid the fuel ball.

[redacted]

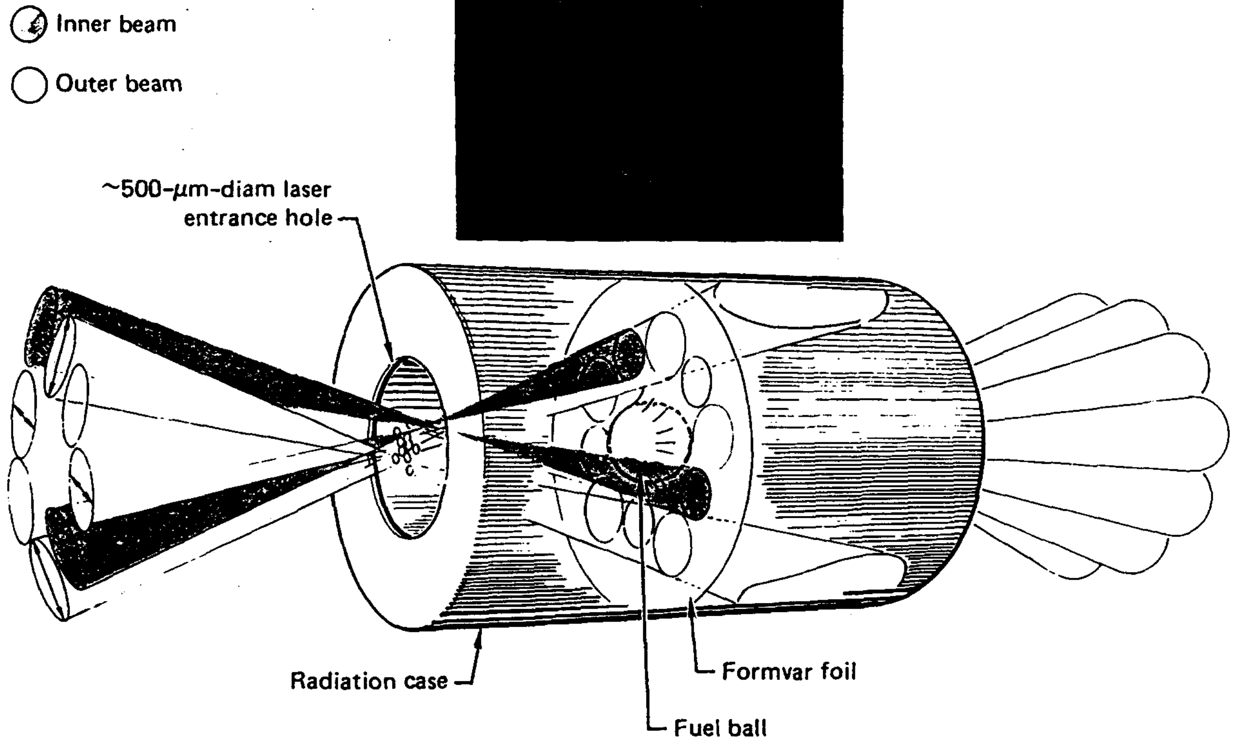

Focusing Geometries

Cairn targets are irradiated by the 20 beams of both the upper and lower clusters of the Shiva facility. In the Cairn B design, the five inner beams of each cluster irradiate the gold scattering cones that cap the ends of a parylene cylinder in which the fuel ball resides, and the five outer beams irradiate the formvar membrane that supports the parylene cylinder (Fig. 5-1). The rationale behind this focusing scheme is to minimize irradiation intensity on the gold scattering cones and therefore lower the suprathermal electron preheat level while, at the same time, observing that the best focus of the beam should remain as close as possible to the plane of the laser entrance hole. In practice, suprathermal x-ray signals are not strongly sensitive to focusing geometry. An example of this standard focusing scheme is shown in Fig. 5-3, whose three parts were generated while calculating an alignment geometry for a particular 2.5 Cairn B target. The notation "S" Cairn B identifies this target as one with a Mod B interior whose radiation case dimensions have been scaled linearly S times the original Cairn target design.[2] For example, a 1.0 Cairn is 800 μm long and 500 μm in diameter with a 250-μm-diam laser entrance hole while a 2.5 Cairn is 2.0 mm long and 1.25 mm in diameter with a 625-μm-diam laser entrance hole. The calculated irradiation patterns are all fivefold symmetric in planes perpendicular in the vertical target axis. Figure 5-3(a) shows the calculated irradiation pattern in the laser entrance hole, Fig. 5-3(b) shows the pattern on the plane of the formvar foil, and Fig. 5-3(c) shows the pattern on the gold scattering cones.

The actual alignment of a Cairn target proceeds in four steps:

Fig. 5-3. The 2.5 Cairn B alignment geometry causes Shiva's beams to diverge into the gold can. Shown here is the calculated irradiation pattern (a) in the laser entrance hole, (b) on the plane of the formvar foil, and (c) on the gold scattering cones.

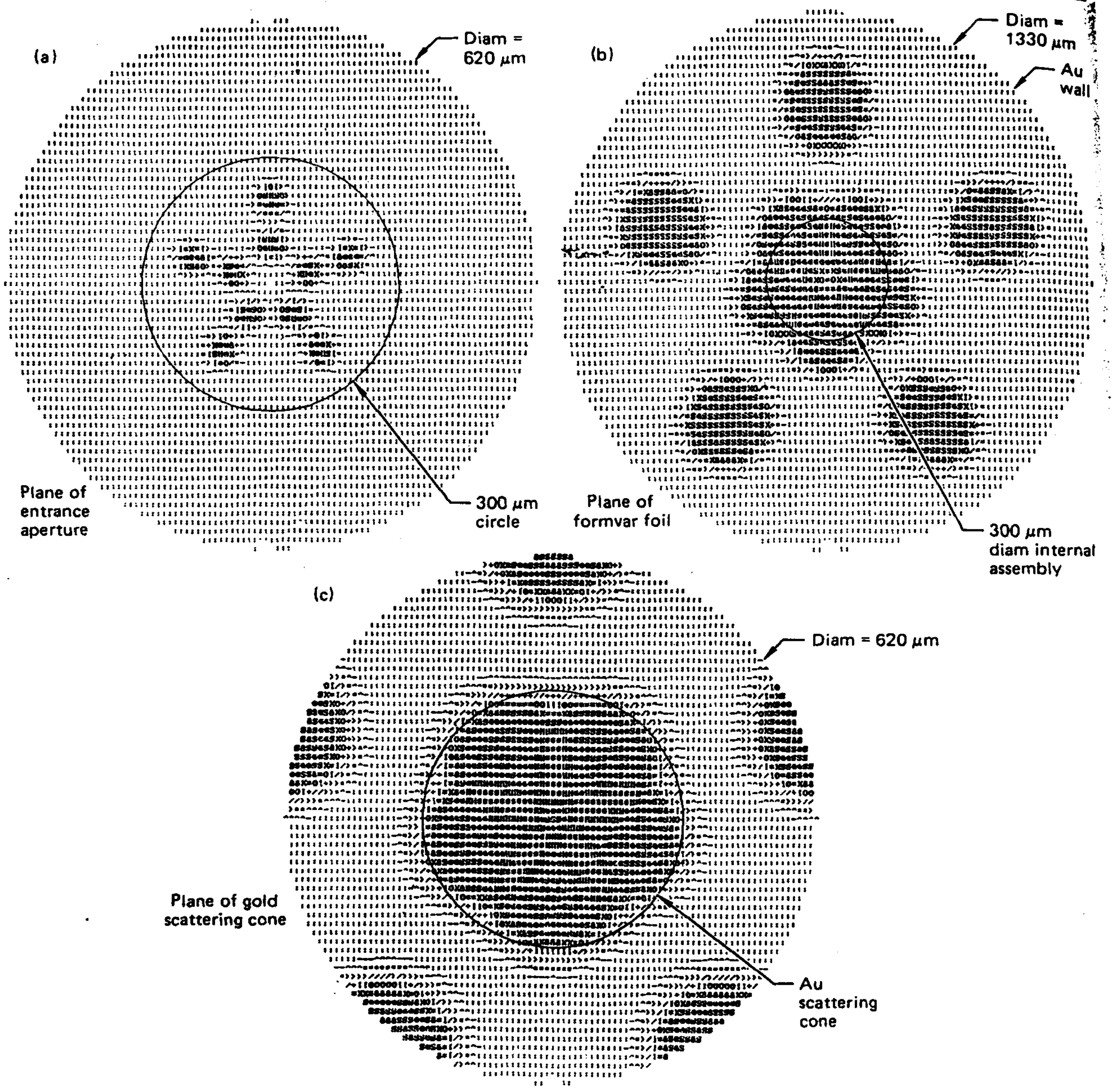

Fig. 5-4. While the Cairn H alignment geometry is similar to that of the Cairn B, the laser beams are directed away from the capsule. Shown here is the calculated irradiation pattern in the midplane of a 2.0 Cairn H target.

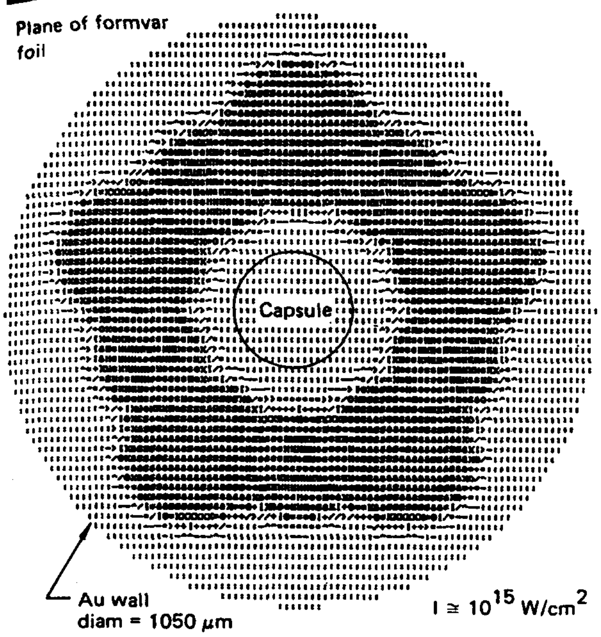

1. The required offsets of the beam best foci (with respect to the center of the target chamber) are determined from a scaled target drawing. This also determines the offsets and beam diameters at the laser entrance hole.

2. The beams are centered by means of a surrogate ball mounted on the same target stalk as the actual Cairn target.

3. The required beam-offset data are fed into a microprocessor that controls lens preset positions. With the help of alignment flags located on the Cairn target, the target alignment for each individual beam is verified by comparing the actual offset and beam diameter at the laser entrance hole with the values computed in step 1. Minor corrections are made to the lens position to ensure that the requirements of the visual verification are satisfied. This gives a "current" position for each lens.

4. Alignment is complete when the verified "current" position of each beam matches the desired irradiation conditions.

Alignment of a Cairn H target proceeds identically, except that different offsets are specified in step 1. Figure 5-4 shows the calculated irradiation pattern in the midplane of a particular 2.0 Cairn H. Although the laser spots initially miss the capsule by more than 50 μm, plasma filling the target can cause some laser energy to refract onto the fuel ball.

Generally, all Cairn designs are irradiated with the maximum laser energy that will not damage the laser at a pulse length of 600 ps (i.e., 7 to 9 kJ).

Occasional checks consistently showed 80 ± 10% laser light absorption. An x-ray microscope in the north polar position ($\theta = 0$) recorded any misalignment of the upper beam cluster that caused laser light to impinge on the outside of the radiation case. Figure 5-5 shows two representative color-enhanced images. Slight clipping at the laser entrance hole, caused by decentering of the fuel ball, did not appear to alter the measured final fuel conditions significantly. The implosion "spike" is clearly visible in both images and appears symmetric. Variations in focusing geometry, such as those shown in Fig. 5-5, likewise had little effect. However, decentering of the fuel ball did pose a serious problem for diagnostics that depended on small diagnostic ports in the radiation case, as will be noted below. The misalignments observed were far outside design-fabrication tolerances, and their cause has yet to be discovered.

Capsule Environment

The five Cairn radiation-case geometries illustrated in Fig. 5-6 were irradiated with a range of incident laser energies that provided a variety of drive and preheat environments for the Cairn capsules. Most of the Cairn capsules were nearly perfect SiO_2 ($\rho \cong 2.2$ g/cm^3) microshells that had a nominal inside diameter of 140 μm and 5-μm-thick walls. They were generally overcoated with 15 μm of $CF_{1.4}$ (Teflon, $\rho \cong 1.8$ g/cm^3) and filled with about 10 mg/cm^3 (about 50 atm) of equimolar D-T. In the following paragraphs, capsules are often characterized by their inside diameter, by their wall thickness, and by their ablator thickness and material; e.g., the nominal capsule described above is designated as a 140 × 5 + 15 CF ball.

Table 5-1 summarizes the Cairn targets we irradiated at the Shiva laser facility during 1979. Neutron yields and fuel densities changed dramatically as target geometries were varied.

Fig. 5-5. (a) Usual Cairn Mod H irradiation geometry. (b) Cairn Mod H irradiation geometry with spots separated on the formvar foil. Note that slight clipping at the laser entrance hole, caused by decentering of the fuel capsule, had no significant effect on the measured final fuel conditions. The implosion spike, clearly visible in both pictures, appears symmetric.

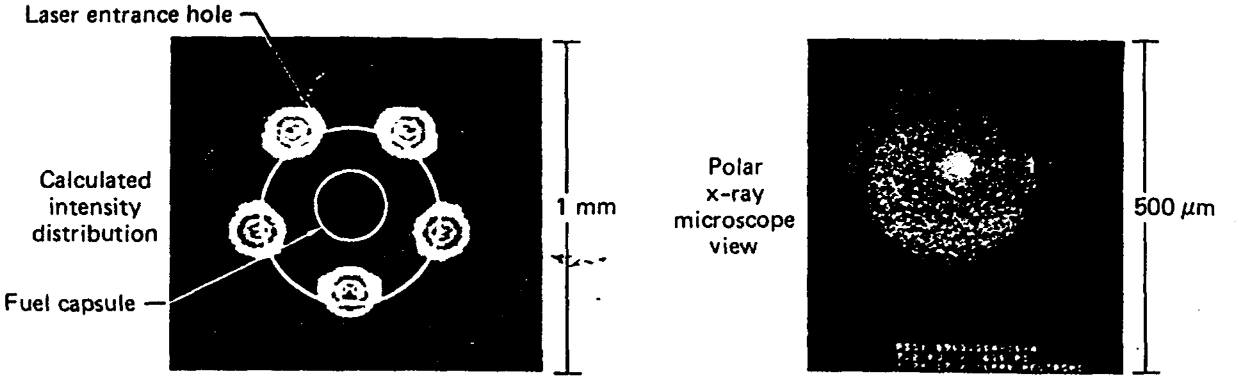

(a) Usual Cairn Mod H irradiation geometry

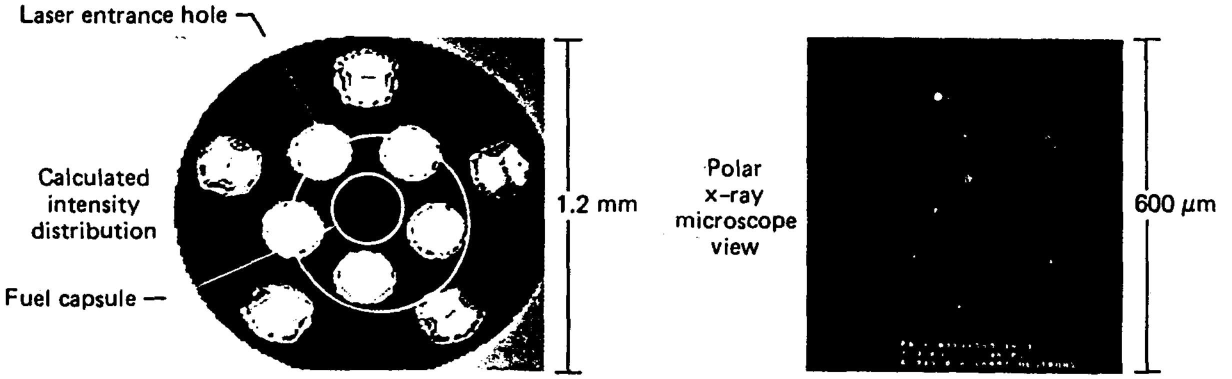

(b) Cairn Mod H irradiation geometry with spots separated on the formvar foil

Presumably, these variations are grossly related to the levels of soft x-ray and thermal electron drive and to the amounts of suprathermal electron and x-ray preheat experienced by the capsule. However, single-parameter vs single-parameter plots (e.g., neutron yield plotted against measured soft x-ray drive) do not reveal simple dependencies.

Drive. Systematic trends do exist, however. For example, soft x-ray drive scales approximately according to the simple Marshak scaling law described in "Theoretical Modeling" in Section 2. As Fig. 5-7 indicates, the power density experienced by the capsule (inferred from DANTE measurements[3]) scales with $10E/S^2(2/\tau)^{1/2}$, where E is the absorbed laser energy in kilojoules, S is the Cairn scale factor, and τ is the laser pulse FWHM (full width at half maximum) in nanoseconds. For values of this parameter of less than about 30, the scaling is reasonable. As the parameter increases, however, the available data suggest a flattening of the drive curve, possibly caused by an efficient transfer of laser energy into the suprathermal electron population. Since many of the Cairn experiments were conducted in this regime, a blind application of the Marshak scaling law may tend to overestimate the drive.

This simple scaling indicates the maximum radiation temperature that should be reached during the 600-ps-wide (approximately) laser pulse. It does not, in any simple way, give the time dependence of the x-rays. In general, the calculated performance of the capsules shows considerable sensitivity to the temporal profile of the x rays, particularly to the rise time of the leading edge. Lack of experimental determination of this profile forces the designer to use LASNEX-determined profiles, which are known to be dependent on such poorly understood phenomena as laser absorption in the

Fig. 5-6. Radiation cases for five Cairn targets: the Mod B, H, I, J, and K. When irradiated with a range of incident laser energies, they provided a variety of drive and preheat environments for the Cairn capsules, most of which were nearly perfect SiO_2 microshells overcoated with 15 μm of Teflon and filled with about 10 mg/cm^3 of D-T.

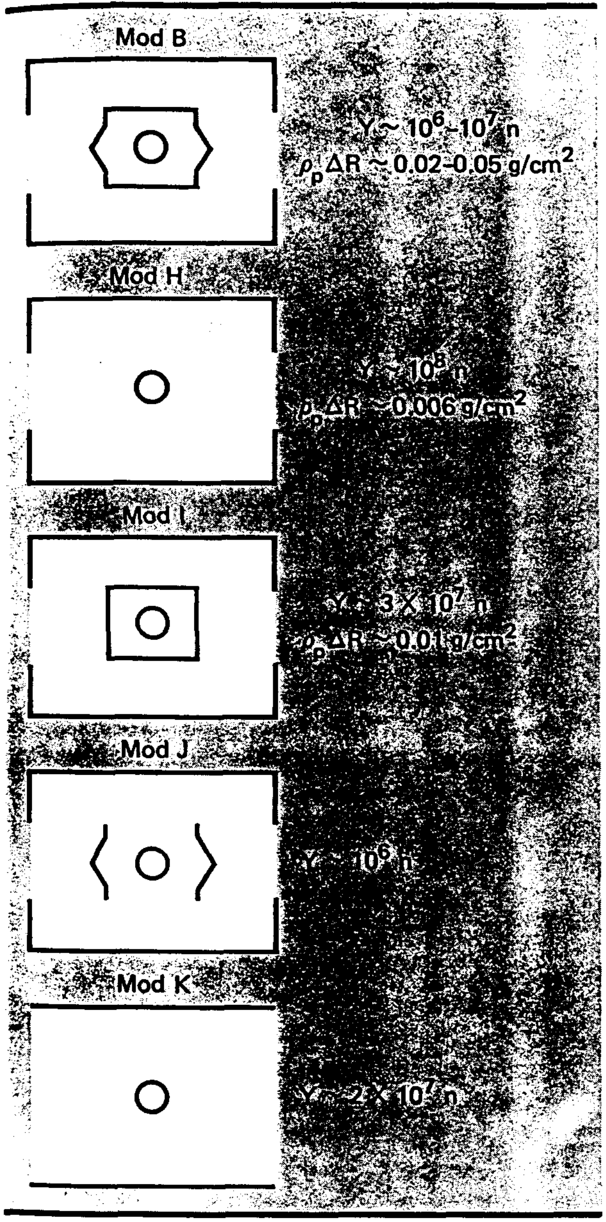

high-Z walls of the hohlraum. In addition, the experimental x-ray data do not determine the x-ray flux incident on the capsule as a function of position on the capsule surface. That is, spatial asymmetries in the x-ray flux, and therefore in the radiative drive, have not been determined experimentally.

Fig. 5-7. Soft x-ray drive scales with the Marshak parameter up to values near 30, at which the hohlraum temperature approaches 200 eV. Beyond 30, the drive appears to saturate in these Cairn targets.

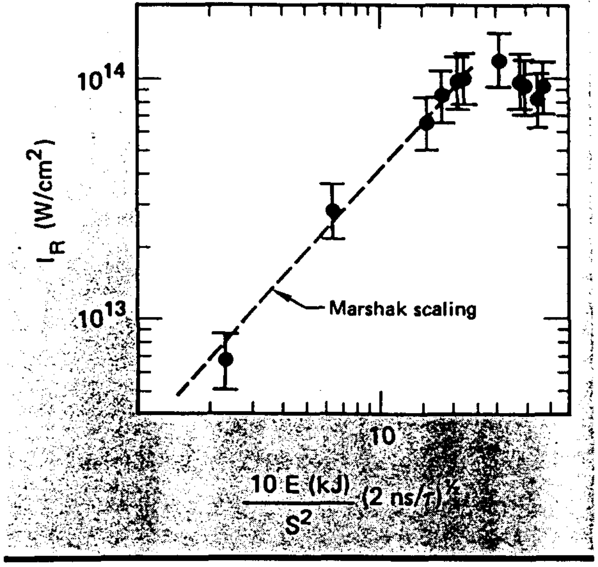

Suprathermal Preheat. As will be pointed out in "Cairn Scaling Study—The Experiments" (see Section 5), the suprathermal x-ray flux at 50 keV can be used to estimate the preheat level experienced by the capsule. Although far from an exact determination, this preheat level is nonetheless a useful indicator. In the simplest approximation, the fraction of laser energy coupled into suprathermal electrons, f_{Hot}, is directly proportional to the x-ray flux detected at an energy corresponding to the temperature, θ_H, of the distribution.

The Cairn targets probably achieved suprathermal temperatures of between 50 and 60 keV; therefore the x-ray flux at 50 keV is tabulated in Table 5-1. Although there is once again much scatter in the data, Fig. 5-8 shows that the Cairn targets often operated near $f_{Hot} = 1.0$ (i.e., at virtually all of the laser energy in fast electrons). Saturation of this curve is required since no more than all of the absorbed energy can reside in fast electrons. As noted in "Cairn Scaling Study" (see Section 5), these data scale empirically with E/S^3, or energy per unit volume.

We offer no theoretical justification for the choice of E/S^3 as a scaling parameter; it merely clusters the data. From the plots of drive and suprathermal x-ray level, it appears that Cairn targets generally operate near drive "saturation."

Table 5-1. Cairn summary for 1979.

Shot No.	Cairn target	E_L, kJ τ_L, ns (±10%)	Yield	I_R, W/cm^2 (±30%)	f_{50}, keV/keV (±25%)	$\rho_p \Delta R$, g/cm^2	ρ_{Peak} g/cm^3
88120602	2.5 B 146 × 4.4 + 17.3 CF	8.4/0.71	$(4.6 \pm 1.8) \times 10^6$				
89011803	2.5 BA 141 × 4.5 + 14.5 CF	6.8/0.70	$(9.1 \pm 2.4) \times 10^5$				
89011805	2.5 B 180 × 5.2 + 14.5 CF	8.0/0.60	$(1.06 \pm 0.12) \times 10^7$				
89012204	2.5 BA	7.7/0.62	$(8.4 \pm 1.1) \times 10^6$				
89012303	2.5 BA	7.5/0.66	5×10^5				
89012509	2.5 B 135 × 4.3 + 15.4 CF	7.9/0.60	$(3.6 \pm 0.5) \times 10^6$				
89013103	2.5 BA	6.1/0.68	$(5.4 \pm 1.9) \times 10^5$				
89020103	2.5 BA	6.3/0.65	$(7.6 \pm 0.9) \times 10^6$				
89020203	2.5 B 148 × 4.8 + 14.5 CF	6.5/0.64	$(2.9 \pm 0.5) \times 10^6$				
89020504	2.5 B 142 × 4.8 + 14.5 CF	8.7/0.63	$(6.0 \pm 0.8) \times 10^6$				
89020703	2.5 B 140 × 4.5 + 15.2 CF	7.8/0.63	$(1.3 \pm 0.3) \times 10^6$		8.0×10^{14}		
89020804	2.5 BA	7.5/0.64	$(2.1 \pm 1.5) \times 10^5$				
89020905	2.5 B 141 × 4.6 + 13.7 CF	5.9/0.59	$(7.7 \pm 1.5) \times 10^5$		3.0×10^{14}		
89020908	2.0 B 144 × 4.8 + 16.1 CF	7.8/0.59	$(3.4 \pm 1.1) \times 10^6$			$0.028^{+0.03}_{-0.01}$	$7<12<28$
89021203	2.0 B 144 × 3.2 + 17.3 CF	7.4/0.68	$(6.9 \pm 1.2) \times 10^6$				
89021206	2.5 B 127 × 6.6 + 14.7 CF	7.0/0.66	$(7.4 \pm 1.9) \times 10^5$				
89021405	2.5 B 144 × 4.9 + 16.5 CF	7.0/0.60	$(1.9 \pm 0.4) \times 10^6$				
89021409	2.5 B 141 × 5.3 + 13.1 CF	7.0/0.61	$(1.2 \pm 0.4) \times 10^6$				
89022004	2.0 B 138 × 4.0 + 15.6 CF	6.7/0.63	$(1.3 + 0.9) \times 10^6$			$0.079^{+0.055}_{-0.058}$	$11<34<62$
89022006	2.0 B 147 × 4.6 + 16.5 CF	7.1/0.54	$(3.4 \pm 1.1) \times 10^6$			$0.0123^{+0.021}_{-0.012}$	$0.0<4.0<14$
89022604	2.0 H 143 × 4.6 + 14.2 CF	7.6/0.58	$(8.8 \pm 1.0) \times 10^8$				
89022606	2.0 BA	6.6/0.6	$(1.5 \pm 0.2) \times 10^7$				
89022704	2.0 H 141 × 4.9 + 17.2 CF	7.3/0.625	$(9.2 \pm 1.1) \times 10^7$			$0.009^{\pm 0.0013}_{\pm 0.0021}$	3.6 ± 0.9
89022709	2.0 BA	6.7/0.625	(1.6 [illegible] 0.2) × 10^7				

Table 5-1. **Continued.**

Shot No.	Cairn target	E_L, kJ τ_L, ns (±10%)	Yield	I_R, W/cm^2 (±30%)	f_{50}, keV/keV (±25%)	$\rho_p \Delta R$, g/cm^2	ρ_{Peak} g/cm^3
89022802	2.5 B 134 × 4.8 + 17.4 CF	8.0/0.65	$(4.0 \pm 0.7) \times 10^6$	8.4×10^{13}	1.3×10^{15}		
89022808	2.0 B 138 × 5 + 14.5 CF	8.0/0.59	$(2.8 \pm 1.0) \times 10^6$			0.0134 ± 0.021	0<4.6<14
89030104	2.0 B	1.3/0.70	$<10^{-5}$				
89030108	2.0 B 135 × 5 + 13 CF	7.4/0.48	$(9.4 \pm 1.4) \times 10^6$	1.2×10^{14}	3.8×10^{15}		
89030202	2.0 HA 138 × 5 + 13 CF	7.5/0.59	$(3.6 \pm 0.7) \times 10^7$				
89030213	2.5 B 141 × 4.2 + 13.7 CF	9.1/0.62	$(7.1 \pm 1.3) \times 10^6$	9.4×10^{13}			
89030505	2.0 HA	4.7/0.56	$(4.8 \pm 0.6) \times 10^7$				
89030509	2.0 B	6.0/0.61	2.5×10^6	9.6×10^{13}			
89031207	2.5 B 150 × 4 + 16.3 CF	7.3/0.72	$(5.1 \pm 1.9) \times 10^5$	6.4×10^{13}	5.2×10^{14}		
89031211	2.0 B 144 × 4.5 + 13 CF	8.2/0.65	$(7.0 \pm 1.0) \times 10^6$			0.020 ± 0.007	7.6 ± 2.2
89031304	2.0 H 143 × 5.1 + 11.7 CF	7.2/0.63	$(1.7 \pm 0.17) \times 10^8$			0.0095 ± 0.0020	3.9 ± 1.0
89031406	2.0 H 137 × 4.1 + 15.6 CF	7.2/0.78	$(3.1 \pm 0.4) \times 10^7$			0.0115 ± 0.0038	4.9 ± 1.9
89031505	2.5 H 140 × 5 + 12.6 CF	7.3/0.78	$(6.9 \pm 0.8) \times 10^7$			0.0049 ± 0.0017	1.8 ± 0.8
89031508	2.5 H 144 × 4.6 + 13 CF	7.7/0.58	$(1.14 \pm 0.12) \times 10^8$			0.0052 ± 0.0016	1.8 ± 0.8
89031904	2.0 H 145 × 2.5 + 8.8 CF	7.8/0.59	$(1.32 \pm 0.14) \times 10^8$				1.8(ALICS)
89031907	2.0 H 136 × 3.9 + 11.5 CF	7.0/0.63	$(3.9 \pm 0.6) \times 10^7$				
89032006	2.0 B 138 × 5 + 13 CF	7.9/0.58	$(4.9 \pm 1.1) \times 10^6$				
89032102	2.0 H 145 × 4.1 + 11.1 CF	7.6/0.54	$(2.0 \pm 0.2) \times 10^8$				
89032104	2.0 B 140 × 5 + 53 CH	6.8/0.6	$(8.7 \pm 1.6) \times 10^6$			0.026 ± 0.010	10 ± 5
89032206	2.5 B Apollo	8.8/0.8	$<10^{-5}$				
89032212	2.0 H 144 × 1.8 + 21 CF	7.0/0.59	$(1.50 \pm 0.15) \times 10^8$				
89032305	2.0 H 141 × 1.7 + 21 CF	6.5/0.59	$(1.48 \pm 0.15) \times 10^8$				

Table 5-1. Continued.

Shot No.	Cairn target	E_L, kJ τ_L, ns (±10%)	Yield	I_R, W/cm^2 (±30%)	f_{50}, keV/keV (±25%)	$\rho_p \Delta R$, g/cm^2	ρ_{Peak} g/cm^3
89032309	2.0 H 140 × 5 + 110 CF	6.9/0.66	$<10^5$				
89082306	2.0 H 143 × 4.6 + 14.5 CF	7.3/0.60	$(1.62 \pm 0.16) \times 10^8$				
89083105	2.0 HA	6.3/0.60	$(1.33 \pm 0.13) \times 10^8$				
89090509	2.0 H 145 × 4.4 + 13 CF	6.8/0.58	$(1.43 \pm 0.14) \times 10^8$				
89090603	2.0 I 144 × 4.4 + 14.1 CF	8.0/0.575	$(3.2 \pm 0.5) \times 10^7$				
89090605	2.0 J 145 × 4.2 + 13 CF	7.4/0.5	$(1.18 \pm 0.25) \times 10^7$				
89090705	2.0 HA	7.3/0.60					
89090708	2.0 HA	7.9/0.59					
89091004	2.0 J 144 × 4.5 + 13.9 CF	7.4/0.60	$(1.88 \pm 0.28) \times 10^7$			0.005 ± 0.004	
89091007	2.0 H 138 × 4.3 + 15.6 CF	7.6/0.60	$(1.59 \pm 0.16) \times 10^8$			0.0068 ± 0.0024	2.6 ± 1.2
89091302	2.0 HA	6.4/0.60					
89091304	2.0 HA	7.2/0.6					
89091403	2.0 I 147 × 4.9 + 12.2 CF	7.3/0.6	$(3.0 \pm 0.5) \times 10^7$			0.013 ± 0.006	4.4 ± 2.5
89091704	2.0 J 143 × 6 + 14.5 CF	7.7/0.625	$(7.2 \pm 1.4) \times 10^6$				
89091706	2.0 J 138 × 5.1 + 14.8 CF	7.0/0.630	$(1.8 \pm 0.3) \times 10^7$			0.003 ± 0.003	
89091803	2.0 I 142 × 4.7 + 15 CF	5.6/0.625	$(9.3 \pm 3.7) \times 10^5$		7.5×10^{14}		
89092104	2.0 HA	7.3/0.580					
89100405	1.6 B 138 × 4.8 + 148.8 CH	8.3/0.6	$(3.3 \pm 0.6) \times 10^7$	9.2×10^{13}	1.8×10^{15}		
89100409	1.6 B 151 × 5.2 + 50.9 CH	7.8/0.6	$(5.0 \pm 0.8) \times 10^7$	8.0×10^{13}			
89100503	2.0 B 141 × 5 + 50 CH	7.9/0.6	$(2.1 \pm 0.8) \times 10^6$	9.8×10^{13}	1.2×10^{15}		
89100506	2.0 B 159 × 5.5 + 48.6 CH	8.1/0.6	$(6.7 \pm 1.5) \times 10^6$	9.0×10^{13}	1.1×10^{15}		
89100802	3.0 B 155 × 4.9 + 50 CH	1.44/0.6	5×10^5	6.6×10^{12}	4.5×10^{12}		
89100804	3.0 B 148 × 5.3 + 49.7 CH	3.9/0.6	5×10^5	2.8×10^{13}	1.5×10^{12}		

Table 5-1. Continued.

Shot No.	Cairn target	E_L, kJ τ_L, ns (±10%)	Yield	I_R, W/cm^2 (±30%)	f_{50}, keV/keV (±25%)	$\rho_p \Delta R$, g/cm^2	ρ_{Peak} g/cm^3
89100903	2.0 H 115 × 13 + 67 CH	8.2/0.6	$(2.2 \pm 0.8) \times 10^6$		1.3×10^{15}		
89101105	2.5 H Apollo	8.8/1.0	$(1.5 \pm 1.2) \times 10^6$		4.0×10^{14}		
89101504	2.0 K	8.0/0.6 $Ea=0.35E_L$	$(1.5 \pm 0.4) \times 10^6$		2.2×10^{14}		
89101603	2.0 K 138 × 4.6 + 15.2 CF	7.0/0.6 $Ea=.37E_L$	$(1.4 \pm 0.4) \times 10^6$		2.5×10^{14}		

Fig. 5-8. The normalized suprathermal x-ray flux at 50 keV scales with E/S^3 (energy per unit volume). Most of the 2.0 Cairn targets operated near $f_{Hot} \cong 1$ (at virtually all the laser energy in fast electrons).

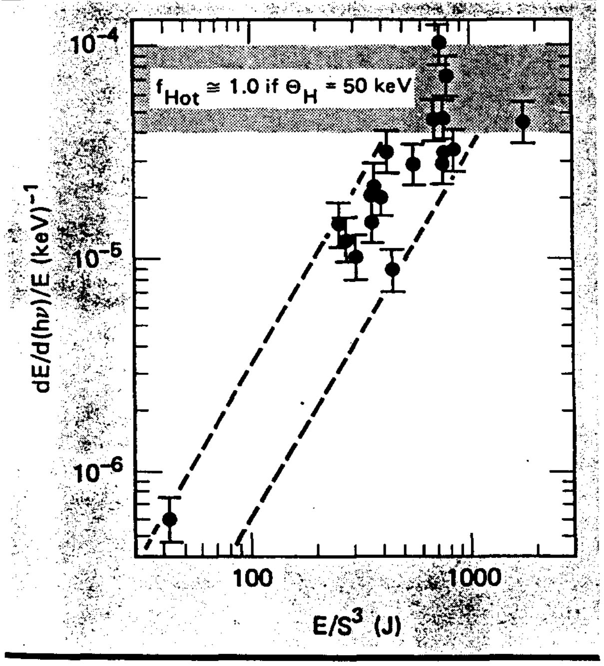

Modeling of Cairn implosions, even in one dimension, is complicated by this choice of operating regime. The Cairn H targets appear to be partially driven by suprathermal electrons, and both the Cairn H and B implosions are degraded by the suprathermal preheat. In addition, a systematic uncertainty of about a factor of two exists in the experimental determination of the x-ray flux at 50 keV as a result of suprathermal x-rays being anisotropically emitted from the targets.

As noted in "Suprathermal Electron Generation in Laser Fusion Target Geometries" (see Section 5), the measured suprathermal x-ray spectrum may change with viewing angle with respect to the axis of the laser beam cluster. These suprathermal x-ray spectra do not uniquely determine parameters of interest to the target designer. The average suprathermal electron energy and the total energy into suprathermals are integrated quantities that do not effectively constrain the time-dependent LASNEX calculations. Moreover, these quantities measure global phenomena that occur throughout the hohlraum volume, while the designer's interest is focused on what happens *at the capsule location.* The relationship between the globally measured suprathermal x-ray flux and the flux of electrons as a function of energy, time, and position on the capsule surface is poorly understood.

Ultra-High-Energy Preheat. During January-March 1979, we monitored ultra-high-energy x rays emitted from Cairn targets with the Shiva neutron time-of-flight (TOF) facility. The data obtained provided estimates of x-ray yield and ultra-high temperature based on x rays in the 300- to 700-keV range.

The Shiva neutron TOF spectrometer has two plastic scintillation detectors at the end of 125-m-long flight paths that detect x rays in the 100-keV to 1-MeV range. The system collimation and shielding provide excellent discrimination against x rays and gamma rays formed outside the target region (i.e.,

Fig. 5-9. X-ray transmission through 1/2- and 1-in.-thick lead filters and 125 m of air as a function of x-ray energy. The ratio of the transmissions through the two filters ($T_{1/2}$ to T_1) is dependent on the x-ray energy.

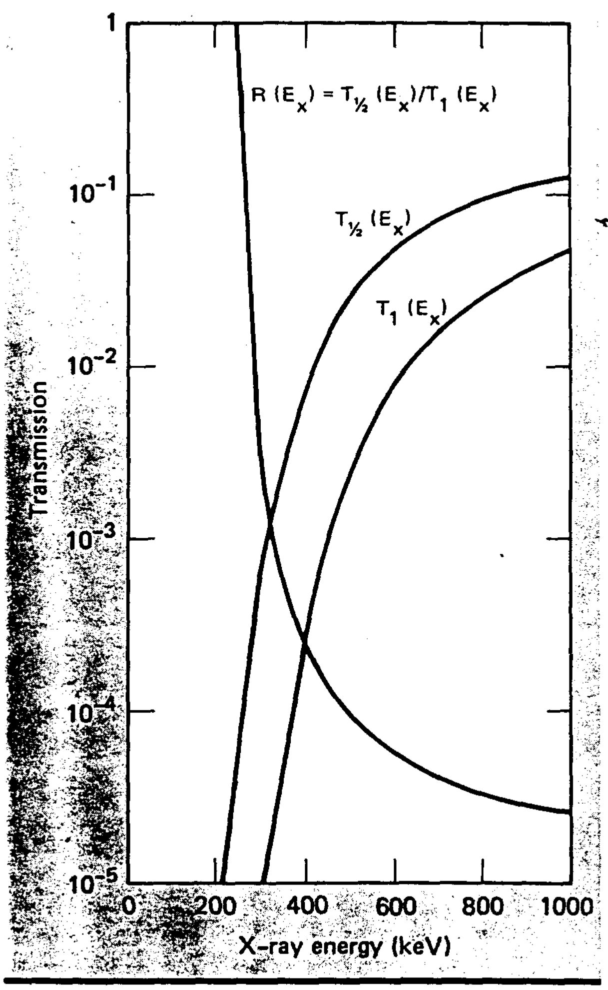

chamber walls, room walls, etc.). To obtain data on the x-ray spectrum above 100 keV, we inserted lead filters between the target and the detectors 80 m from the target. We placed a 1/2-in.-thick filter in one beam path and a 1-in.-thick filter in the other beam path. Figure 5-9 shows the x-ray transmission through the filters and 125 m of air as a function of x-ray energy. The ratio, $R(E_x)$, of the transmissions through the two filter systems is dependent on the x-ray energy E_x. This is also shown in Fig. 5-9.

The energy deposited in a detector, E_{det}, is given by

$$E_{det} = \int_0^{\infty} T(E_x)\,\epsilon(E_x)\left(\frac{dS(E_x)}{dE_x}\right) dE_x \quad , \qquad (1)$$

Fig. 5-10. Ratio of x-ray energy deposition in fluor after passing through 1/2 in. of lead to x-ray energy deposition in fluor after passing through 1 in. of lead versus 1/kT.

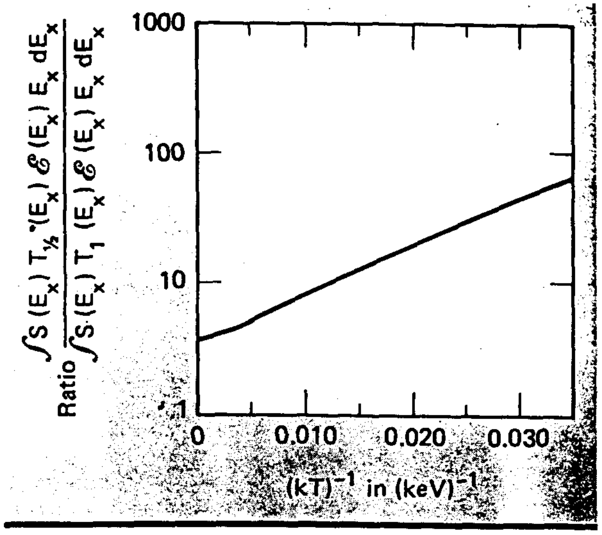

where $T(E_x)$ is the filter transmission, $dS(E_x)/dE_x$ is the source spectrum in energy per unit energy, and $\epsilon(E_x)$ is the detector efficiency. Figure 5-10 shows the ratio of energy deposited in the detectors versus $(kT)^{-1}$ for a source distribution having the form

$$dS(E_x) = S_0 \exp(-E_x/kT) dE_x$$

and a constant detector efficiency for x rays in the range 300 to 1000 keV.

The mean free path (MFP) for 300-keV x rays in plastic is about 8 cm long; that for 800-keV x rays is about 13 cm. These values are similar to the 10-cm-long MFP for 14-MeV neutrons, so energy deposition within the 10-cm detector is similar. The ratio of signals obtained from the two TOF detectors using lead filters provides a means for estimating the temperature of the ultra-high-energy portion of the x-ray spectrum. Figure 5-11 shows the normalized x-ray spectra transmitted for several temperatures by a 1/2-in.-thick piece of lead and 125 m of air. For temperatures of about 50 keV, the detectors are responding to x rays with energy above 300 keV.

Table 5-2 is a summary of the data recorded for Shiva Cairn targets. The measured signal ratios range from 5 to 15, corresponding to temperatures of 60 to 200 keV for a one-temperature model. The spectra in Fig. 5-11 indicate that most of the energy detected by the TOF detectors results from 300- to 600-keV x rays. For comparison, the isotropic source strength of the 500-keV monoenergetic x-ray

Fig. 5-11. X-ray spectra after passage through 1/2-in.-thick lead versus x-ray energy for several values of 1/kT. Initial spectra have the form

$$dS(E_x) = S_0 \exp(-E_x/kT) dE_x.$$

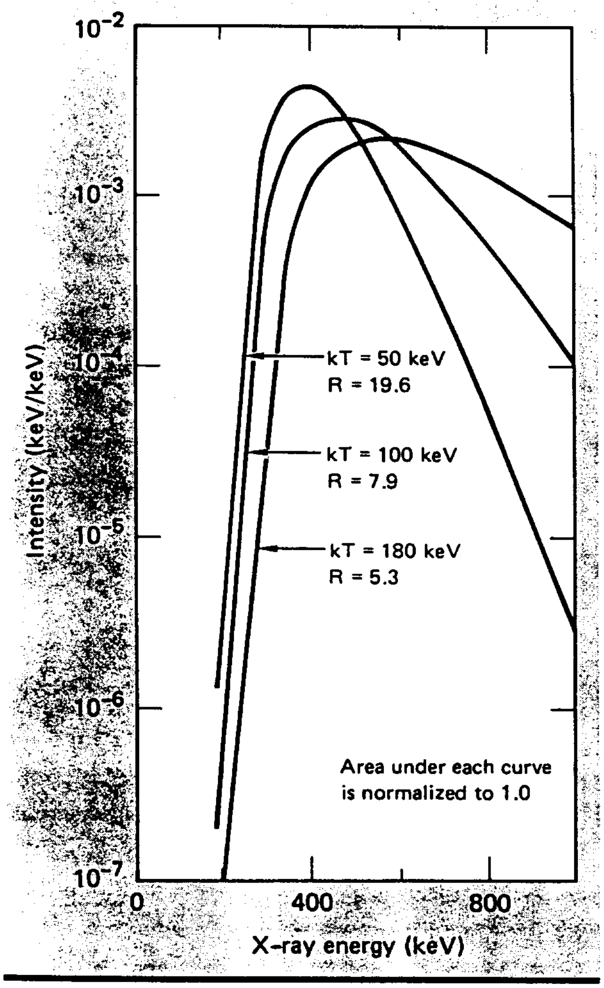

source necessary to produce the observed signals for each shot is listed in Table 5-2. As with the 50-keV FFLEX data mentioned above, these source strengths generally increase with E/S^3 (Fig. 5-12). The x-ray temperature, on the other hand, varies about a mean value of 124 keV with a standard deviation of 37 keV.

Given a typical bremsstrahlung conversion efficiency of about 10^{-2}, these data suggest that between 1.0 and 30.0 J found its way into this ultrahigh-energy electron distribution. It is clear that such energetic electrons cannot be shielded against in the Cairn design, but the preheat they produce is not energetically important. Calculations show that future reactor targets are sensitive to electrons in this energy range, so their production mechanisms must be understood and controlled.

Fig. 5-12. Equivalent 500-keV x-ray source strength generally increases with E/S^3.

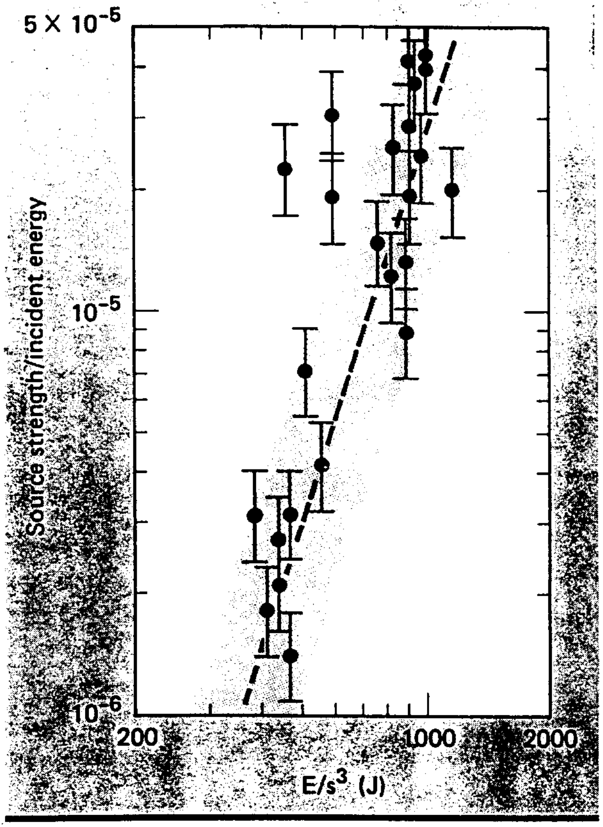

Final Fuel Conditions

The crudest characterization of an ablative implosion reduces to a measurement of the maximum fuel density achieved. Figure 5-13 contrasts the useful ranges of several density-monitoring techniques. While low-density plasmas may be studied with alpha-particle imaging to determine the size, distribution, and shape of the burn region, the alpha particle's large collision cross section with fuel and pusher ions renders this technique virtually useless above density-confinement radius products of about 10^{-3} g/cm^2. The four overlapping shaded areas in the figure—Ar, Br, Si, and Cu—represent radiochemistry operating regimes for argon, bromine, silicon, and copper, which are present in the fuel or the pusher as noted. Argon line imaging through silicate pushers has a useful range exceeding alpha imaging, but only radiochemistry and x-ray backlighting offer promise for measuring the areal densities expected for ≥100× liquid density implosions with the anticipated low ion temperatures.[4]

Table 5-2. Summary of ultra-high-energy x-ray data recorded by the neutron time-of-flight (TOF) system for Cairn targets.

Shot No.	Target	Source strength of 500-keV x-rays, mJ	Detector signal ratio	Temperature, keV
89013103	2.5 B	19.2	—	—
89020103	2.5 B	11.3	6.9 ±0.9	120
89020203	2.5 B	>39.5	—	—
89020504	2.5 B	35.5	8.2 ± 2.4	140
89020905	2.5 B	<3.0	—	—
89020908	2.0 B	>197	—	—
89021203	2.0 B	>197	—	—
89021206	2.5 B	14.7	10.0 ± 1.5	80
89021405	2.5 B	19.2	7.8 ± 2.7	105
89021409	2.5 B	158	<8.0	100
89022004	2.0 B	>197	—	—
89022206	2.0 B	>197	—	—
89022604	2.0 H	>367	—	—
89022606	2.0 B	82	8.3 ± 4	95
89022704	2.0 H	139	12.9 ± 5	65
89022709	2.0 B	169	6.3 ± 3.6	137
89022802	2.5 B	56	—	—
89022808	2.0 B	338	3.9 ± 0.6	200
89030104	2.0 B	<3.0	—	—
89030108	2.0 B	305	4.4 ± 0.8	200
89030202	2.0 B	271	6.3 ± 1.1	135
89030213	2.5 B	169	6.5 ± 1.8	135
89030505	2.0 H	141	8.2 ± 3.6	100
89030507	2.0 B	84	9.8 ± 5.0	80
89031207	2.5 B	22.6	—	—
89031211	2.0 B	158	7.3 ± 2.5	110
89031304	2.0 H	203	5.9 ± 1.2	155
89031406	2.0 H	90	10.5 ± 5	75
89031505	2.5 H	11	—	—
89031508	2.5 H	—	—	—
89031904	2.0 H	186	7.2 ± 2	110
89031907	2.0	62	7.2 ± 3.3	110
89032006	2.0 B	305	5.9 ± 0.8	180

Radiochemistry $\rho_p \Delta R$ Measurements. From Fig. 5-13; it is clear that radiochemistry is a viable method for making pusher $\rho_p \Delta R$ measurements on our present Cairn targets. The total number of activated atoms created in the pusher, N*, is given by

$$N^* = \frac{N_C}{\eta_C \, \eta_D \, e^{-\lambda t_L} (1 - e^{-\lambda \Delta t})} \; .$$

The definitions of these symbols and a discussion of their values follows.

The 16 radiochemistry collector-efficiency calibration shots we did are indicated in Table 5-1 by an "A" (for activated) in the target description. Cylindrical collector foils of titanium, held in place by a matching aluminum carrier, were used for all shots in this series.

We determined collection efficiency as follows: First, we irradiated coated fuel balls at the Livermore reactor for 6 to 10 h in a thermal neutron flux of 7 × 10^{13} n/cm·s, where some of the sodium atoms present in the glass microsphere were converted to radioactive ^{24}Na ($t_{1/2}$ = 15.02 h). Then we found the collection efficiency by comparing the ^{24}Na activity of the fuel ball to that in the collected debris.

The targets for all the collector experiments were Cairn radiation cases, each of which had a 380- to 420-μm-diam hole drilled about 100 μm below its equator to allow capsule debris to eject toward the collector. Each case generally contained 140 × 5 capsules coated with various thicknesses of CF ablator.

Fig. 5-13. Calculated operating regimes for various density diagnostics for ranges of experimental interest.

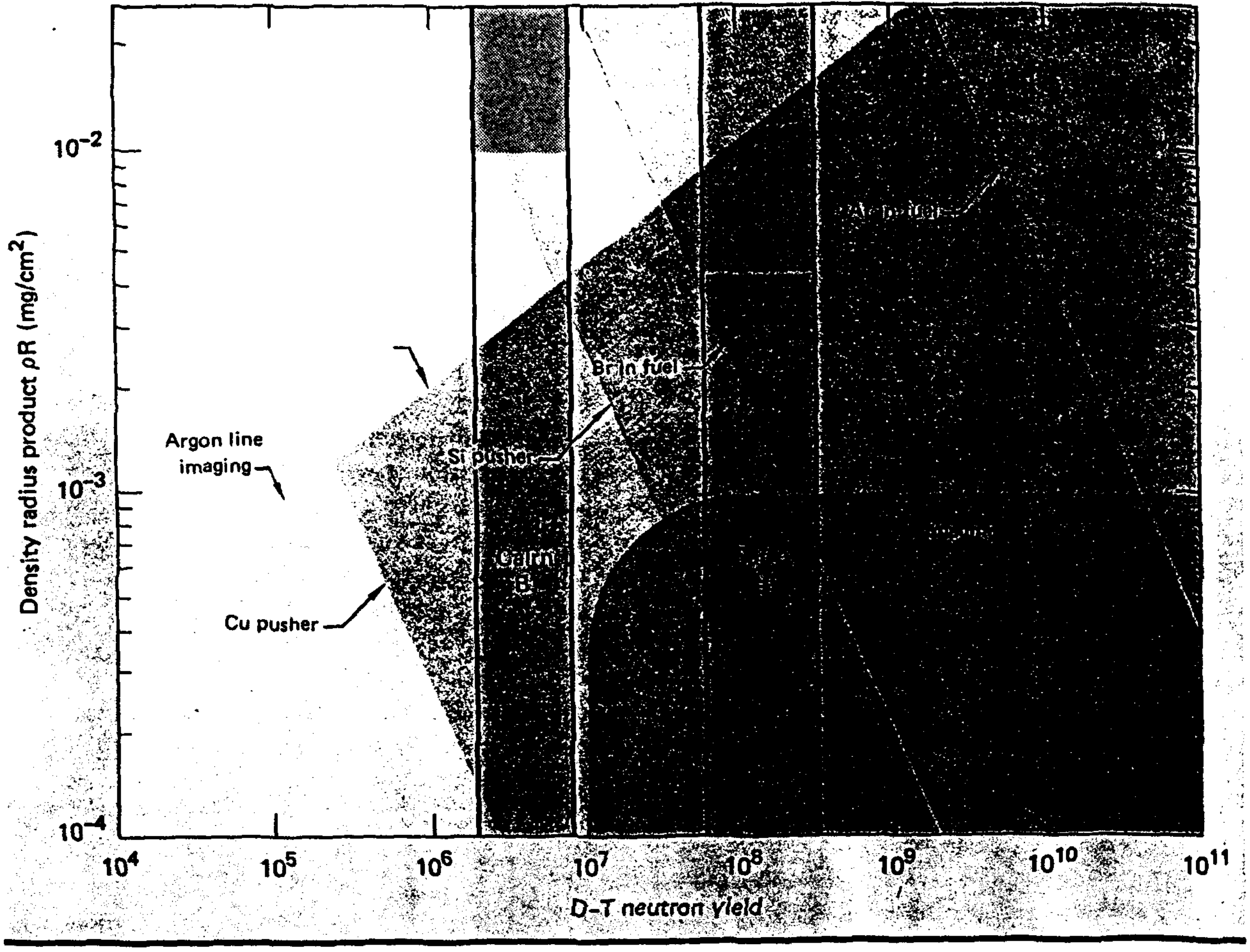

Titanium collector foils have been used in all of the radiochemistry experiments conducted at Shiva. We have observed, however, that ^{47}Ti is activated by target-produced protons having energies greater than 3.8 MeV. Since the activation product, ^{47}V ($t_{1/2}$ = 30 min), decays by β^+ emission—the same decay mode of activated copper and bromine, the ^{47}V decays will raise the background, making it difficult for us to count these materials we plan to use in future targets.

Generally, we conclude from these measurements that, using a cylindrical collector, the average fraction of sodium atoms collected for Cairn 2.0 H 140 × 5 + 15 CF targets is η_c = (20 ± 3)%. We assume that a similar fraction of the aluminum atoms, formed by neutron activation of the silicon atoms, is also collected.

Aluminum-28 decays by the emission of a β^- particle having a 2.86-MeV endpoint energy and a 1780-keV gamma ray. Figure 5-14(a) shows an aluminum-28 spectrum and the 280-keV-wide gamma-ray window; the γ background is about 85 cpm. The β-spectrum from an aluminum-28 sample is shown in Fig. 5-14(b). The upper limit of the window corresponds to the endpoint energy, and the lower limit was chosen at about 300 keV so that the beta-gamma coincidence background is approximately 0.3 cpm. Figure 5-14(b) also shows a background spectrum produced by betas in coincidence with a signal in the gamma window. The beta signal's background is about 35 cpm.

To measure the absolute efficiency of the beta-gamma coincidence detector, we placed a 1-cm² piece of 99.999% pure aluminum-27 next to a ^{252}Cf source that produced 8 × 10^8 n/s by spontaneous fission. The average neutron energy was 2 MeV. These neutrons were moderated by scattering in a 30.5 cm polyethylene sphere that surrounded the sample and source. The moderated

Fig. 5-14. Multichannel analyzer output for aluminum-28 (a) gamma and (b) beta spectra.

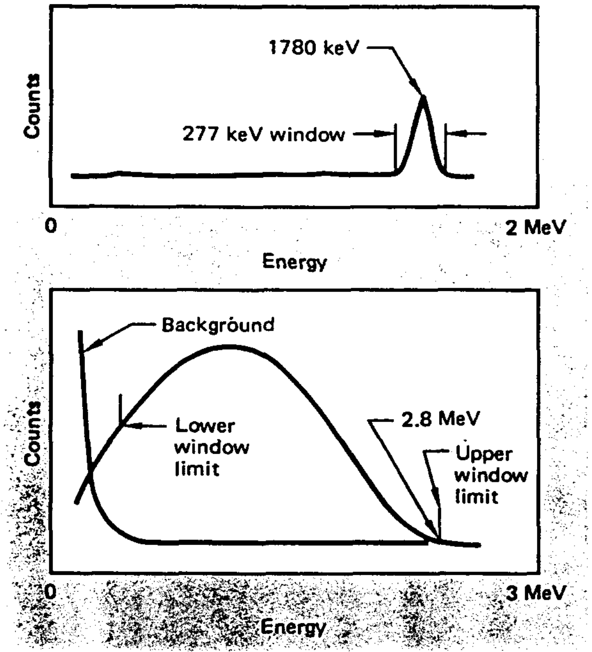

neutrons produced aluminum-28 ($t_{1/2}$ = 2.24 min) by neutron capture, proving that our calibration source was the same nuclide made in the pusher $\rho_p\Delta R$ experiments. Then we took about four minutes to transport the sample from the irradiation location to where we inserted it, along with a 2-mil-thick titanium collector foil, into our coincidence detector. The sample initially produced 2400 gamma cpm, 3900 beta cpm, and 1600 coincidence cpm.

We found the detector efficiencies (ϵ_γ and ϵ_β) by first recording the number of beta counts (n_β), gamma counts (n_γ), and coincidence counts ($n_{\beta\gamma}$) detected in 10 min and then solving the equations

$$n_\gamma = \epsilon_\gamma A,$$
$$n_\beta = \epsilon_\beta A,$$

and

$$n_{\beta\gamma} = \epsilon_\beta \epsilon_\gamma A,$$

where A is the source activity. The total efficiency of the system is the product of ϵ_γ and ϵ_β. Because the light transfer is excellent in the beta detector, its efficiency (measured as 69 ± 3%) is not dependent on source location. The efficiency of the gamma detector, on the other hand, is dependent on source location; system efficiency increases as the sample is placed deeper in the well.

We determined the efficiency of the gamma detector, via the above technique, to be 27 to 41% at source positions corresponding to the top and bottom, respectively, of the sample-containing region of the betafluor. In addition, we used the 1836-keV gamma ray of ^{88}Y, a convenient long-lived gamma-ray source to find the shape of the relative efficiency curve at intermediate positions. The overall efficiency for detecting ^{28}Al decays as a function of source position is given in Fig. 5-15. Then we determined a weighted average detector efficiency of η_D = (28 ± 2)% for Cairn targets. Because most of the debris is collected at the rear of the collector foil which, when placed in the NaI detector, corresponds to a location deep in the well where efficiency does not change rapidly with source location, the detection efficiency is very insensitive to the detailed debris distribution.

The aluminum-28 decay constant, λ, is known to be

$$\lambda = \frac{\ln 2}{t_{1/2}} = \frac{\ln 2}{2.24\ \text{min}} = 0.309\ \text{min}^{-1}$$

The loading time, t_L, is the time that elapses between the laser shot and the start of counting. About 17 s is needed to extract the collector-foil holder from the target chamber and transfer it to the counting area in the Shiva basement, where the collector foil is removed from the aluminum carrier and rolled to fit into a compatibly shaped beta detector. Then this detector is placed in the NaI well, the hatch to the shield is closed, and counting begins. Total loading time is typically 1.5 min. Although our total counting period, t_c, is variable since we collect data in a series of forty 30-s periods, we find that the signal-to-noise ratio is always near maximum when a counting time of 5 min is chosen.

N_c is the number of observed counts above background in the counting interval Δt, the coincidence background rate before and after a shot that was consistently 0.2 to 0.3 cpm. Figure 5-16 shows an example of the background. If we take the threshold of detection to be a signal that is three sigma above background in a five-minute counting

Fig. 5-15. Radiochemistry coincidence detector calibration.

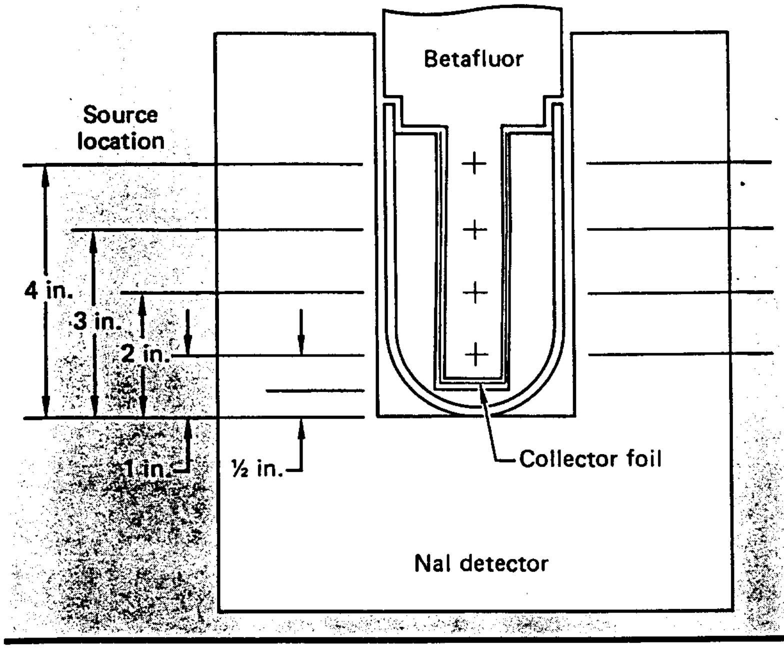

γ efficiency	β efficiency	Overall efficiency
0.33 ± 0.01	0.69 ± 0.03	0.23 ± 0.01
0.38 ± 0.01	0.69 ± 0.03	0.26 ± 0.01
0.40 ± 0.01	0.69 ± 0.03	0.28 ± 0.01
0.41 ± 0.01	0.69 ± 0.03	0.28 ± 0.01

Fig. 5-16. Typical coincidence signals before and after a Cairn target shot.

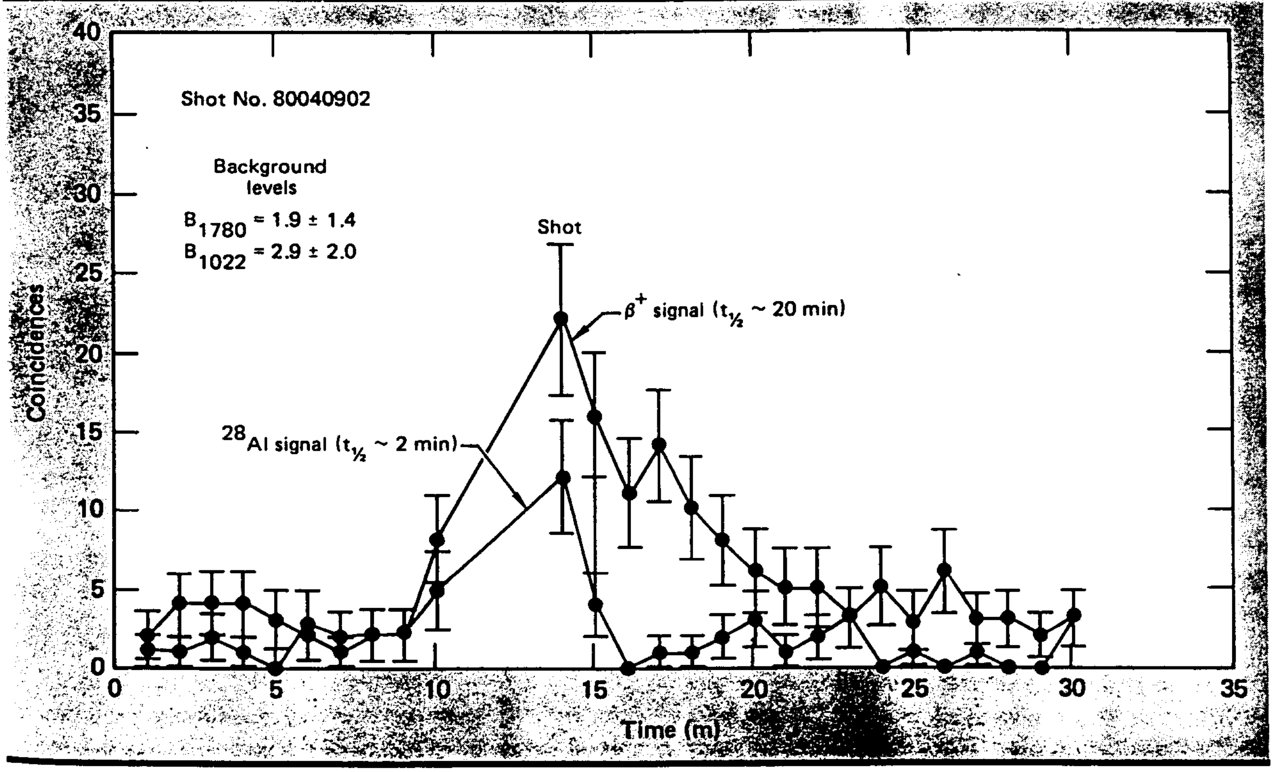

Fig. 5-17. Experimental measurements of the silicon-28 (n,p)/aluminum-28 cross section.

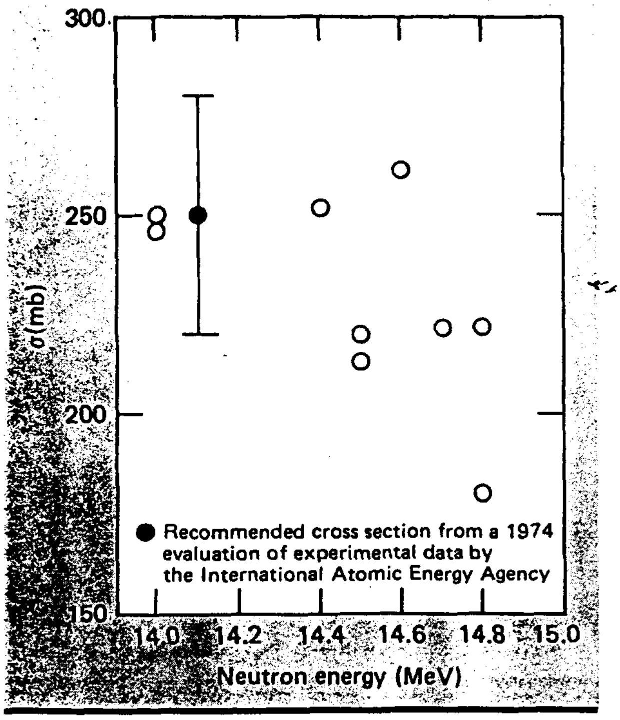

period, we must obtain at least four net counts [$3\sigma = 3\sqrt{(0.3\ \mathrm{cpm})(5\ \mathrm{min})} = 4$]. Using this number and typical values for the parameters in Eq. (1), we see that the radiochemistry system produces an above-background number of counts when Cairn targets create a total of 144 activated atoms.

From the number of activated atoms created in the target, N*, we calculate the $\rho_p\Delta R$ of the glass integrated over space and over the neutron production time by

$$\rho_p\Delta R = \frac{N^*}{Y_n\sigma f \frac{A_0}{A_{Si}} w} ,$$

The neutron yield, Y_n, is determined by lead and copper activation detectors. Figure 5-17 shows experimental measurements of the $^{28}Si(n,p)^{28}Al$ cross section, σ, at neutron energies of about 14 MeV. We take the cross section to be 250 ± 30 mb. The other parameters that enter the calculation are (1) the isotopic abundance of ^{28}Si, f; (2) the atomic weight of silicon, A_{Si}; (3) Avogadro's number, A_0; and (4) the mass fraction of silicon in the glass microspheres, w. We have used the values $f = 0.9223$, $A_{Si} = 28.0855$ g, and $w = 0.36 \pm 0.02$ (Ref. 5).

A summary of $\rho_p\Delta R$ measurements from the Cairn series is included in Table 5-1. When these data are plotted versus their corresponding neutron yields in Fig. 5-18, a clear trend emerges; that is, measured $\rho_p\Delta R$ values are larger for lower neutron yield and hence for lower ion temperature.

A simple ideal gas model based on an isothermal–isobaric approximation may be used to obtain a crude interpretation of radiochemistry results.[6] This isothermal–isobaric approximation relies on four assumptions:

1. A fraction, $\epsilon \cong 1.0$, of the SiO_2 pusher is assembled around the fuel in a spherical shell at the time of neutron emission.
2. All of the fuel is contained in the imploded pusher.
3. The pusher and fuel are both uniformly distributed.
4. The states of the pusher and fuel are characterized by one temperature (isothermal) and one pressure (isobaric).

Assumption four constrains the burn-time fuel density (ρ_f) to be related, via the equations of state for pusher and fuel, to the pusher density (ρ_p). Simulation calculations suggest that $\rho_p = \alpha\rho_f$, where $\alpha \cong 1.5$ to 2.0. Thus, the burn-time fuel density for any given target is related to the measured pusher $\rho_p\Delta R$ by

$$\rho_f = (\rho_p\Delta R)^{3/2}\, G\,(\epsilon M_p, M_f, \alpha) \quad ,$$

where

$$G\,(\epsilon M_p, M_f, \alpha) = \left\{\alpha\left(\frac{3}{4\pi}\right)^{1/3}\left[\left(\frac{\epsilon M_p}{\alpha} + M_f\right)^{1/3} - M_f^{1/3}\right]\right\}^{-3/2}$$

and M_p and M_f, respectively, are identically equal to the pusher mass and fuel mass in grams per cubic centimeter. By inserting typical values for the pusher and fuel masses, we find that

$$\rho_f \cong 2.3 \times 10^3 (\rho_p\Delta R)^{3/2}$$

This analysis places the fuel densities at burn time in the range of 1.0 to 10.0 g/cm³, given the observed $\rho_p\Delta R$ values, in agreement with the best LASNEX estimates listed in Table 5-1.

Fig. 5-18. Cairn pusher $\rho_p \Delta R$ measurements versus their neutron yields.

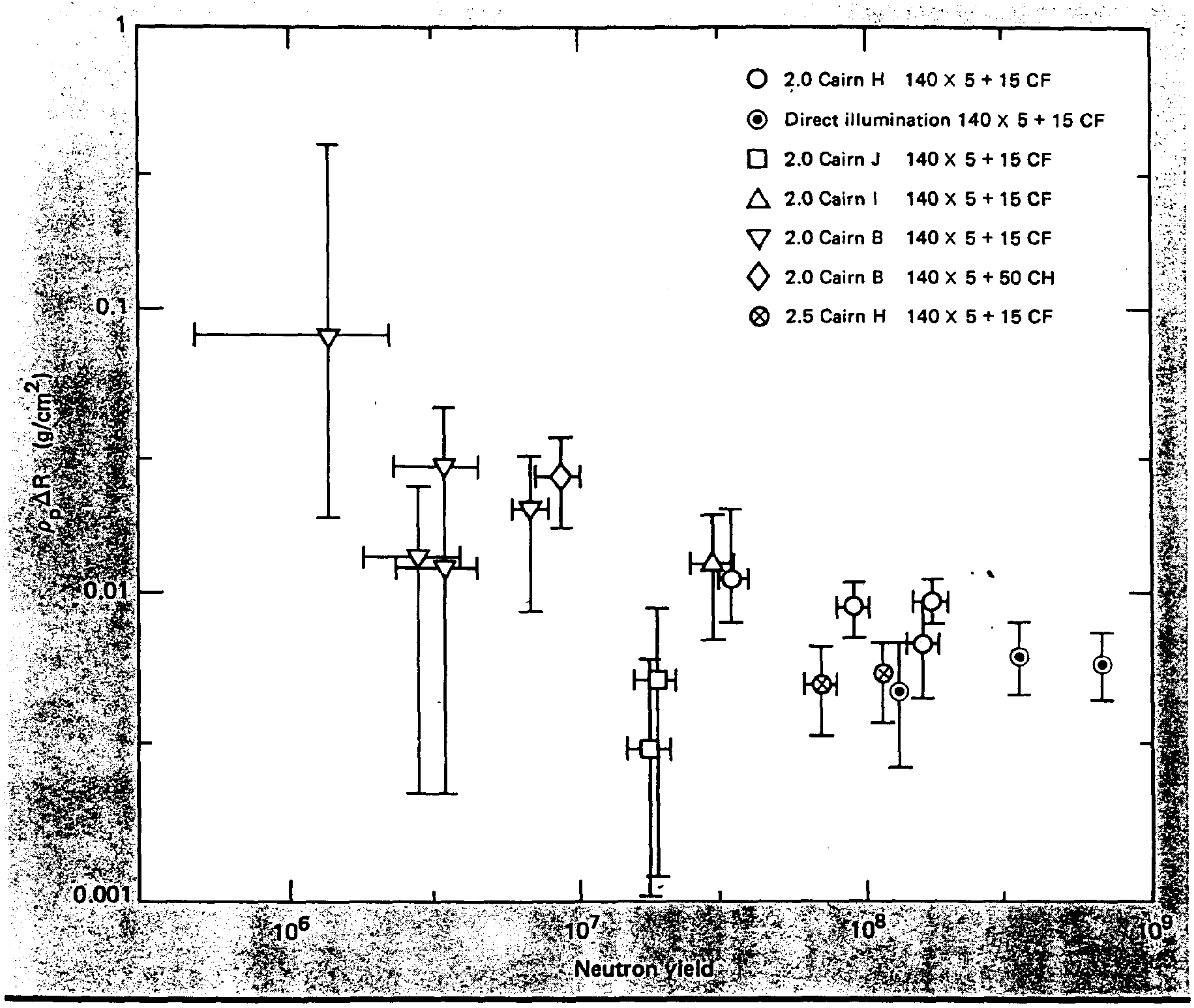

Imaging Crystal Spectrometer (ALICS and SILICS) Measurements on Cairn Targets. Three in a series of six shots fired with Shiva included argon line-imaging spectrometers (ALICS); the other three included silicon line-imaging spectrometers (SILICS). Of these, five were 2.0 Cairn Mod H shots and one was a 2.0 Cairn Mod B shot.

In all of these shots, either ALICS or SILICS was positioned on the (ϕ = 90°, θ = 108°) port directly opposite the x-ray microscope (XRM). ALICS/SILICS viewed the fuel ball through about a 200-μm-diam hole in the can; on the opposite side of the can was about a 330-μm-diam viewing hole for the XRM. The thickness of the glass pusher was varied somewhat for the 2.0 Mod H targets, but it was primarily the thickness of the $CF_{1.4}$ ablator that was increased during the shot sequence. On these shots, ALICS was to image, in one-dimension, (1) the size of the fuel core containing some argon by looking at the spatial extent of argon x-ray lines, (2) the diameter of the fuel–pusher interface by looking at potassium lines (K is a constituent of LLNL glass), or (3) the x-ray continuum stemming from the fuel, pusher, and ablator regions. SILICS had a similar purpose but its energy coverage was lower to facilitate observation of silicon, rather than argon and potassium lines. The results of these shots are outlined in Table 5-3.

From the shot synopses in Table 5-3 we can conclude that ALICS/SILICS gave an image only

Table 5-3. Synposes of imaging-crystal spectrometer (ALICS/SILICS) results for a series of six shots fired with Shiva. The targets included five 2.0 Cairn Mod H targets and one 2.0 Cairn Mod B target.

Shot No.	Comments
89031904	Target: 2.0 Cairn H Inside diameter: 145.4-μm; target material; $CF_{1,4}$, 3.3 mg/cm^3 D-T, 0.085 atm. argon; wall thickness: 2.5 μm glass; ablator thickness: 8.8 μm No argon line(s) observed, but ALICS imaged core x-ray continuum and some weak lines at ~2.5 and 3.5 keV. Core diameter determined to be ~27 μm. Heavy but tolerable overall fogging of x-ray film noted. XRM opposite ALICS indicated intense compressed emission zone in center of its ~330-μm-diam viewing hole. XRM channel No. 3, which is sharply peaked in efficiency at ~2.8 keV, correlates well with ALICS/SILICS data on this and subsequent shots. Its energy window closely approximates the energy range covered by ALICS or SILICS. See Fig. 5-19(a).
89031907	Target: 2.0 Cairn H Inside diameter: 136.0 μm; target material; 3.9 μm glass, 11.5 μm $CF_{1.4}$, 4,0 mg/cm^3 D-T, 0.14 atm. argon SILICS imaged nothing. Heavy but tolerable overall fogging of x-ray film noted. XRM observed a very weak compressed emission zone.
89032006	Target: 2.0 Cairn B Inside diameter: 138 μm; target material: 5 μm glass, 13 μm $CF_{1.4}$, 10.0 mg/cm^3 D-T, no argon. SILICS imaged nothing amid tolerable film fogging. XRM indicated no compression x-ray spike.
89032102	Target: 2.0 Cairn H Inside diameter: 144.6 μm; target material: 4.1 μm glass, 11.1 μm $CF_{1.4}$, 5 mg/cm^3 D-T, 0.16 atm. argon. Debris punctured Be window on SILICS film box, causing film to be overexposed by room lights. XRM indicated a weak implosion spike, although maximum emission zone is on extreme left side of viewing hole. See Fig. 5-19(b).
89032212	Target: 2.0 Cairn H Inside diameter: 143.6 μm; target material: 1.8 μm glass, 20.9 μm $CF_{1.4}$, 10 mg/cm^3 D-T, 0.09 atm. argon. Special target with minimum glass thickness to facilitate transport of Ar lines out of core. ALICS observed homogeneous overexposure of its film. XRM indicates weak implosion spike with ball on far left side of viewing hole.
89032305	Target: 2.0 Cairn H Inside diameter: 140.8 μm; target material: 1.7 μm glass, 20.9 μm $CF_{1.4}$, 10 mg/cm^3 D-T, 0.097 atm. argon. Another special ALICS target. ALICS observed no core image amid tolerable film fogging. XRM indicated weak implosion spike with maximum emission zone on far right side of viewing hole.

when the XRM indicated an intense implosion spike in the 2.8-keV channel. Further, since some of the compressed emission zones were misaligned relative to the ~330-μm-diam XRM viewing hole, ALICS/SILICS often could not have seen the imploded target. We do not understand the reason for this misalignment. Alignment checks and amplified spontaneous emission (ASE) tests produced no such displacements. Because of collimation by the diagnostic hole, ALICS only views a lateral expanse of 210 μm at the fuel-ball position.

We can speculate why the first target emitted so intensely at about 2.8 keV. Assume that silicon free-bound and free-free x-ray transitions are the most significant contributions to photon emission at about 2.8 keV. The first 2.0 Cairn H target was similar to all others except that it had the smallest ablator thickness. Thus, the weak intensity of photon emission observed by the XRM in subsequent shots could have been due either to significantly higher ablator opacity as a result of increasing the $CF_{1.4}$ thickness or to a decrease in the heating of the outer regions of the glass at maximum compression, again as the result of more $CF_{1.4}$ being present at that time. If the decrease in heating

Fig. 5-19. Side-viewing x-ray microscope images of Cairn H implosions. (a) On this shot, the XRM opposite ALICS indicated an intense emission zone in the center of its 330-μm-diam viewing hole. (b) On another shot, the XRM opposite SILICS indicated a weak implosion spike, although the maximum emission zone was on the extreme left side of the viewing hole.

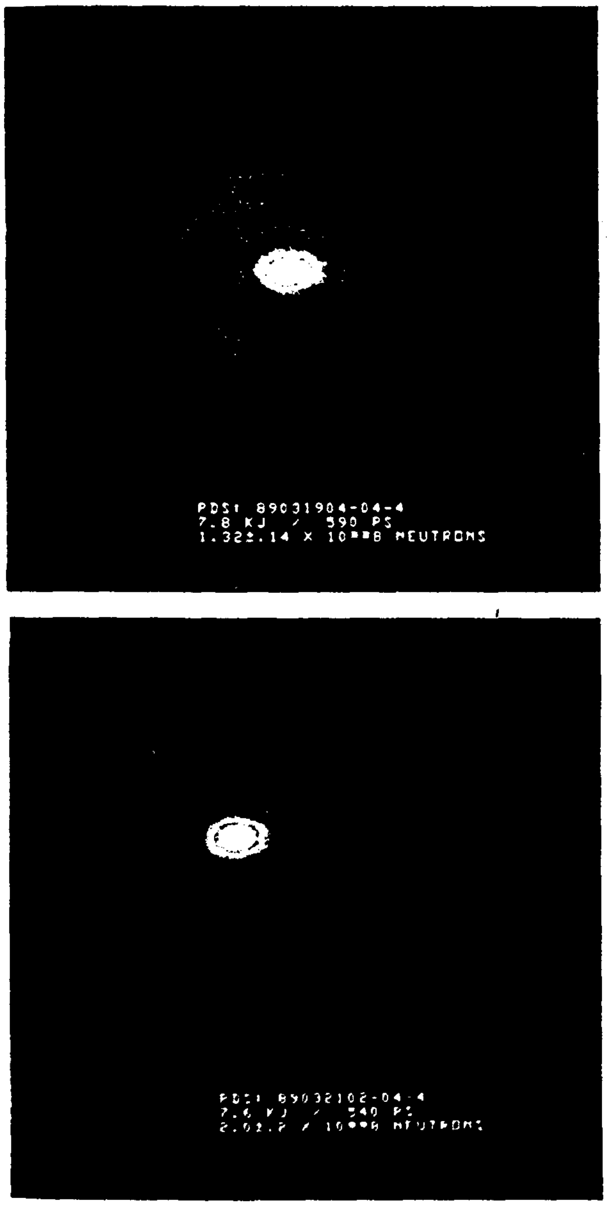

Fig. 5-20. Pinhole camera images produced by > 8-keV x-rays emitted by a Cairn B target.

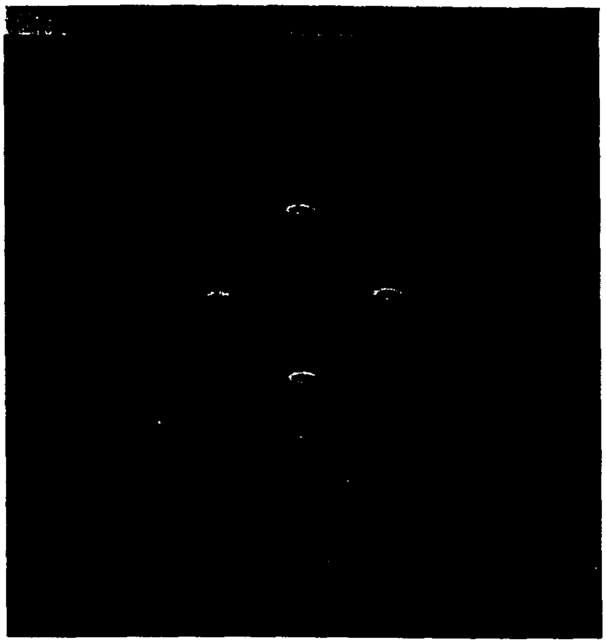

were the responsible mechanism at the time of maximum implosion, the outer regions of the pusher would be optically thick to silicon radiation emitted deep inside the glass, where electron temperatures and densities are the highest. This would imply that, on the first target, ALICS and the XRM were both viewing continuum radiation from deep inside the pusher. LASNEX predicts that electron temperatures for these H-series targets at maximum compression are about 700 eV at the fuel–pusher interface and about 280 eV at the pusher corona. Thus, it should have been possible to observe silicon continuum emissions at about 2.8 keV from a 5-μm-thick spherical shell near the fuel-pusher interface with an attenuation of only about a factor of 15 (assuming ρR glass $\cong 6 \times 10^{-3}$ g/cm^2). Potassium lines should also have been observable from this same shell at about 3.55 keV since they would suffer less absorption by the pusher. Unfortunately, our data indicate that only weak line emission was observed from the potassium. The observed silicon continuum emission, on the other hand, was more intense and possibly larger in spatial extent, suggesting that most of the photons we have recorded could have originated from a region that is both cooler than the interface and further out in the pusher shell. However, analysis of our data with regard to the volumetric compression measured refutes the above assertion. The base width of the spatial extent of continuum emission at 2.8 keV is measured to be about 27 μm. If we assume that the

Fig. 5-21. Multispectral zone-plate images of the compressed core of a Cairn H target.

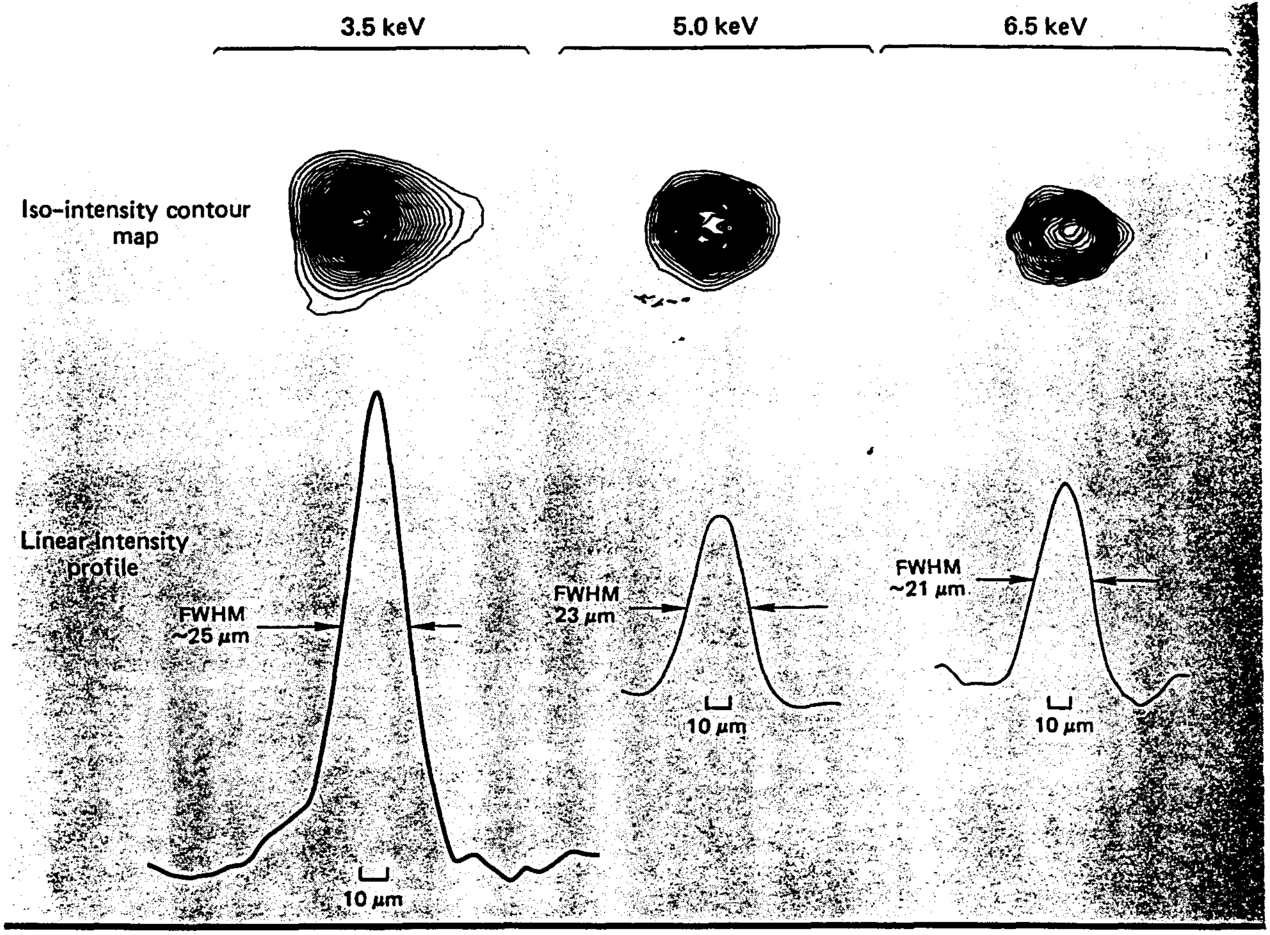

instrumental spatial resolution of 20 μm convolves in Gaussian quadrature with true source width, we obtain a core diameter of about 18 μm. Given the initial fill of 3.3 mg/cm^3 D-T, a core diameter of 17 μm would be necessary to attain 10 times liquid D-T density. Thus, to within our experimental uncertainty, we obtain density values that are consistent with the interpretation of radiochemistry measurements—i.e., at least 10 times compression for these series-H targets. Our measurements are, in fact, conservative since the spatial width of continuum emission at 2.8 keV is somewhat larger than that observed near the potassium lines at about 3.6 keV.

X-Ray Images. Besides x-ray microscope images such as those shown in Figs. 5-5 and 5-19, pinhole camera and Fresnel zone-plate camera images were recorded for some Cairn targets. Figure 5-20 shows a typical set of four images of a Cairn B target produced by x rays with energies exceeding 8 keV. Note that the laser scattering cones shine brightly through the ~20-μm-thick gold radiation case. Images of other Cairn designs are similar save for the presence or absence of scattering cones. In all images, the laser entrance holes and scattering cones—presumably high electrostatic field regions—show up clearly, independent of laser-beam focusing geometry; that is, this image of a Cairn B target was not detectably altered by irradiating the target with a Cairn H focusing geometry.

Figure 5-21 shows multispectral zone-plate images of the compressed core region of a Cairn H target. Like the ALICS and SILICS spectrometers, the camera was located at ($\phi = 90°$, $\theta = 108°$) and viewed the capsule through about a 200-μm-diam hole. In agreement with ALICS and radiochemistry observations, densitometry reveals a reasonably symmetric 21- to 25-μm-diam imploded core.

Modeling Cairn Implosions with LASNEX

It is not yet possible to model the Cairn implosions in full detail, both because the present codes are, at best, two-dimensional and because the experimental conditions (e.g., the spatial and temporal profile of each of Shiva's 20 beams on every shot) are not known fully. Indeed, even meaningful two-dimensional calculations are impractical at present because the laser deposition package in LASNEX does not contain all the necessary physics—Brillouin scattering at all angles, Raman and $2\omega_{pe}$ instabilities, etc.

We undertook a much less ambitious approach: to see if we could develop a one-dimensional model to simultaneously explain both the Cairn Mod B and H implosion results. We found such a set of model assumptions, several of which are only justified by arguments of self-consistency or by appeals to intuition. However, we don't claim that these simulations represent "the final" model, simply that they reproduce most of our experimental observations.

The main assumptions are that the Cairn H implosions are predominantly electron-driven and that the Cairn B implosions are preheated less than those in the Cairn H geometry.

Calculational Model, Cairn H Geometry. Our present one-dimensional model is an outgrowth of models developed in earlier work on Cairn implosions.[2] In this model, a laser-heated spherical radiation case creates a hohlraum at whose center the spherical capsule sits. The laser is introduced between the case and the capsule. The fraction of the laser light that goes outward and is absorbed in the case determines the radiation temperature and the production of those suprathermal electrons that dominate the production of hard x rays. The fraction of the laser light that goes inward and hits the capsule produces lower energy electrons that drive the capsule.

In the H model, seven-eighths of the absorbed laser light (i.e., 5.3 kJ) goes outward with a 600-ps FWHM Gaussian time profile. The inward pulse simulates the portion of the laser light that is refracted onto the capsule by blowoff from the hohlraum walls. This blowoff-caused refraction comes on sharply about 200 ps into the laser pulse, according to two-dimensional LASNEX calculations. For this reason, the inward laser pulse (0.7 kJ) is given a 200-ps FWHM Gaussian profile in time. Although this amount of laser light exceeds the amount expected to hit the capsule if the laser light were diffusely scattered off the hohlraum walls, the yields observed in the Cairn H implosions require this large a fraction. This ansatz is supported by the two-dimensional calculations of this geometry that show laser light being focused onto the capsule by the blowoff-caused refraction.

The outer hohlraum wall is treated using the non-local thermodynamic equilibrium (NLTE) capability in LASNEX, in accordance with the disk modeling discussed in "Theoretical Modeling" in Sec. 2. As in disk modeling, emission opacity is set to 0.5 to get temperatures (180 to 185 eV) that are close to those seen in the experiments (180 ± 20 eV).

The laser light is absorbed either by inverse bremsstrahlung in the underdense region of the plasma or by instabilities at critical density. The fraction of light absorbed by each mechanism is controlled, as is the suprathermal temperature, to give electron drive early in time (before the laser peak) and to produce hard x rays late in time (after the laser peak).

The justification for assuming that the Cairn H implosions are predominantly electron-driven lies in the proximity of the Cairn H implosion results to those obtained using direct laser illumination of the same capsule (compare hexagons and circles in Fig. 5-18).[7] The direct-illumination implosions are certainly electron-driven, and their proximity to Cairn H implosion results suggests that the Cairn H implosions may be similarly driven.

In these one-dimensional calculations, the spherical hohlraum fills to quarter-critical density at the peak of the laser pulse. The current picture of hohlraum processes suggests that Raman and $2\omega_{pe}$ instabilities will become strong at this time and produce a much hotter flux of suprathermals. The suprathermal temperature is, therefore, increased at the peak of the laser pulse to simulate the onset of these instabilities (Fig. 5-22). At the same time, the inverse bremsstrahlung absorption is reduced so that all remaining laser light goes into the instabilities and produces suprathermals (Fig. 5-23).

Fig. 5-22. Temperature of suprathermal electrons generated by LASNEX during a Cairn Mod H calculation. The jump discontinuities at 0.11 and 0.13 shake (one shake equals 10^{-8} s) are input changes. The jump discontinuity at 0.14 shake is due to plasma filling the channel between the capsule and the hohlraum wall.

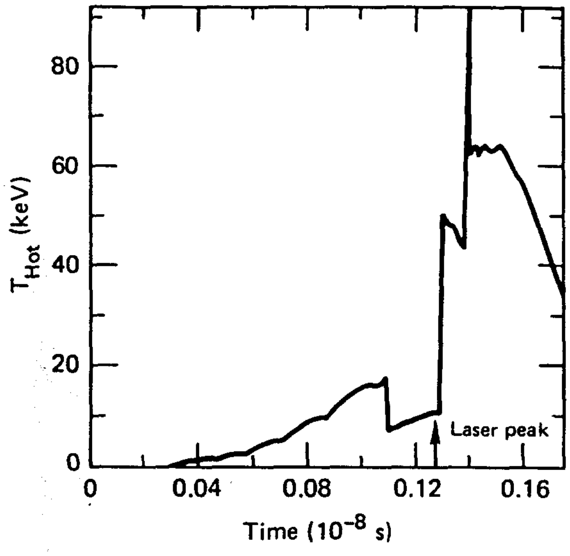

Fig. 5-23. Energy split between inverse bremsstrahlung and suprathermal deposition in the LASNEX calculation of a Cairn Mod H implosion. At the end of the calculation, 71% of the absorbed energy has gone into suprathermals.

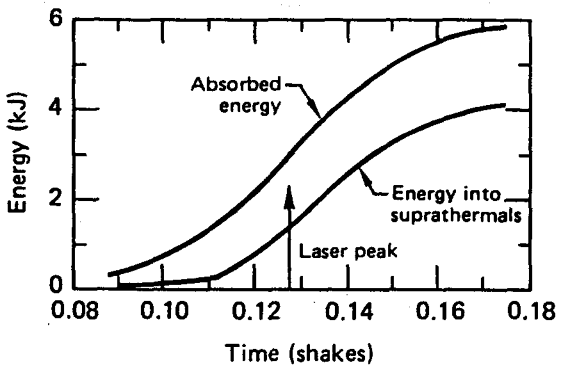

Calculational Model, Cairn B Geometry. The Cairn B geometry has shields and a parylene can (Fig. 5-1), which the Cairn H geometry lacks, and the laser focusing is, in general, different in the two geometries. The extent to which these differences change the physical environment in which the capsule resides (i.e., the x-ray and electron spectral fluxes as functions of time) are not, as yet, experimentally known in detail.

In the Cairn B geometry, blowoff from the parylene can and from the wall outside this can will tend to exclude laser light from the midsection of the hohlraum. This should be especially true after the laser peak, when the bulk of the suprathermal electrons are generated. Thus, the x rays and suprathermal electrons will be generated in the ends of the hohlraum and will have to scatter around the shields to get to the capsule. This will tend to depress both the x-ray and electron fluxes at the capsule location relative to those seen in the Cairn H geometry. The x-ray albedo is higher than the electron albedo, so the x-ray flux at the capsule should be depressed less. A simple area scaling of radiative fluxes suggests that the radiation temperature at the capsule should be ≈10 eV less in the Cairn B geometry, whereas the same kind of argument for the electrons suggests a factor of 3 to 5 reduction in flux.

We implemented these corrections by taking the radiation temperatures determined in the Cairn H geometry calculation, decreasing them by 10 eV, and forcing this temperature in the Cairn B geometry calculation. The electron flux was reduced by introducing "leaks" into the LASNEX calculation, which removed part of the electron flux before it reached the capsule. The best agreement with experiment was obtained when only 25% of the original electron flux reached the capsule.

We introduced the parylene can into the calculation as a spherical shell between the case and capsule. Although the shields were not physically put in the calculation, their effect on the x-ray and electron fluxes was. All the laser light was initially directed outward toward the radiation case.

Calculational Modeling of Two-Dimensional Asymmetrics. The Cairn geometries are suspected of having some temperature asymmetries around the capsule. At present, the experimental evidence for this is far from complete. A crude method of including this effect in one-dimensional calculations is to "dud" the center of the D-T fuel so that it doesn't burn. This models an asymmetric shock wave that would produce lower central temperatures. The amount of fuel dudded is a measure of asymmetry; however, since these implosions tend to produce a temperature distribution peaked in the center of the fuel, any dudding has a significant effect on yield.

Fig. 5-24. Comparison of Cairn Mod H and B calculations with experimental results. The numbers above each calculational point refer to the fraction of fuel mass that is dudded (i.e., not allowed to burn) at the center of the capsule.

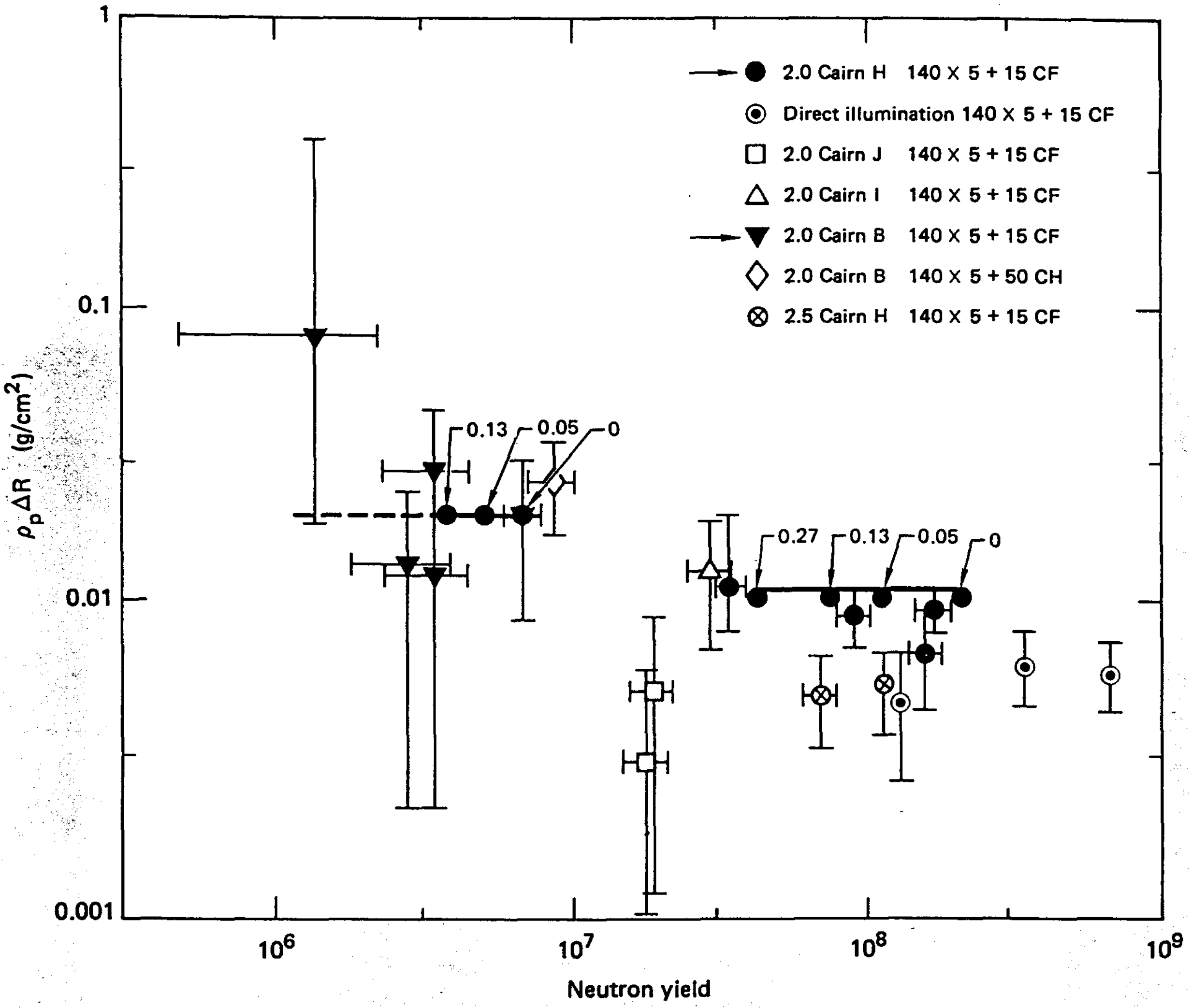

Calculational Results. Both models give neutron yields and pusher $\rho\Delta R$'s that are close to the experimental observations (Fig. 5-24). The experimental data seem consistent with the lines of calculational results with increasing central fuel dudding, suggesting that the experimental data spread is caused by different drive asymmetries on different experiments.

These models suggest peak fuel densities of 4.0 g/cm^3 for the Cairn H implosions and 5.5 g/cm^3 for the Cairn B implosions (Table 5-4).

The calculations systematically give lower hard x-ray fluxes than those observed experimentally. The model presented in Fig. 5-24 gives a flux at 50 keV of 5.8 × 10^{14} keV/keV (compare with Table 5-1) for a normalized flux of 1.5 × 10^{-5}(keV)$^{-1}$ (compare with Fig. 5-8). This is at the lower end of the values actually observed, although 71% of the absorbed laser light went into suprathermals in the LASNEX calculation (with an average T_{Hot} = 30 to 40 keV).

Both models (Cairn H and B) are sensitive to the number of suprathermals that cause preheat early in the implosion. In the Cairn H model (Fig. 5-25), the relative number of drive to preheat electrons (roughly those below and above 20 keV, respectively) is important. Decreasing the drive gives a constant flux of preheat electrons more time

Table 5-4. LASNEX simulations of Cairn B and H targets.

Target model	Neutron yield	Pusher[a] $\rho\Delta R$, g/cm^2	Fuel[a] ρR, g/cm^2	Peak fuel density, g/cm^3	Density at peak burn, g/cm^3
H	1.9×10^8	0.0097	0.0023	4.04 (19×)	2.3
B	7.4×10^6	0.0190	0.0032	5.45 (26×)	4.3

[a] Neutron-production-weighted time-averaged quantities.

Fig. 5-25. Dependence of calculated performance on changes in suprathermal flux. The change in Mod H calculations, although predominantly a reduction in electron drive (about a factor of three), included a concomittant increase in preheat. Numbers above the Mod B calculational results give the relative amount of suprathermal preheat.

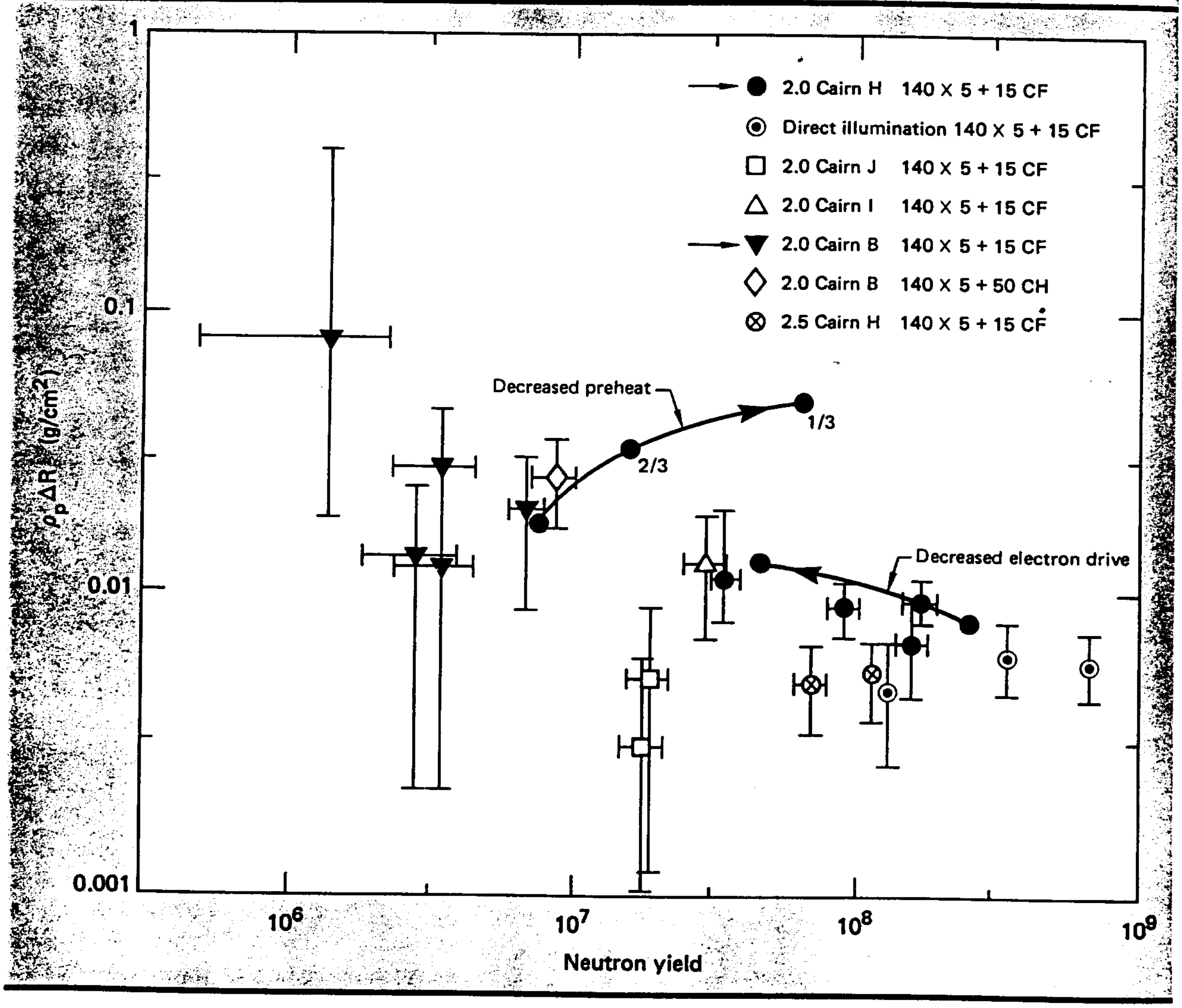

Fig. 5-26. **(a) Variation in calculated performance of Cairn Mod B implosions with changes in the assumed radiation temporal profile. Temperature profile curves in (b) are referenced by letters near each calculated result. (b) Three temperature profiles prescribed in a Cairn Mod B implosion calculation with the results shown in (a). The nominal Cairn H calculation gives curve A. Curve C was used in the nominal Cairn Mod B calculation. Curve B shows the effect of a broader, flatter profile. The difference in peak temperature between curves A and C is less than the experimental error.**

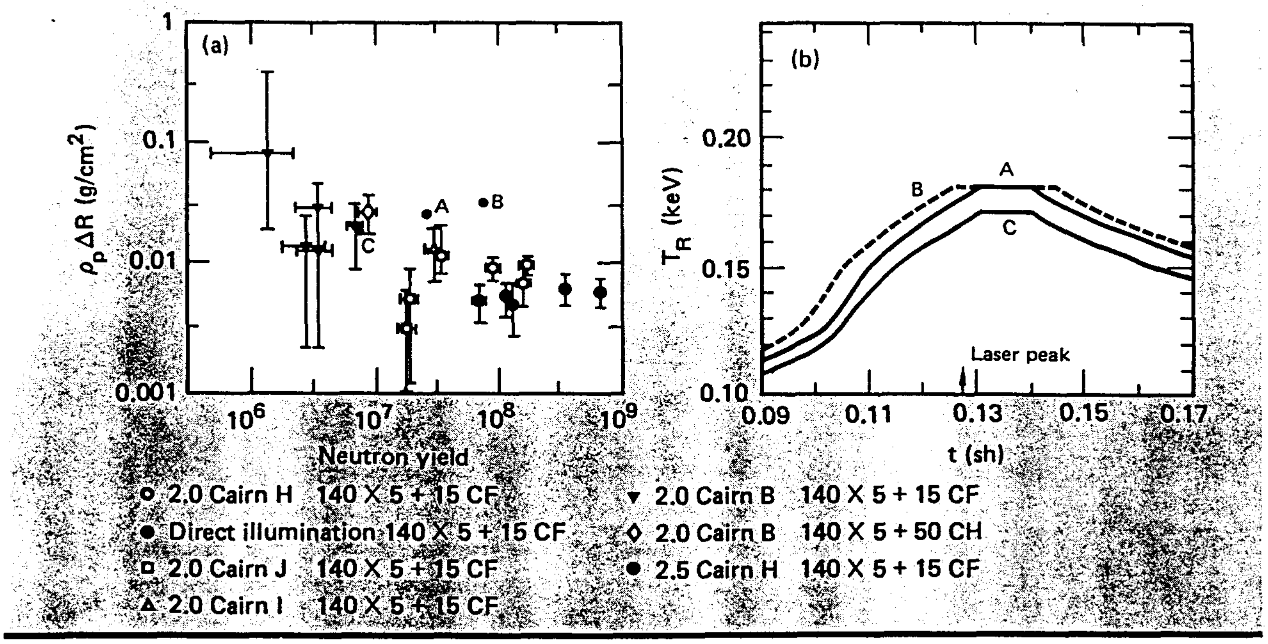

to act, which is roughly equivalent to increasing the preheat at constant drive. The Cairn B implosions, on the other hand, are radiation-driven, so decreasing the suprathermals affects only the preheat. Less preheat means improved performance (Fig. 5-25).

We used the LASNEX-derived radiation-temperature-vs-time profile for the calculations. Experimental data on the time-dependence of the radiation temperature are very sparse. While the peak temperatures in these calculations (180 to 185 eV) are roughly consistent with the peak observed temperatures (168 to 177 eV with ±15-eV error bars); the actual profile seen by the capsule can substantially influence the calculational results, as can variations within the experimental error bars (Fig. 5-26).

Extension of Modeling to Other Capsules and Geometries. The agreement between the model of the Cairn H implosion and the experimental results was, to some extent, foreordained since the model was varied until agreement was reached. The agreement between the Cairn B model and the experimental results is less suspect in this regard because the Cairn B model was largely determined by the Cairn H model.

Two good checks of the whole procedure are (1) to calculate new capsules in the same geometry and (2) to calculate the same capsule in other, related geometries. The 140 × 5 + 50 CH capsule, which was imploded in both the Cairn H and B geometries, provides the first kind of check. The Cairn I and J geometries (Fig. 5-6), which are intermediate between the Cairn H and B geometries, provide the second kind of check.

The calculation of the 140 × 5 + 50 CH capsule gave yields about a factor of four higher than those observed (Fig. 5-27), suggesting that the implosions for this capsule were either substantially more asymmetric than those for the 140 × 5 + 15 CF capsule or that the model is not universal. The 140 × 5 + 50 CH capsule is considerably larger than the 140 × 5 + 15 CF capsule; it is also large with respect to the shields and parylene can (Fig. 5-28). Thus, one might expect a more severely perturbed implosion with this larger capsule.

Fig. 5-27. Comparison of calculations of Cairn Mod I, Mod J, and a 140 × 5 + 50 CH capsule in Mod B geometry, with experimental results. The upper Mod I calculation had no inward-directed laser pulse. The lower Mod I calculation had the same inward-directed laser pulse used in the Mod H calculation.

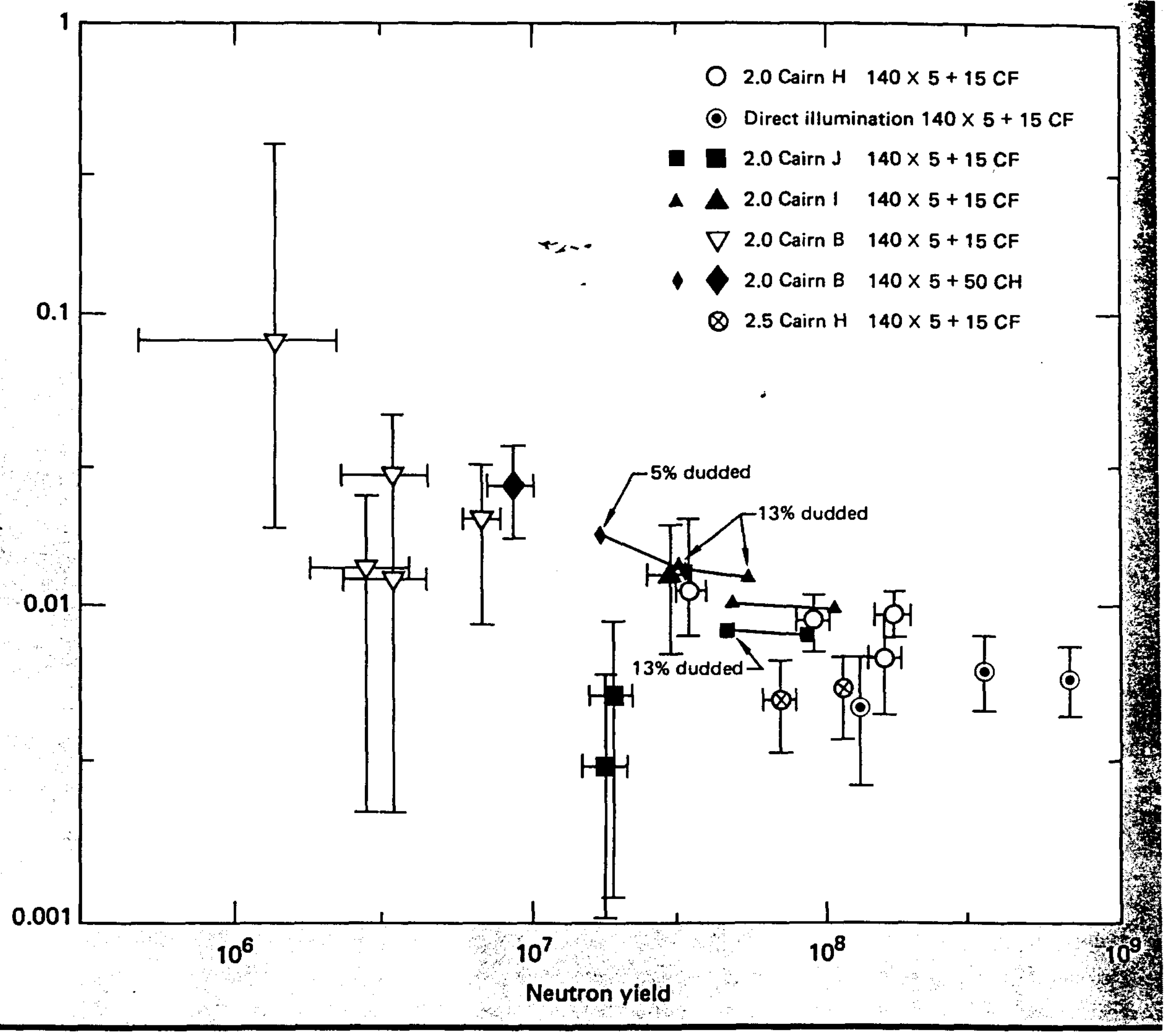

The one experimental measurement of the Cairn I implosion is in good agreement with the calculations. This geometry was modeled by including the parylene shell in a Cairn H calculation, with all of the laser energy directed outward to simulate the exclusion of laser light from the region between the parylene can and the hohlraum wall. If this assumption is introduced into a Cairn H calculation with no change in laser deposition, the calculated yield will be a factor of two too high (Fig. 5-27).

The calculation of the Cairn J implosion differs considerably from the experimental results (Fig. 5-27), being a factor of three too high in yield and a factor of two too high in $\rho\Delta R$. This geometry was modeled by removing the parylene shell and introducing an inward-directed laser into the Cairn B calculation. The experimental data for the two Cairn J implosions was of poor quality. The $\rho\Delta R$ values were particularly low, being only a factor of four above the initial $\rho\Delta R$ prior to implosion, and it is not clear that the data are reliable enough to constitute a good check of the calculational model.

Overall, this modeling approach predicts densities of 3 to 6 g/cm^3 for these implosions (Table 5-5). It does fairly well at predicting $\rho\Delta R$'s (using

Table 5-5. Extension of LASNEX model for Cairn B and H targets to other geometries.

Target model	Neutron yield	Pusher^a $\rho\Delta R$, g/cm^2	Fuel^a ρR, g/cm^2	Peak fuel density, g/cm^3	Density at peak burn, g/cm^3
I	5.8×10^7	0.0130	0.0028	4.4 (19×)	3.1
J	8.6×10^7	0.0078	0.0018	3.6 (17×)	1.8
140 × 5 + 50 CH in B model	3.3×10^7	0.0136	0.0029	6.2 (30×)	4.5

Fig. 5-28. Comparison of a 140 × 5 + 15 CF capsule and a 140 × 5 + 50 CH capsule in a Cairn Mod B geometry. The CH capsule's larger diameter may result in larger temperature asymmetries.

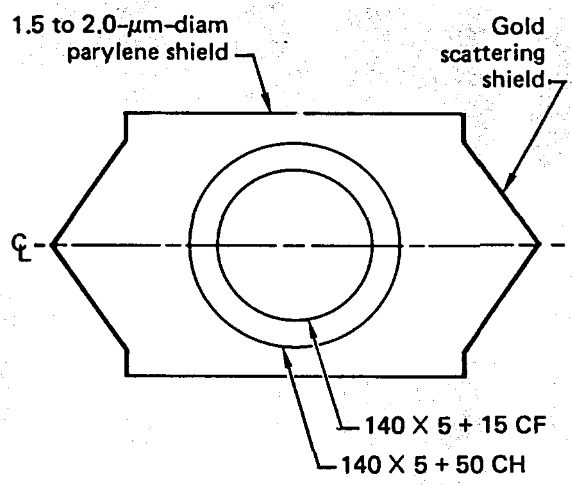

slightly dudded calculations) and gets the yields within a factor of four.

Summary

Figure 5-29 provides a look at the data accumulated by various techniques for all target studies performed at Shiva during 1978-1979. Such model uncertainties as pusher–fuel mixing near burn time may introduce a factor-of-two systematic interpretation error. The data plotted are a best estimate of D-T fuel density at burn time.

Figure 5-29 reveals that the targets of each design irradiated by the Shiva facility cluster in density-vs-neutron-yield space. Low-density "Hyperion" exploding-pusher targets achieved ion temperatures in the range of two to four keV and, therefore, yield near 10^{10}. Bare Teflon-coated microspheres and Cairn H targets reached D-T densities of about two to four grams per cubic centimeter and ion temperatures of just over one kiloelectron volt so that about 10^8 D-T neutrons were produced. Finally, Cairn B targets achieved densities of 6 to 10 g/cm^3 at ion temperatures of about 500 eV. The several Cairn designs are well separated in this plot. Table 5-6 summarizes their average performances.

The same data are replotted in Fig. 5-30 to display the variation of fuel ρr with ion temperature. Here higher fuel areal density has been achieved at the expense of ion temperature and D-T burn efficiency (defined as the fraction of D-T fuel consumed during the burn). Target designs tested during 1979 challenged our measurement capabilities. Operating regimes often maximized both x-ray drive and preheat, causing severe interpretation difficulties. Neutron yields for the Cairn B design were marginal for reliable pusher $\rho_p\Delta R$ measurements; however, all the data indicate that Cairn B achieved 30 to 50 times liquid D-T density.

Authors: K. R. Manes and J. C. Stevens

Major Contributors: J. M. Auerbach, E. M. Campbell, N. M. Ceglio, S. M. Lane, R. A. Lerche, L. N. Koppel, D. L. Matthews, R. H. Price, and W. M. Ploeger

Fig. 5-29. Fuel density at burn time versus neutron yield.

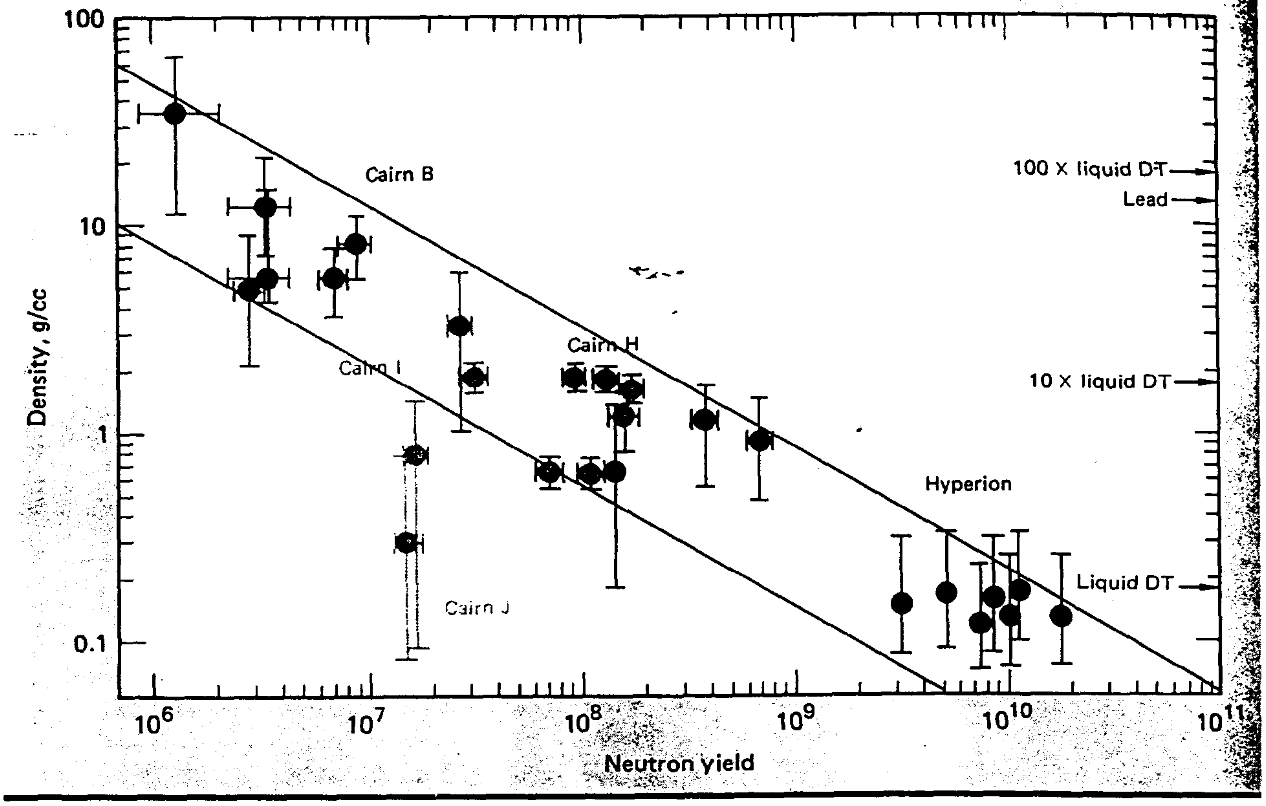

Table 5-6. Results for average 2.0-scale Cairn targets.

Target model	Neutron yield	Pusher R, g/cm^2	Peak fuel density
B	$(4.9 \pm 2.7) \times 10^6$	$0.022 \pm {}^{0.011}_{0.006}$	40×
H	$(1.1 \pm 0.1) \times 10^8$	$0.0089 \pm {}^{0.0012}_{0.0021}$	17×
I	$(3.1 \pm 0.5) \times 10^7$	$0.013 + 0.006$	21×
J	$(1.8 \pm 0.2) \times 10^7$	0.004 ± 0.002	3×
K	$(1.4 \pm 0.4) \times 10^6$	—	—

Fig. 5-30. Fuel conditions achieved, 1978–1979.

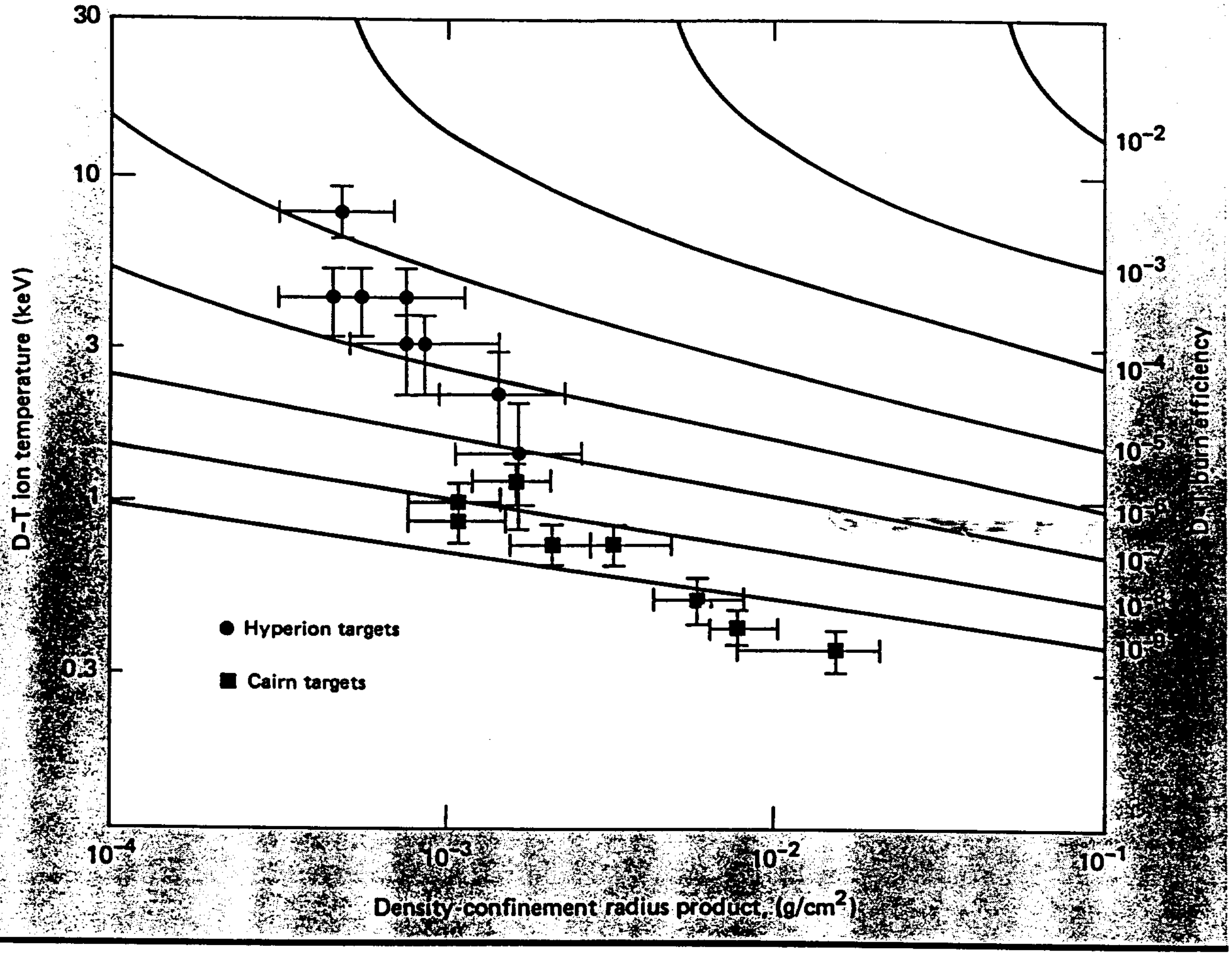

Cairn Scaling Study—the Experiments

Introduction

Since October 1979, we have been engaged in a series of experiments to characterize the physics of empty Cairn hohlraums. The series was motivated by two needs: (1) to provide data to normalize the hydrodynamics codes modeling hohlraum phenomena and (2) to provide scaling data applicable to the design of Nova targets. The experiments have been performed on the Shiva laser facility as part of our study of drive and preheat in radiation-driven targets.

Background

Our main approach to producing high-density compression of D-T fuel is through radiation-driven implosions. The inertial-confinement fusion (ICF) target for these implosions consists of a fuel-filled microsphere enclosed in a cylindrical gold hohlraum, at each end of which is a laser entrance hole. Laser energy is directed into both ends of the cylinder, heating the gold and causing it to emit thermal x rays ($T_R \approx 100$ to 200 eV) that act as the drive for the capsule implosion. This radiation drive is calculated to be almost isotropic and uniform enough to avoid exacerbating fluid instabilities.

Attainment of the hohlraum temperatures required for implosion has, unfortunately, been accompanied by a great increase in "hot" electron preheat. The enclosed geometry of our target has resulted in STE production rates far exceeding that observed when the same amount of laser energy is used to irradiate a disk target (discussed in the preceding article). STE production rates depend on a number of processes. At present, the following are thought to be the principal phenomena:

- *STE production by resonance absorption.* Laser beams irradiate the inner surface of the hohlraum, and suprathermal electrons are created at the critical density layer.[27] Refraction of the laser beams by underdense plasma filling the hohlraum may lead to higher intensities on the surface than might be the case in an empty cylinder. The result is enhanced resonance absorption and high STE production.
- *Laser-beam filamentation.* This process also depends on an underdense plasma filling the hohlraum. A local increase in laser intensity results in a local reduction in plasma density.[28] The local index of refraction is thereby changed in such as way as to further increase laser intensity. This process can result in very energetic electrons and in intensities as high as 10^{17} W/cm^2.
- *Damping of plasma waves from plasma instabilities.* Stimulated Raman scattering[29] (light wave converts into an electron plasma wave and light wave at lower frequency) and two-plasmon decay[30] (light wave converts into two electron plasma waves) give rise to high-phase-velocity electron plasma waves. Landau damping of these waves results in the production of very-high-energy electrons. These processes occur at plasma densities of $1/4\ N_{cr}$ or less, making them likely candidates in the plasma filling a hohlraum. Strong emission of Raman-scattered light has been observed from hohlraums irradiated at both the Shiva and Argus laser facilities.

The relative contribution of each of the above processes in any hohlraum experiment is critically dependent on the plasma density distribution. If this distribution were known precisely, the prediction of STE production could be accurate. Unfortunately, measurement of the microscopic plasma structure in the hohlraum is difficult and has not yet been carried out. However, we have designed experiments to examine the macroscopic characteristics of suprathermal electrons in hohlraums and to compare them to the macroscopic predictions of theory. In addition, we intend to use the scaling results of these experiments to infer the preheat level of targets proposed for Shiva and Nova.

The input quantities for the experiments discussed here are the geometry and material of the hohlraum and the characteristics of the laser pulse (energy, duration), while the primary output quantities to be measured are related to the suprathermal electrons. However, we have also completed a study relating laser light absorption and thermal x-ray drive to the above input parameters. Since most suprathermal electrons do not leave the hohlraum, their characteristics cannot be measured directly; therefore, we have elected to measure the characteristics of the Bremsstrahlung x rays produced by these electrons. These x rays are produced primarily by collisions of the electrons with ions in the walls of the hohlraum. X rays having photon energies greater than or equal to 50 keV pass through the 20-μm-thick gold hohlraum walls without much attenuation. Diagnostics are implemented to record the spatial, spectral, and temporal characteristics of these x rays.

We can also look for the signature of nonlinear plasma processes such as Raman scattering. Infrared detectors to check for scattered light about the Raman wavelength ($\lambda = 2.12\ \mu$m) can be easily set up (see "Experimental Details").

Fig. 5-71. Hohlraum characteristics of Cairn targets irradiated by the Shiva laser system.

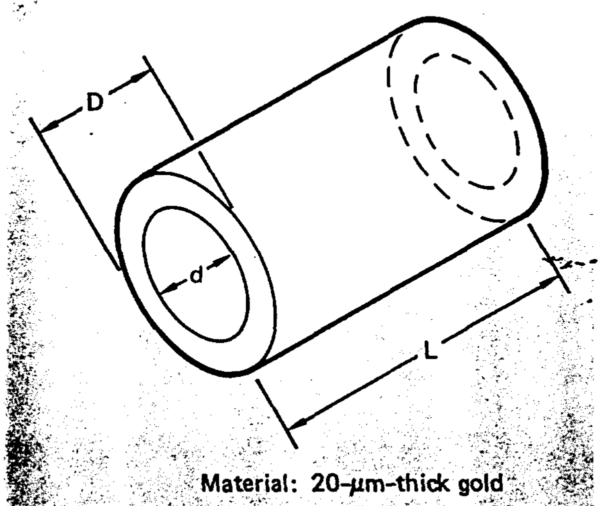

Scale No.	D, µm	L, µm	d, µm
1.6	800	1280	400
2.0	1000	1600	500
2.5	1250	2000	625
3.0	1500	2400	750
4.0	2000	3200	1000
5.0	2500	4000	1250
5/8-3.0	1500	1500	750
5/8-4.0	2000	2000	1000

Fig. 5-72. Temporal shape of a typical incident laser pulse at the output of the amplifier chain for the 2-ns experiments. The 2-ns pulse was formed by stacking two 1-ns pulses at the output of the Shiva oscillator.

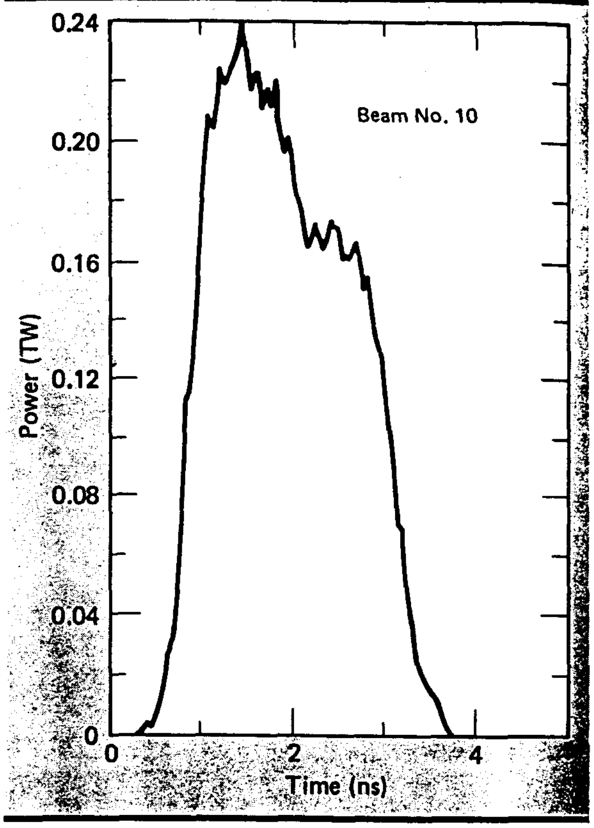

Experimental Details

Figure 5-71 summarizes the characteristics of the hohlraums used in the experiments. Most were standard Cairn hohlraums, which have a length/diameter ratio of 1.6 and a laser-entrance-hole/hohlraum-diameter ratio of 0.5. As shown in Fig. 5-71, hohlraums with scale factors of two to five were used. The basic Cairn hohlraum (1.0 factor) is 800 µm in length and 500 µm in diameter, with a 250-µm-diam laser-entrance hole. The hohlraums are fabricated from 20-µm-thick gold. On the cylindrical surface of each hohlraum is a 300- to 400-µm-diam diagnostic hole to measure the thermal x-ray spectrum within. To investigate the effects of aspect ratio (length/diameter), we used the 5/8-to-3.0- and 5/8-to-4.0-scale hohlraums. The motivation for using a unity-aspect-ratio hohlraum will be described later in the paragraphs on target alignment.

The Shiva laser system was used to irradiate these Cairn hohlraums. There were two sets of experiments at different pulse lengths. The first set utilized a 2-ns pulse, formed by stacking two 1-ns pulses at the output of the Shiva oscillator, and energies of 0.5 to 6 kJ. Figure 5-72 illustrates the temporal shape of a typical pulse at the output of the amplifier chain. For the second set of experiments, a simple Gaussian pulse with a FWHM of 600 ps was employed. Incident and reflected-beam calorimeters measured the light reaching the target for each beam and the light scattered back through each target irradiation lens.

An extensive set of diagnostics was positioned on the Shiva target chamber for both sets of experiments. Arrays of scattered-light photodiodes and calorimeters were located at various positions on the chamber to record the scattered 1.06-µm light

Fig. 5-73. Diagram of a typical Raman detector unit used for single-detector Raman experiments.

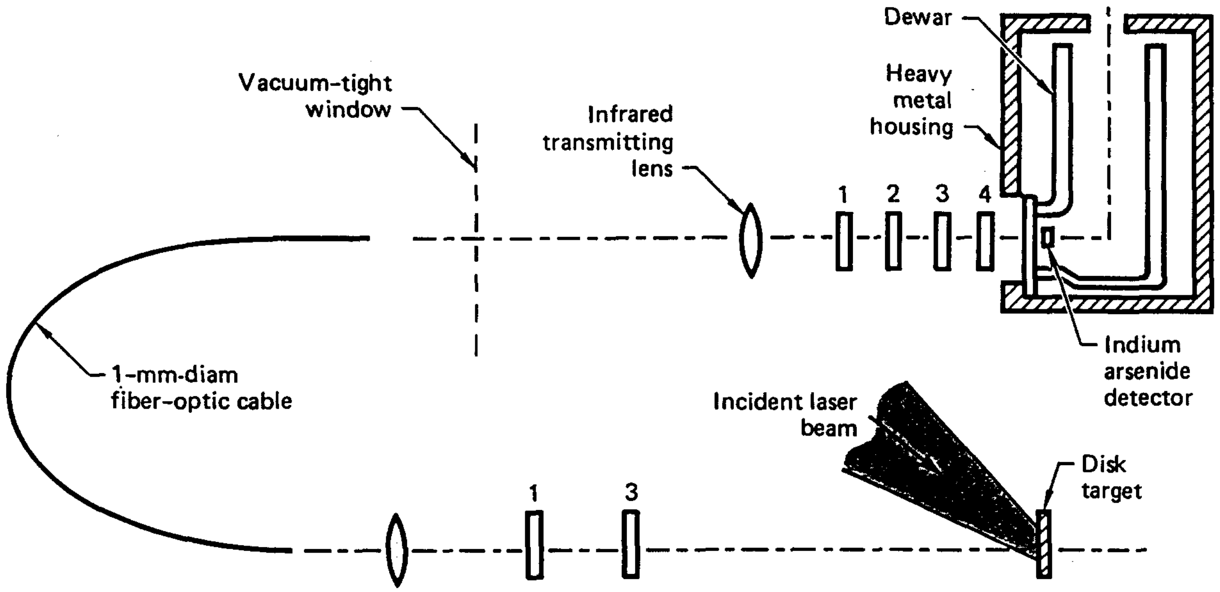

1. Visible absorbing filter: $<10^{-4}$ transmittance below 0.75 μm.
2. 5-mm-thick lead glass.
3. Near-infrared absorbing filter: $<10^{-3}$ transmittance below 1.2 μm with 1.06 μm blocking coating ($<10^{-6}$ transmittance at 1.06 μm).
4. Bandpass interference filter.

Table 5-14. FFLEX channels and energy coverage.

Prefilter	Fluorescer	Post-filter	Energy coverage, keV
Mo	Y	Y	17–20
Dy	Sm	Sm	47–50
W	Yb	Yb	61–70
Pb	Au	Au	80–88
Pb			Background channel

distribution. This distribution, along with the laser-system calorimetry, was employed to calculate target absorption, and an LLNL ultrafast optical streak camera was used to record the temporal shape of the incident laser pulse. For the second set of experiments, we used an indium arsenide infrared detector and a set of bandpass interference filters to record the emission of Raman scattered light (in the 1.6-to-2.2-μm wavelength range). A diagram of a typical Raman detector unit is shown in Fig. 5-73. Three x-ray spectrometers measured the spectrum of the x-ray emission. The filter-fluorescer spectrometer[31] used the four channels described in Table 5-14 to obtain an x-ray spectrum between 20- and 80-keV photon energy. A background channel was used to monitor noise interference from electromagnetic pickup and high-energy x rays of a few hundred keV energy, which could penetrate the lead shielding surrounding the detectors. The low-energy

Table 5-15A. Dante channels and energy coverage.

Channel	Filter	Absorption edge, keV	Cathode type	Channel width, eV[a]
1	Formvar $C_{10}H_{16}O_5$	0.28	Al	110
2	V	0.52	Al	125
3	Cr	0.58	Al	110
4	Fe	0.71	Al	270
5	Co	0.79	Al	240
6	Ni	0.86	Al, Cr	160
7	Cu	0.94	Cr	170
8	Zn	1.03	Cr, Ni	180
9	Al	1.56	Ni	470
10	Al	1.56	Ni	250

[a] Upper limit of channel is at absorption edge.

Table 5-15B. Mirror Dante channels and energy coverage.

Channel	Mirror	Cut off energy, keV	Filter	Absorption edge, keV	Cathode type	Channel width, eV[a]
1	C	0.2	Bo	0.19	Al	48
2	Be	0.4	Formvar	0.28	Al	100
3	C	0.55	V	0.52	Al	150
4	C	0.75	Cr	0.58	Al	100
5	C	0.75	Co	0.79	Al	210
6			Al	1.56	Al	550

[a] Upper limit of channel is at absorption edge.

Table 5-16. X-ray streak camera channels and energy coverage.

Filter	K-edge, keV
Polyvinyl chloride	1.7
Zn	9.7
Se	4.5
Ti	5.0
V	5.5
Co	7.7
Ag	25.5

x-ray emission was measured by the Dante[32] and Mirror Dante x-ray spectrometers. Table 5-15 indicates the energy coverage for each of the K-edge-filtered x-ray diode channels in the two systems. The Dante spectrometers have their x-ray diodide detectors connected to fast oscilloscopes and transient digitizers, which allows these instruments to obtain time-resolved as well as time-integrated spectra.

The temporal history of the high-energy x-ray emission (~60 keV) was measured with a microchannel plate detector located behind the 80-keV filter-fluorescer channel, the LLNL x-ray streak camera[33] with a multichannel K-edge filter pack, and an S-1 optical streak camera modified to observe both scattered laser light and x rays of photon energies greater than 30 keV simultaneously. The double observation is accomplished by placing a sheet of lead over a portion of the optical streak-camera slit. This optical/x-ray diagnostic was available only for the 600-ps laser-pulse experiments and was sensitive to only the brightest x-ray flashes. Table 5-16 shows the filter channels and energy coverage for the LLNL x-ray streak camera. These diagnostics will be discussed further in "X-ray Temporal Measurements."

Figures 5-74(a) and 5-74(b) show the beam alignment into standard and modified Cairn hohlraums, respectively. The Shiva laser[34] has two clusters of 10 beams. Each cluster has five inner beams inclined at 9.7° to the chamber axis and five outer beams inclined at 17.6° to the chamber axis. Each beam has an f/6 lens to focus the laser pulses at the center of the target chamber. The azimuthal separation between each inner and adjacent outer beam in the cluster is 36°. Both figures show a cross section of the target and the positions of one inner and one outer beam in each cluster. Because of the fivefold symmetry of each cluster, the diagrams show the positioning for all the other beams.

The standard Cairn alignment in Fig. 5-74(a) indicates that the inner beams irradiate the end cap of the hohlraum and that the outer beams primarily irradiate the lateral surface of the hohlraum. As plasma blows out from the lateral surface, however, refraction of the outer beams can occur, causing them to also irradiate the end cap and produce a much higher intensity than planned. The highest incident intensities for a 2.0-E Cairn irradiated with a 6-kJ/2-ns pulse are, ignoring refractive effects, approximately 2.5 × 10^{14} W/cm^2. Peak intensities for the larger hohlraums are about 4.5 × 10^{13} W/cm^2. For an 8-kJ/600-ps pulse, on the other hand, peak intensities in a 2.0-E hohlraum are about 10^{15} W/cm^2.

In the modified-Cairn alignment scheme, Fig. 5-74(b), all beams are positioned to irradiate the end caps of the hohlraum. This arrangement tries to avoid refraction of beams in the plasma evolving from the hohlraum's lateral surface, as described in the previous paragraph. For the 5/8-3.0-scale

Fig. 5-74. Beam-alignment diagrams for (a) the standard and (b) modified Cairn-E hohlraums. The standard alignment indicates that Shiva's inner beams irradiate the end cap of the hohlraum while the outer beams irradiate the hohlraum's lateral surface; however, the outer beams can be refracted by plasma blowoff, causing them to irradiate the end cap and produce higher-than-anticipated intensities. In the modified scheme, all beams are positioned to irradiate the end caps of the hohlraum, thereby avoiding refraction.

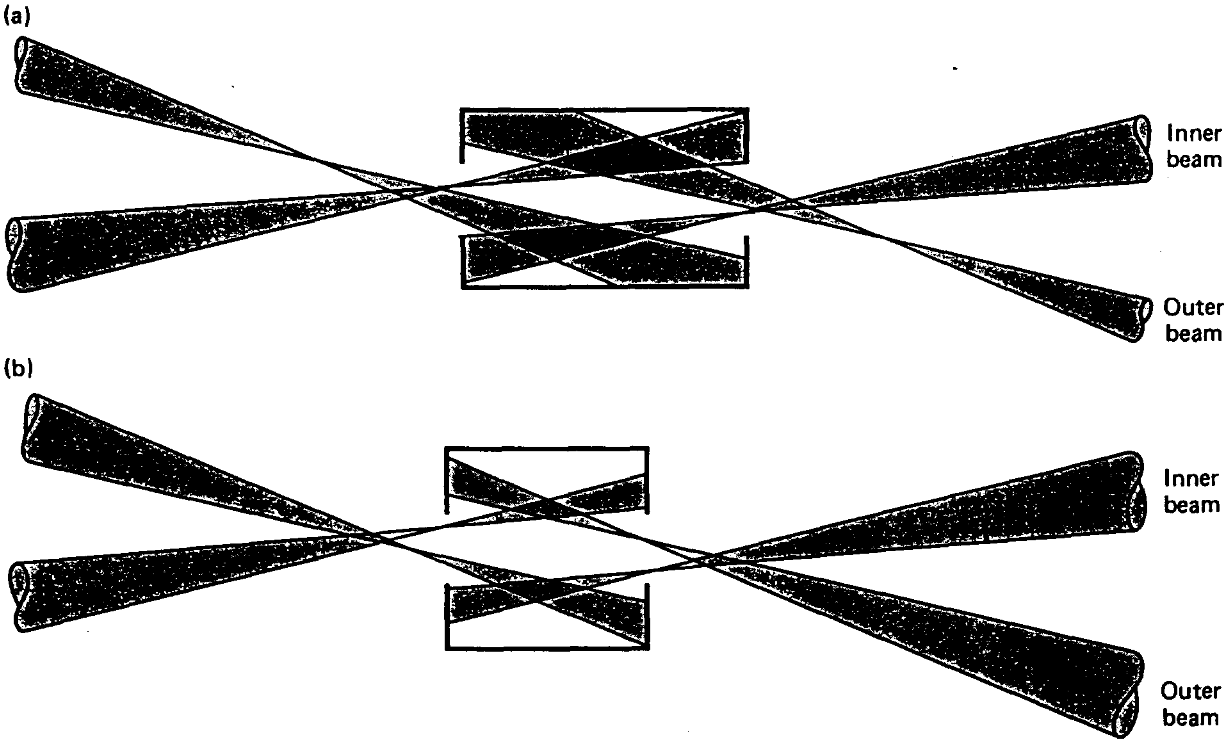

hohlraum irradiated by an 8-kJ/600-ps laser pulse, the maximum incident laser intensity on the end caps is 8.7 × 10^{14} W/cm^2; for the 5/8-4.0-scale hohlraum, the maximum intensity is 5 × 10^{14} W/cm^2.

Experimental Results

The experiments were carried out in two sequences: one set of 2-ns irradiations (22 target shots) followed by one set of 600-ps irradiations (12 target shots). Table 5-17 lists all the shots and the principal parameters, including the shot number, the target type and identification number, the energy and duration (FWHM) of the laser pulse, the fraction of laser energy absorbed, the effective blackbody radiation temperature (T_R) in electron volts, and the high-energy x-ray flux (keV/keV) at 50 (I_{50}) and 80 keV (I_{80}). Two numbers are shown under "absorption fraction" for each entry; the upper number corresponds to data obtained from the scattered-light photodiodes, and the lower number corresponds to data obtained from the LC-21 scattered light calorimeters. The target description contains three items of information. For example, 2.0 E-1 indicates that the target is a standard 2.0-scale Cairn, that it is empty, and that it has one diagnostic hole.

Absorption Measurements. In the irradiation of hohlraums by the 2-ns laser pulses, the underdense plasma has more time to fill the hohlraum before peak laser intensity, as compared to an irradiation by a 600-ps pulse. Hence, the 2-ns absorption measurements provide a "worst case" or "lower limit" on absorption for this experimental sequence. The results of the measurements are shown in Fig. 5-75. The absorption fractions clearly indicate no degradation of absorption due to Brillouin scattering. For the smaller hohlraums, measurements were

Table 5-17. Cairn-E scaling study-shot summary.

Shot No.	Cairn target	Laser pulse, kJ/ns	Absorption fraction, %	T_R, eV	I_{50}, keV/keV	I_{80}, keV,keV	Comments
89112003	189 5.0 E-1	5.83/2	83 83	93	4.36×10^{11}		No 80-keV filter-fluorescer signal
89112103	196 5.0 E-1	6.06/2	79 73	97	0.53×10^{11}		No 80-keV filter-fluorescer signal
89112604	190 3.0 E-1	6.19/2	81 73	122	2.39×10^{14}	7.40×10^{13}	
89112606	194 3.0 E-1	5.23/2	77 70	119	1.70×10^{14}	5.04×10^{13}	
89112704	192 2.0 E-1	6.33/2	87 82	162	8.78×10^{14}	2.25×10^{14}	
89112708	191 2.0 E-1	5.67/2	82 78	164	6.31×10^{14}	1.66×10^{14}	
89120406	201 3.0 E-1	1.60/2	84 75	92	6.39×10^{11}	5.06×10^{11}	
89120506	204 4.0 E-1	5.87/2	80 75	104	6.85×10^{12}	6.62×10^{11}	
89120603	203 4.0 E-1	6.25/2	81 75	108	1.24×10^{13}	6.05×10^{11}	
89120605	202 3.0 E-1	3.44/2	81 73	110	1.58×10^{13}	4.30×10^{12}	
89120703	206 5.0 E-1	5.74/2	92 87	93	3.04×10^{12}	6.79×10^{11}	
89120706	199 2.0 E-1	2.87/2	82 70	123	1.40×10^{14}	4.24×10^{13}	Outer-beam irradiation
89121001	200 2.0 E-1	2.85/2	79 79	124	1.45×10^{14}	3.26×10^{13}	Inner-beam irradiation
89122003	209 2.0 E-1	2.13/2	83 79	116	6.00×10^{13}	1.88×10^{13}	
89122006	211 2.0 E-1	1.00/2	85 80	103	5.27×10^{12}	7.51×10^{11}	
80011003	210 2.0 E-1	0.42/2	90 77	77			No filter-fluorescer data
80011006	218 2.0 E-1	0.55/2	87 76	86			No filter-fluorescer data
80011412	217 2.0 E-1	4.99/2	79 79	135	2.58×10^{14}	4.62×10^{13}	
80011419	219 2.0 E-1	4.69/2	85 80	133	4.48×10^{14}	9.97×10^{13}	
80011503	215 2.0 E-1	4.17/2	78 75	143	1.75×10^{14}	3.86×10^{13}	
80011605	221 2.0 E-1	2.20/2	82 76	133	1.24×10^{14}	3.19×10^{13}	
80011704	214 3.0 E-1	3.01/2	84 78	105	1.47×10^{13}	3.21×10^{12}	
80030505	223 3.0 E-1	7.54/0.6	86 76	143	3.30×10^{14}	1.30×10^{14}	
80030605	234 5/8-4.0 E-1	8.19/0.6	71 70	141	6.91×10^{13}	3.09×10^{13}	
80031010	230 5/8-3.0 (E-1)	7.69/0.6		144	7.36×10^{13}	3.46×10^{13}	No absorption data
80031103	229 2.5 E-1	6.35/0.6	80 77	158	2.89×10^{14}	1.03×10^{14}	
80031204	231 2.5 E-1	8.00/0.6	83 [illegible]	164	4.67×10^{14}	2.16×10^{14}	

Table 5-17. Continued.

Shot No.	Cairn target	Laser pulse, kJ/2 ns	Absorption fraction, %	T_R, eV	I_{50}, keV/keV	I_{80}, keV,keV	Comments
80031406	236 5/8-4.0 (E-1)	6.13/0.6		143	4.77×10^{13}	4.29×10^{13}	No absorption data
80031704	239 2.0 E-1	7.86/0.6	80 60	174	1.16×10^{15}	8.37×10^{14}	
80031903	232 5/8-3.0 (E-1)	9.22/0.6	84 80	147	4.63×10^{14}	1.88×10^{14}	
80032006	240 2.0 E-1	8.00/0.6	77 75	173	9.92×10^{14}	5.98×10^{14}	
80032502	226 3.0 E-1	7.12/0.6	86 83	147	3.05×10^{14}	1.27×10^{14}	
80040802	246 5/8-4.0 (E-1)	7.37/0.6	87 87	144	5.65×10^{13}		Bad spectral data at 80 keV
80040805	252 5/8-3.0 (E-1)	7.61/0.6	84 81	159	1.73×10^{14}		Bad spectral data at 80 keV

Fig. 5-75. Cairn-E absorption measurements at τ = 2 ns.

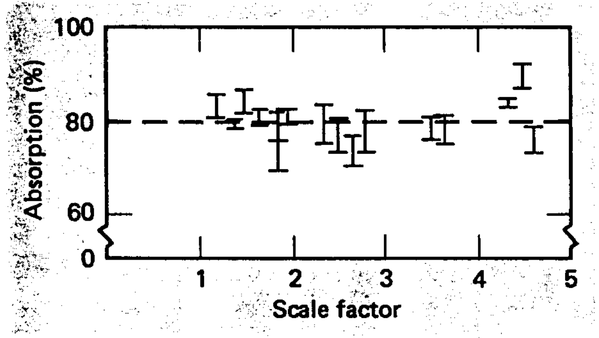

made at several energies ranging from one to six kilojoules. For all irradiation geometries and hohlraum sizes, these targets absorbed (80% ± 10%) of the incident laser energy. The range of values on each measurement is the difference between the value obtained from the scattered-light photodiodes (upper) and that obtained from the scattered-light LC-21 laser calorimeters (lower). An average absorption of 80% has been typical of all Cairn targets irradiated by Shiva.

Thermal X-ray Measurements. Using the Dante and Mirror Dante low-energy x-ray spectrometers, we have made measurements to determine how the thermal x-ray drive scales with the three macroscopic parameters: laser energy, laser pulse width, and hohlraum size. The thermal x-ray drive, I_R, is related to the blackbody radiation temperature, T_R, by the equation

$$I_R = \sigma T_R^4 \qquad (2)$$

where σ is the Stefan–Boltzmann constant. The Dante instruments measured the thermal x-ray spectrum by looking into the hohlraum through a 300- to 400-μm-diam hole drilled in the cylindrical surface. By equating the integral under the x-ray spectrum to the product of the hole area, laser pulse width, and σT_R^4, we find the "equivalent" time-averaged radiation temperature T_R.

The choice of scaling parameter for I_R is founded on previously reported theoretical considerations.[35] The scaling parameter, η, in terms of laser energy (E), pulse width (τ), and hohlraum scale (S), is

$$\eta = \frac{E}{S^2 (\tau)^{1/2}} = \frac{E}{S^2 \tau^{1/2}} \ . \qquad (3)$$

This parameter comes from an analyis of energy transfer in the material ablating away from the walls of the hohlraum. The laser energy is

Fig. 5-76. Blackbody-intensity scaling law.

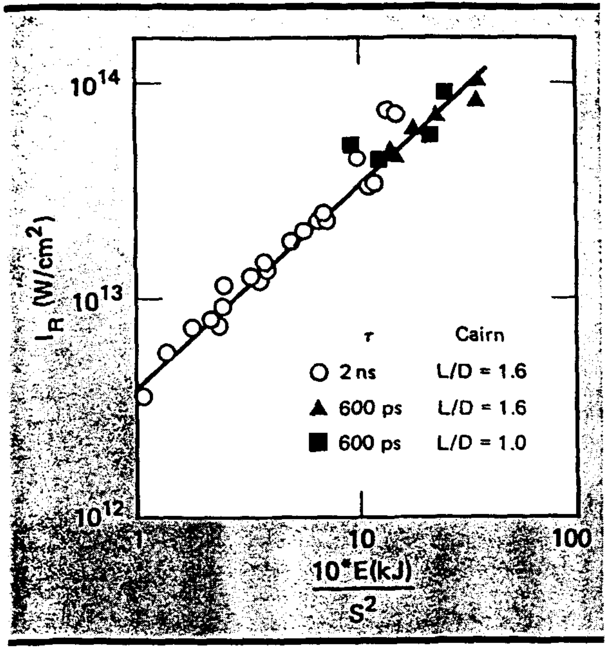

absorbed by the material and is converted into x rays and hydrodynamic motion of the plasma. Solution of the equations of motion and energy transfer (including radiative transfer) gives expressions for the temperature and density profiles (Marshak waves) near the wall. By equating the expressions for laser light converted into x rays and the x-ray energy flowing out of the Marshak wave, one finds that the blackbody temperature scales with the parameter η in Eq. (3). Figure 5-76 shows the radiation intensity data plotted against η for the 2-ns experiments, the standard Cairn hohlraums irradiated at 600 ps, and the modified Cairn hohlraums irradiated at 600 ps. The data show excellent correlation with η, and obey the scaling law

$$I_R = 3.08 \times 10^{13} \left[\frac{E(kJ)}{S^2} \sqrt{\frac{2\ \text{ns}}{\tau\ (\text{ns})}} \right]^{0.96} \text{W/cm}^2 \quad . \qquad (4)$$

This relationship is being used to specify the operating point for the latest high-density targets on Shiva.

As described in "Experimental Details," the Dante systems can provide time-resolved spectra and, hence, time-resolved radiation temperature and drive. To illustrate this capability, Fig. 5-77 shows the time history of the radiation temperature of a 5/8-4.0-E Cairn irradiated by an 8.2-kJ/600-ps pulse. The time-resolved temperature history shows a peak temperature of $T_R \cong 136$ eV. This value is very close to the radiation temperature calculated from Dante waveforms that are not corrected for the temporal response of the detector electronic system. The peak amplitude of the waveform that is used in this second type of calculation is determined by dividing the area of the unresolved waveform by its width at half amplitude. For the unresolved data corresponding to Fig. 5-77, a peak temperature of $T_R \cong (138 \pm 3$ eV) was obtained. Later we will compare time-resolved Dante data with time-resolved, high-energy x-ray spectral data to show the temporal relation between x-ray drive and preheat. If the underdense plasma filling the hohlraum were always the dominant source of hot electrons, the peak of the thermal drive might occur ahead of the peak of the high-energy x-ray emission. This effect will be more pronounced the larger the hohlraum because the filling time is longer. For small hohlraums, or where hot electrons are produced by resonance absorption, the peaks of the thermal and high-energy x-ray emissions should be more nearly coincident. This will be discussed below.

Fig. 5-77. Time-resolved x-ray temperature for a 5/8-4.0-scale Cairn-E hohlraum irradiated by a 8.2-kJ/600-ps laser pulse.

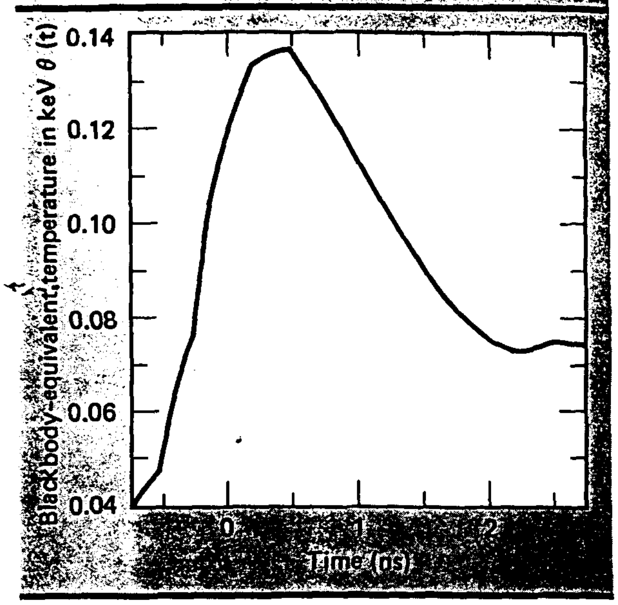

High-Energy X-ray Spectral Measurements. We made extensive measurements with the filter-fluorescer spectrometer to determine the dependence of the high-energy x-ray spectra (due to the

Fig. 5-78. Cairn-E filter-fluorescer spectra at $\tau = 2$ ns (a) for a constant energy of 6 kJ and varying hohlraum sizes and (b) for a 2.0-scale Cairn-E hohlraum and energies varying from 1 to 6 kJ.

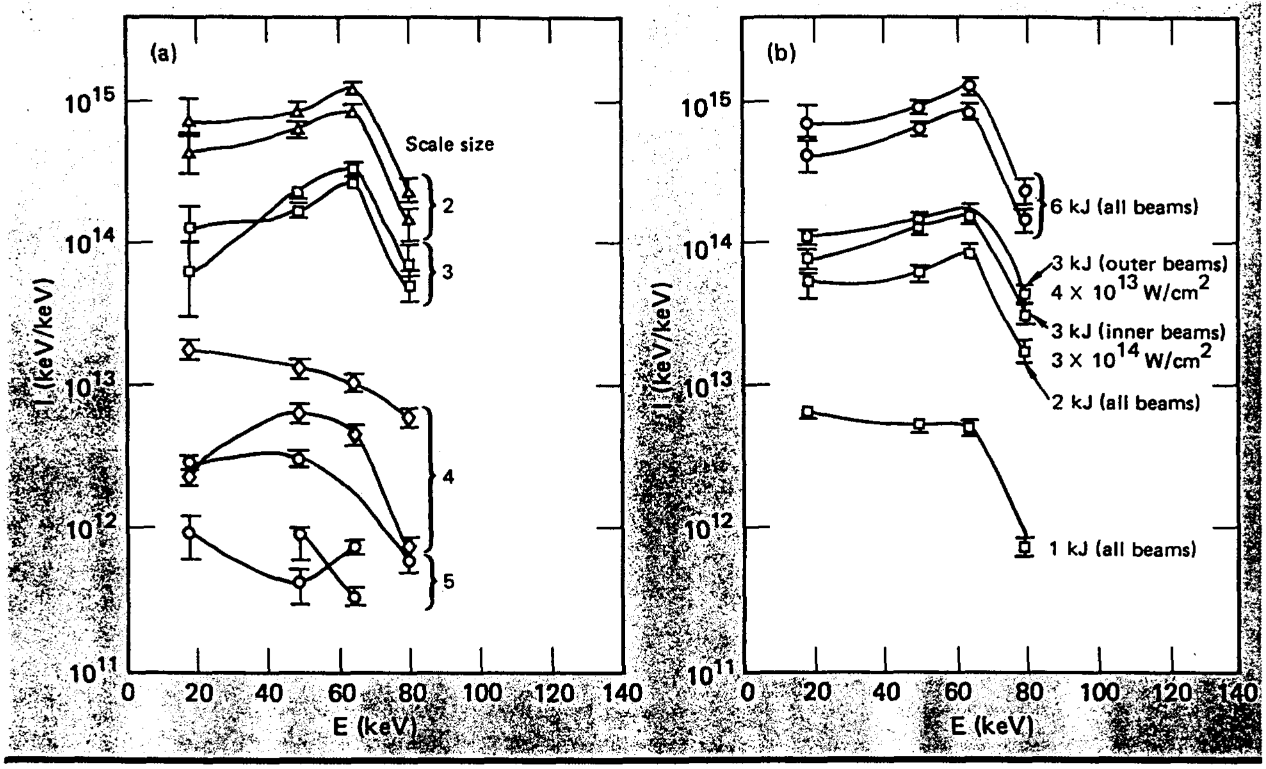

hot electrons) on three macroscopic variables: incident laser energy, laser pulse width, and hohlraum geometry (size and aspect ratio). There were two sets of experiments for the 2-ns laser pulses. Various hohlraum sizes and a constant laser energy of 6 kJ were used for the first set. The second set utilized laser energies from 0.5 kJ to 6 kJ and a single hohlraum size (2.0-E Cairn). These two sets allowed us to examine the effects of energy and size individually. Measured spectra are shown in Figs. 5-78(a) and 5-78(b).

Three interesting features are evident from the spectra. First, the spectral intensity levels vary more strongly with scale size than with energy. Second, most of the spectra have a local peak at a photon energy of about 70 keV. This is probably caused by K-line emission from the gold. Third, there is evidence in Fig. 5-78(b) that the production of hot electrons is a "volume-dependent," rather than surface-dependent, process.

We carried out two sets of irradiation experiments with an incident energy of 3 kJ. In the first, a 2.0-E hohlraum was irradiated with Shiva's "inner" beams only; the second set of shots used only the "outer" beams. The first-bounce laser intensity on the hohlraum surface was $I \leqslant 3 \times 10^{14}$ W/cm^2 for the first set and $I \leqslant 4 \times 10^{13}$ W/cm^2 for the second. Although the intensities differed by a factor of seven, the two spectra shown in Fig. 5-78(b) show no difference in shape or level, leading us to conclude that hot-electron production is strongly dependent on processes occuring within the volume of the hohlraum and not exclusively on its surface. The data only indicate the overall effect of the processes. We cannot determine how much of the hot-electron production was due to stimulated processes such as Raman instability and how much was due to enhanced resonance absorption as a result of beam refraction and intensification as the light traversed the plasma filling the hohlraum. Delineation of the processes will necessitate "microscopic" local measurements of the hohlraum environment.

From the x-ray spectra of Fig. 5-78, we have found a new scaling law. We did this by plotting the

Fig. 5-79. Dependence of x-ray flux on (a) incident energy and (b) hohlraum size at $\tau = 2$ ns.

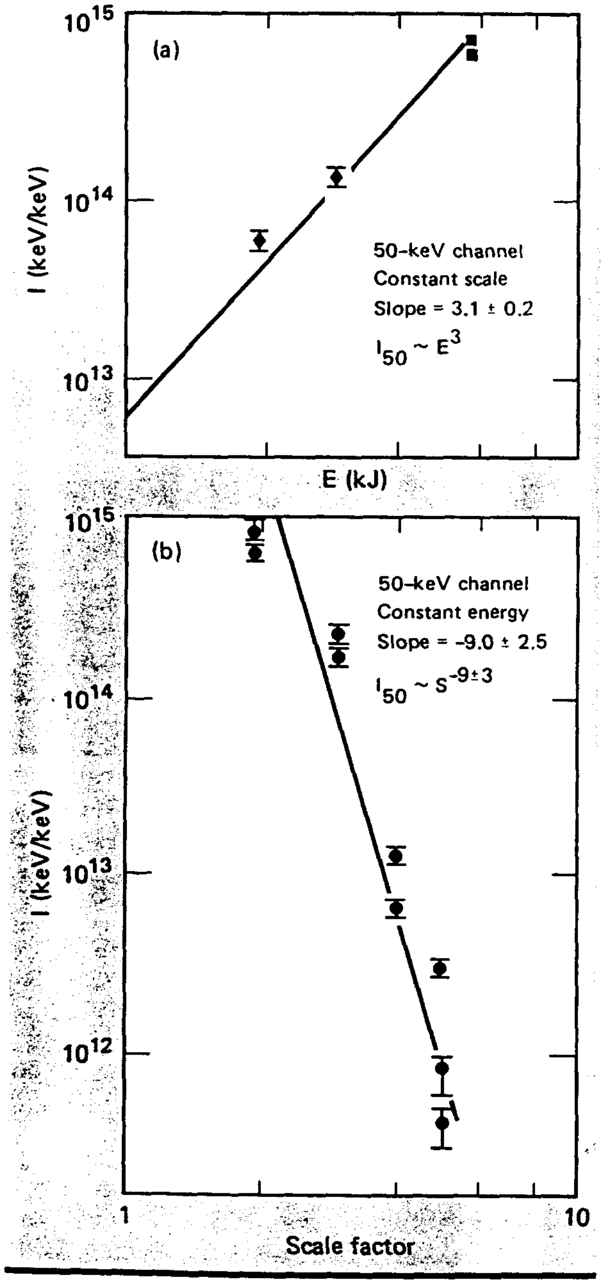

50- and 80-keV x-ray flux as a function of laser energy (E) and hohlraum scale factor (S) on log–log graphs. The results for the 50-keV channel are shown in Figs. 5-79(a) and 5-79(b). At a constant value of S, the flux at 50 keV (I_{50}) scales as E^3, and at a constant value of E, the fluence scales roughly as S^{-9}. This implies the scaling parameter is $E/S^{3\pm1}$ and

$$I_{50} \sim E/S^{(3\pm1)} \quad . \tag{5}$$

In addition to E and S, there are two other important scaling parameters: the laser pulse width, τ, and the aspect ratio, L/D (Fig. 5-71). To investigate the effects of these two parameters, we took both standard (with scale factors of 2.0, 2.5, and 3.0) and modified Cairn hohlraums (5/8–3.0 and 5/8–4.0) and irradiated them with 8-kJ/600-ps laser pulses. The 5/8–3.0 Cairn has an equivalent scale factor of 2.5, while the 5/8–4.0 Cairn has an equivalent scale factor of 3.4. The time-averaged, high-energy x-ray spectra had a shape similar to the spectra in Fig. 5-78(b). In an attempt to isolate the effects of pulse width and aspect ratio, we plotted the 50- and 80-keV x-ray-flux components for both sets of experiments (2 ns, 600 ps) versus E/S^3. The results for the 50- and 80-keV components, respectively, are shown in Figs. 5-80(a) and 5-80(b). The data indicate that both the 2-ns and 600-ps experiments have x-ray-flux data that scale well with E/S^3 and that there is no detectable dependence on the laser pulse width for the range between 600 ps and 2 ns. Since plasma density in the hohlraum must vary with time, this was a surprising result. The scaling relationships in Figs. 5-80(a) and 5-80(b) can be expressed as

$$I_{50} \cong 5 \times 10^{15}\left[\frac{E(kJ)}{S^3}\right]^3 \text{keV/keV} \tag{6}$$

and

$$I_{80} \cong 3 \times 10^{14}\left[\frac{E(kJ)}{S^3}\right]^3 \text{keV/keV} \quad . \tag{7}$$

Note that the scaling relationships, Eq. (6) and (7), are used only to describe the data for the Shiva experiments in Table 5-17. Extrapolation of these relationships should not be used for target experiments with higher values of E/S^3. The reason for such caution can be seen in the upper part of the data in Fig. 5-80(a), where the slope of the cluster of

Fig. 5-80. High-energy x-ray flux at (a) 50-and (b) 80-keV scales with E/S^3 (energy/hohlraum scale factor^3).

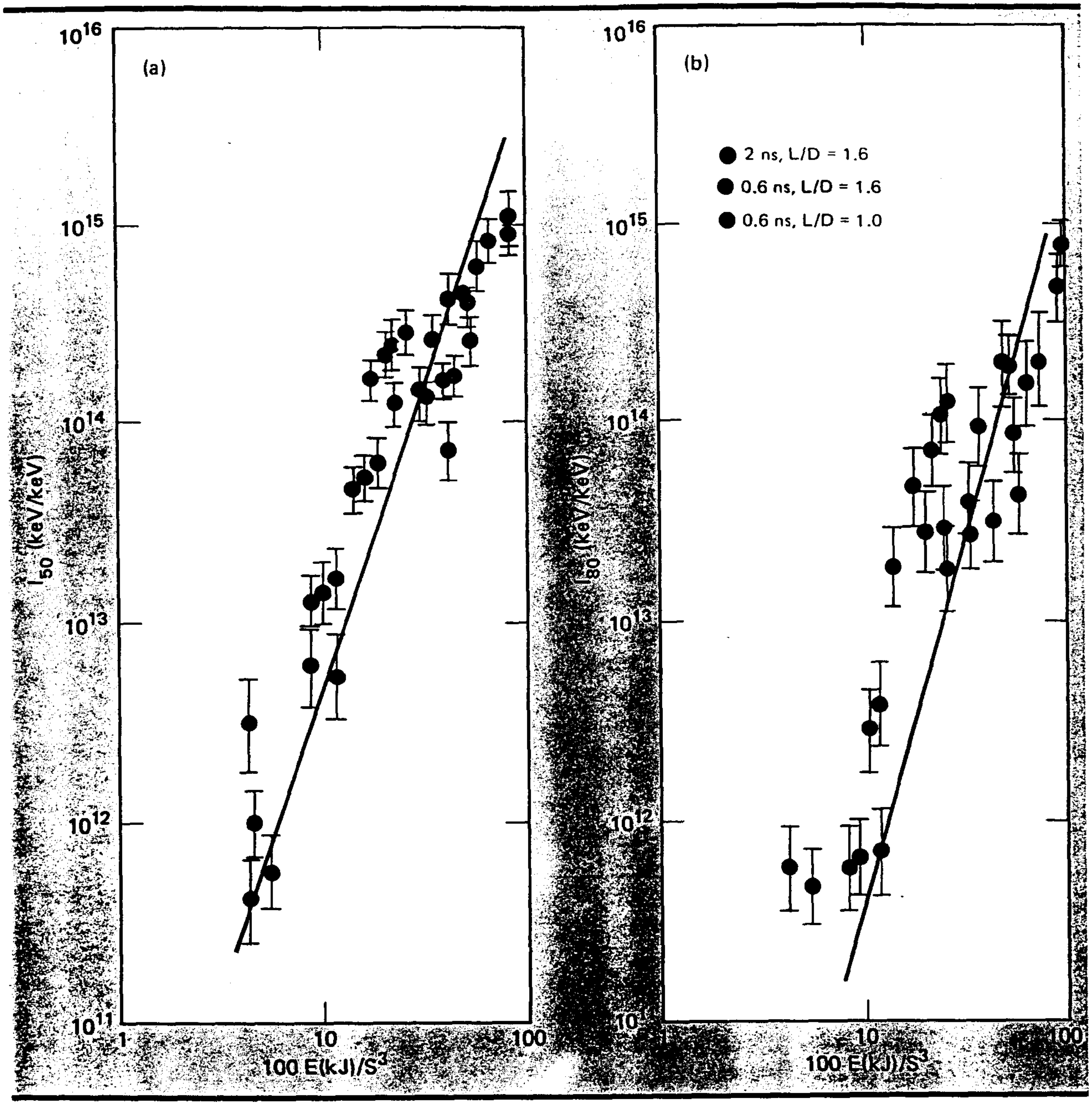

data has started to decrease (roll over). This "rolling over" implies that saturation of the hot-electron production processes is starting to take place.

In an attempt to identify a more generalized scaling relationship, we correlated the results of experiments with smaller Cairn hohlraums, with and without fuel balls, and irradiated on both Shiva and Argus as shown in Fig. 5-81. In this figure, the normalized x-ray flux at 50 keV is divided by the absorbed laser energy (0.8 E_{inc}). Data from 1.6 Cairn B targets and 0.6-scale Forerunner targets extend the range of 100 E/S^3 well past 100. The decreasing slope and the trend toward saturation are now quite evident. The upper part of the curve lies within the range of normalized fluxes that

Fig. 5-81. Temporal profile of high-energy x-ray emission measured by x-ray streak camera. Here the normalized suprathermal x-ray flux at 50 keV scales as E/S^3.

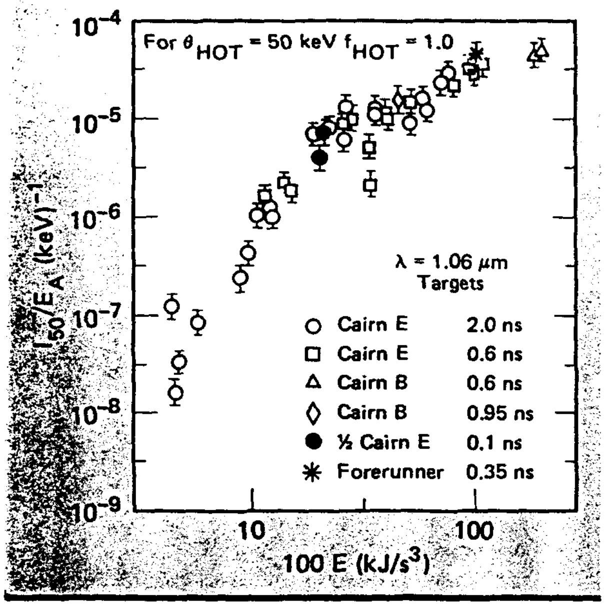

would occur if all laser energy went into a distribution of hot electrons having a Maxwellian distribution with a temperature of 50 keV. Further experiments at longer pulse duration are needed to define the time dependence. The suprathermal electron fluxes produced by the modified Cairn hohlraums did not differ by more than a factor of two from those produced by the standard Cairn hohlraums for the same value of E/S^3. On the average, their production was lower, but the scatter in the data is large. One reason for this may be that refraction of the laser beams by the hohlraum plasma is strong enough to smear out the distinct characteristics of the intensity distributions of different beam-alignment schemes.

X-ray Temporal Measurements. The high-energy x-ray temporal data for the 2-ns experiments showed a definite time delay between the peak of the laser pulse and the peak flux of high-energy x rays. This is evidence that the underdense plasma filling the hohlraum plays a predominant role in hot-electron production. Temporal x-ray data for the 600-ps-pulse experiments, on the other hand, showed no time delay between the laser pulse and production of high-energy x rays. One reason for this might be that the higher incident intensities resulting from the 8-kJ/600-ps laser pulses caused a higher plasma filling rate than the rate for hohlraums irradiated with 2-ns laser pulses. Conversely, the portion of the hohlraum filled may have been small enough that hot electrons were produced predominately by resonance absorption at the hohlraum surface. In this case, the suprathermal electron history follows the history of the incident laser pulse.

Although the x-ray streak camera is not absolutely timed with respect to the incident laser pulse, it did show relative timing information implying that hot-electron production depends on hohlraum filling. Figure 5-82(a) shows the temporal history of the x-ray emission at 10- to 25-keV photon energy for 2.0-E hohlraums irradiated at energies of 4.2 to 5.7 kJ and a pulse width of 2 ns. In each waveform, there is an initial step increase in the flux that can be attributed to the production of hot electrons by the direct irradiation of the hohlraum surface by the laser pulse. This early stage of hot-electron production may be dominated by the resonance-absorption mechanism. After a delay of about 500 ps, there is a much larger high-energy x-ray flux. This flash of x rays can be attributed to the filling of the hohlraum by underdense plasma and subsequent hot electron production by *volumetric* processes (Raman, $2\omega_{pe}$ or filamentation). The ratio of the second to the first peak is a factor of 50. Figure 5-82(b). shows the incident energy dependence of the time delay between the first and second x-ray peaks. The time delay also increased with hohlraum size, as was shown with microchannel plate measurements (to be discussed below).

The x-ray streak camera did not show this stepped structure for the 600-ps laser-pulse experiments. More information on this different behavior can be found in data collected by an optical/x-ray streak camera designed to look at scattered light and x rays of ⩾30-keV photon energy simultaneously. Half of the streak camera slit is covered with a sheet of lead that passes only high-energy x rays and blocks the scattered 1.06-μm light, which is thus incident only on the exposed half of the slit. Figure 5-83 shows the camera response due to the light and x-ray emission from a 2.0-E Cairn irradiated by a 6.4-kJ/600-ps laser pulse. Note that

Fig. 5-82. (a) Temporal profile of x-ray emission at 10- to 25-keV photon energy for 2.0-scale Cairn-E hohlraums irradiated at energies of 4.2 to 5.7 kJ and a pulse width of 2 ns. (b) Incident energy dependence on time delay between first and second x-ray peaks.

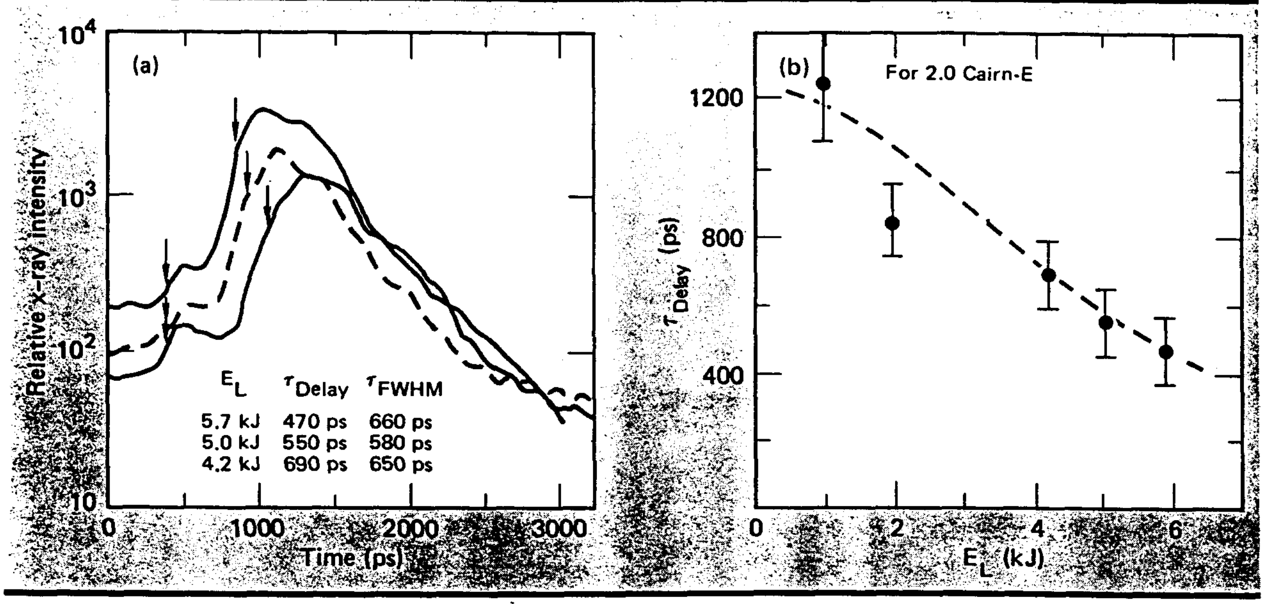

Fig. 5-83. Measurement of >30-keV x-rays by optical/x-ray interval streak camera, showing camera response due to light and x-ray emission from 2.0-scale Cairn E hohlraum irradiated by 6.4-kJ/600-ps laser pulse.

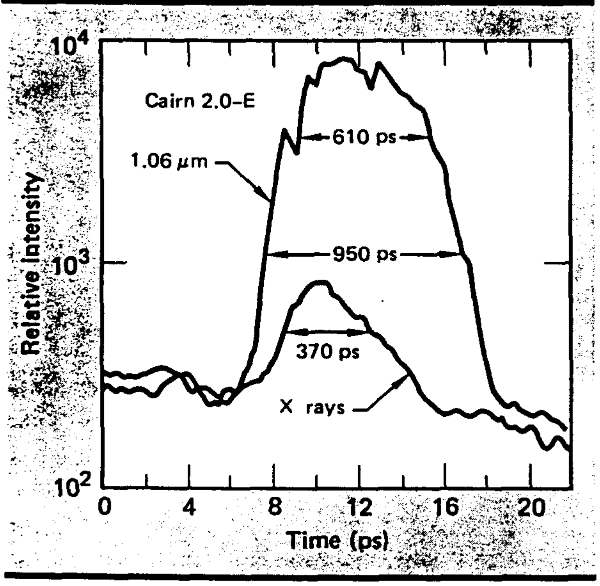

the high-energy x rays peak before the laser pulse does, suggesting early filling of the hohlraum. Early hohlraum filling can result in early STE production by two possible mechanisms. First, consider Raman instability, which is optimum at quarter-critical density. If the hohlraum reaches quarter-critical density early in the laser pulse, maximum STE production by this process will also occur early. Then, as the hohlraum fills to higher densities, the Raman production rate drops to zero, with a corresponding decrease in the level of high-energy x rays. Second, the plasma filling the hohlraum can refract the laser beams to the degree that they no longer reach the critical density layer near the wall, causing STE production by resonance absorption to cease. Again, the suprathermal x-ray levels will decrease.

In future long-pulse experiments ($\tau \geqslant 2$ ns), the optical/x-ray streak camera may provide the best information on hohlraum filling because there will be absolute timing between the laser pulse and the high energy x-ray emission.

The final set of temporal measurements to be described utilized the capability of the transient digitizers on the Dante detectors and the microchannel plate located behind the 80-keV channel of the filter fluorescer.

Figure 5-84 shows how the microchannel plate is used to obtain high-energy x-ray temporal information. A photodiode that senses laser light from one of the 20 amplifier chains provides a fiducial signal from which to reference x-ray emission

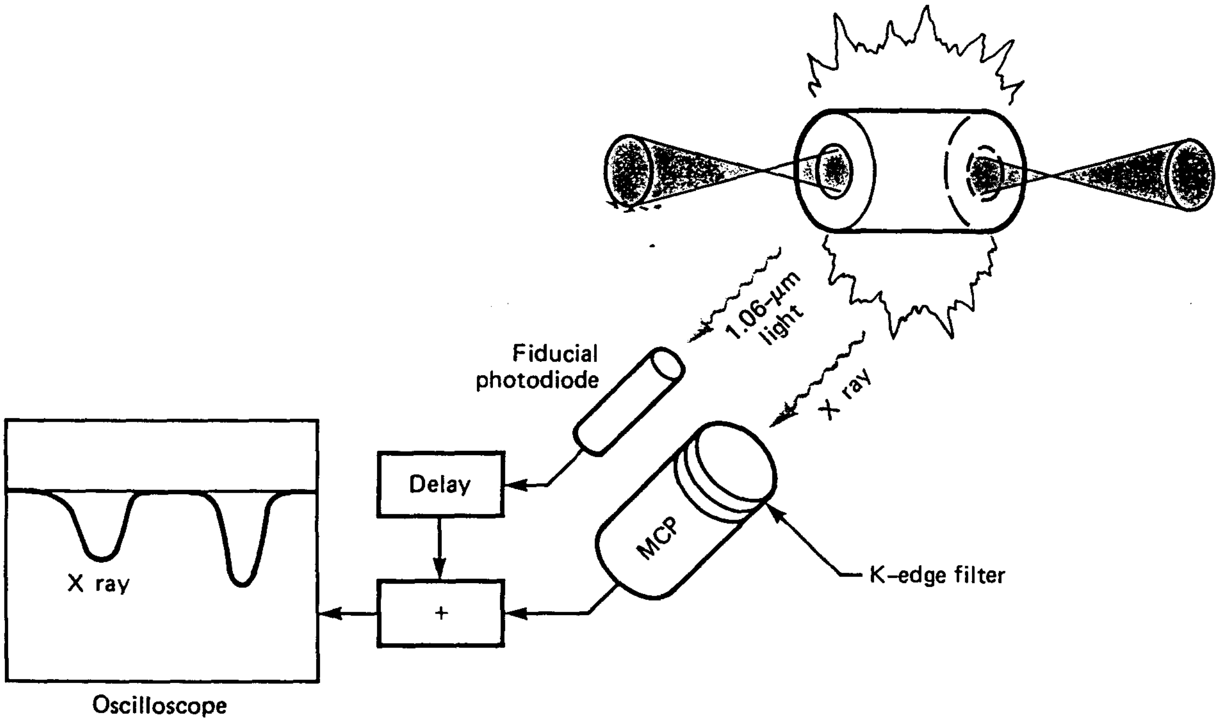

Fig. 5-84. Microchannel plate measurement of high-energy x rays. A photodiode that senses light from one of the 20 amplifier chains provides a fiducial signal to reference x-ray emission relative to the laser pulse, and x-rays passing through the K-edge filter produce a voltage at the output of the microchannel plate. Both signals are then displayed on the same oscilloscope trace, and time delays from various experiments are compared by aligning the peaks of the photodiode fiducials.

relative to the laser pulse. X rays passing through the K-edge filter (~60 keV) produce a voltage pulse at the output of the microchannel plate. The two signals are displayed on a common oscilloscope trace. Time delays from different experiments are compared by aligning the peaks of the photodiode fiducials. Dante channels use the same fiducial photodiode. Dante traces from different channels are compared by superimposing all of the fiducial traces.

The data obtained from these diagnostics demonstrated the effects of hohlraum size and incident laser energy on the time variation of thermal and high-energy x rays. The temporal behavior of thermal and high-energy x-ray emission from a disk and hohlraum are compared in Fig. 5-85. The left plot shows the output of the 500-eV Dante channel for a 2.0-E Cairn hohlraum (●) and a gold disk (▲) irradiated by 2-ns-long laser pulses. The disk reaches peak thermal emission about 500 ps before the hohlraum because of the hohlraum's higher "thermal mass". On the right, the effects of hohlraum filling are evident. The peak of the 40-keV x-ray emission from the hohlraum is about 300 ps later than the emission from the disk. Hot-electron production for the disk probably results from resonance absorption, whereas a volumetric process such as Raman instability may be the dominant source in the hohlraum.

Figure 5-86 shows the effects of varying incident laser energies on the temporal profile of x-ray emission from a 2.0-E Cairn. The hohlraum is irradiated by 2-ns pulses with energies of 3 kJ (curve A) and 6 kJ (curves B and C). The peak position for the thermal x-ray emission (left plot) and for the 40-keV emission (right plot) both changed negligibly for this range of energies. While this is to be expected for the thermal x-ray emission, the conclusions for the 40-keV x-ray emission are less clear. One speculative explanation might be that the plasma blowoff velocity reaches an "asymptotic" value, which is almost independent of laser intensity, at early times. The effects of hohlraum size are

Fig. 5-85. Temporal profile of thermal and suprathermal x-ray emission from a disk ( ) and a 2.0-scale Cairn E hohlraum ( ) irradiated by 2-ns pulses. Emission output of (a) 500-eV Dante channel (thermal) and (b) 40-keV Shiva channel (suprathermal).

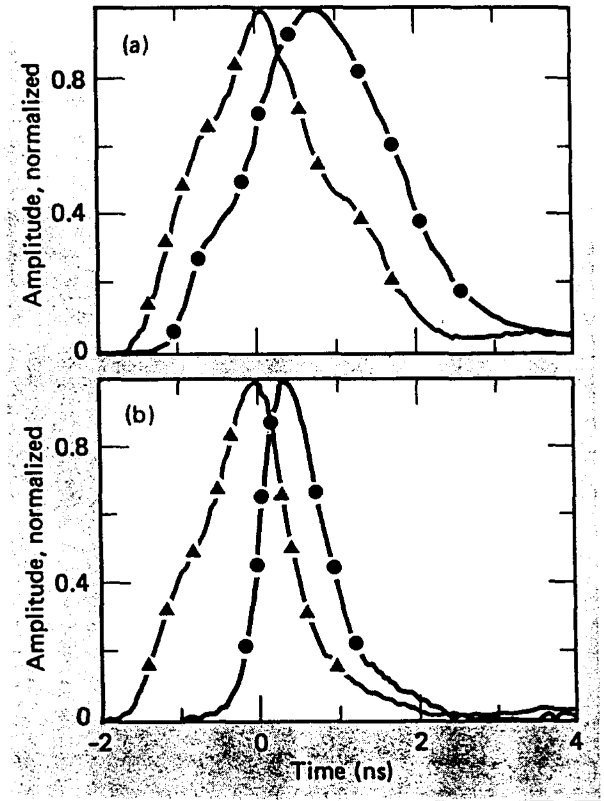

much more pronounced on the time of peak x-ray emission than the effects of incident laser energy. In Fig. 5-87, the temporal profiles of the 500- and 40-keV x-ray emission are displayed for a 2.0-E Cairn hohlraum irradiated by a 6.0-kJ/2-ns pulse and for a 3.0-E Cairn irradiated by a 3.0-kJ/2-ns laser pulse. The left plot indicates that the peak of the 500-eV x-ray emission for the 3.0-E Cairn (●) occurs 550 ps after the peak of the 2.0-E Cairn emission (▲). Once again, this delay can be attributed to the larger size of the 3.0-E hohlraum and its larger "thermal mass". The plot at right shows the effect of hohlraum size on the temporal profile of the 40-keV x-ray emission. There is a 300-ps delay of the peak emission from the 3.0-E hohlraum with respect to the peak emission of the 2.0-E hohlraum. This can be attributed to the longer time required by the 3.0-E hohlraum to reach a plasma density at which plasma processes such as Raman or $2\omega_{pe}$ leading to hot-electron production[35] occur at significant rates.

Fig. 5-86. Temporal profile of thermal and suprathermal x-ray emission from 2.0-scale Cairn-E hohlraums irradiated by 2-ns pulses with energies of 3 (A) and 6 kJ (B, C). Emission output of (a) 500-eV Dante channel (thermal) and (b) 40-keV Shiva channel (suprathermal).

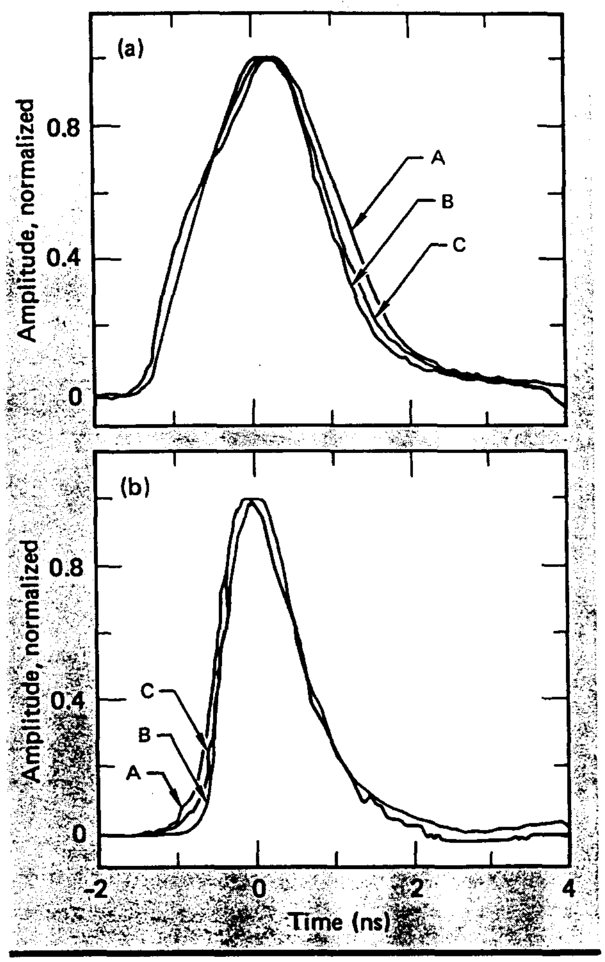

Raman Light Measurements. The Raman light detector[36] described in "Experimental Details" was brought into operation toward the end of this study. However, the few measurements made with it indicate that Raman instability contributes in part to STE production. The experiments were all done with a laser pulse width of 600 ps. Data are presented here for both empty hohlraums and hohlraums with fuel-ball assemblies. Two modified Cairn hohlraums (one 5/8–3.0-E and one 5/8–4.0-E) irradiated at 8 kJ/600 ps produced Raman scattered light of peak spectral intensity 115 and 87 J/sr-μm, respectively, at a wavelength of 1.8 μm.

Fig. 5-87. Temporal profile of thermal and suprathermal x-ray emission from 2.0-E ( ) and 3.0-scale ( ) Cairn-E hohlraums irradiated by 2-ns pulses having respective energies of 6.0 and 3.0 kJ. Emission output of (a) 500-eV Dante channel (thermal) and (b) 40-keV Shiva channel (suprathermal).

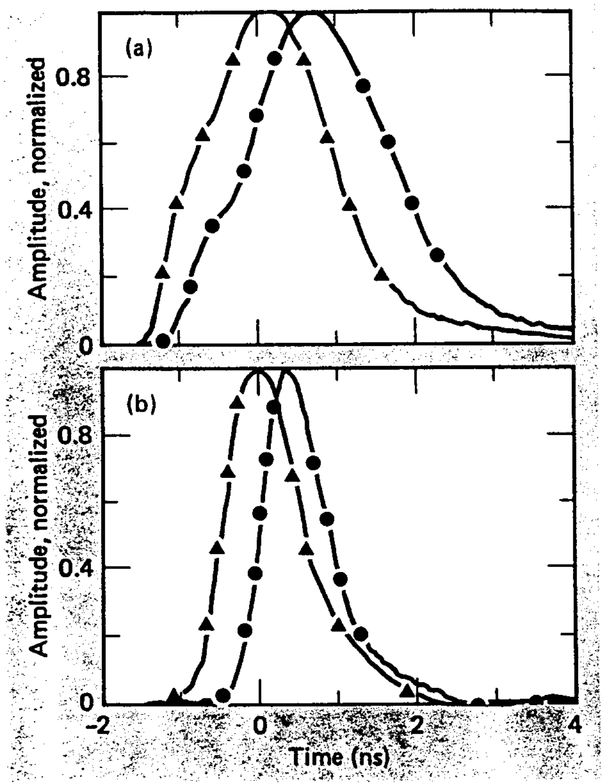

These data are illustrated in Fig. 5-88. The Raman instability works optimally at quarter-critical density, which corresponds to a Raman light frequency of 2.12 μm for 1.06-μm light. The fact that the peak observed intensity occurred at 1.8 μm implies that the instability scattered incident laser light at densities below one-quarter critical.

The Raman light levels measured from the modified Cairns were low compared to levels from hohlraums containing fuel-capsule assemblies irradiated during the same time period. We carried out several experiments with 2.0-scale standard hohlraums containing fuel balls mounted on a 400 Å formvar sheet in the center plane of the hohlraum, positioning the 20 Shiva beams to irradiate this formvar sheet rather than the gold walls of the hohlraum. When irradiated, the sheet forms a low-Z underdense plasma that fills the hohlraum. Because of its lower Z, the plasma probably reaches quarter-critical later than a gold plasma; thus, Raman instability occurs closer to peak laser power than it did in an empty hohlraum (see Fig. 5-82). This is one possible explanantion for the observed higher Raman light levels at 1.6 μm. Another explanation is that the fuel-capsule assembly may alter the shape of the Raman spectrum, giving the higher levels. Future experiments with a Raman spectrograph are needed to answer this question. As shown in Fig. 5-87, the levels of Raman light were between 400 and 600 J/sr-μm at a wavelength of 1.8 μm, and 200, 150, and 50 J/sr-μm at wavelengths of 1.6, 2.0, and 2.12 μm, respectively. This last wavelength point corresponds to light that must have been scattered from electron plasma waves very near quarter-critical density. The data have shown that the Raman instability is operative in hohlraums and may, therefore, account for some of the suprathermal electrons. The Raman instability and its dynamics in hohlraums will be discussed in the "Cairn Hohlraum Scaling Study" that follows.

Summary

We have completed the first set of experiments to characterize the physics of empty hohlraums. There is strong evidence that the production of suprathermal electrons occurs, in part, in the underdense plasma that fills the hohlraum. The two principal items of evidence are (1) the delay of suprathermal x rays with respect to the incident laser pulse for long pulses and (2) the measurement of large amounts of Raman scattered light. However, for the 600-ps laser-pulse experiments, the absence of a time delay between the high-energy x rays and the laser pulse indicates that processes occuring on the hohlraum surface (such as resonance absorption) are producing large numbers of suprathermal electrons.

The relative contribution of each process was not discernible in these experiments since the latter were macroscopic in nature. Only a spatially- and time-resolved microscopic measurement of the plasma density distribution inside the hohlraum will indicate which processes are dominant at each point of space and time. Additional scaling experiments will also provide useful information. Sequences of Cairn irradiations at short (τ = 200 ps FWHM) and long pulses ($\tau \geqslant$ 3 ns) will most likely reveal the

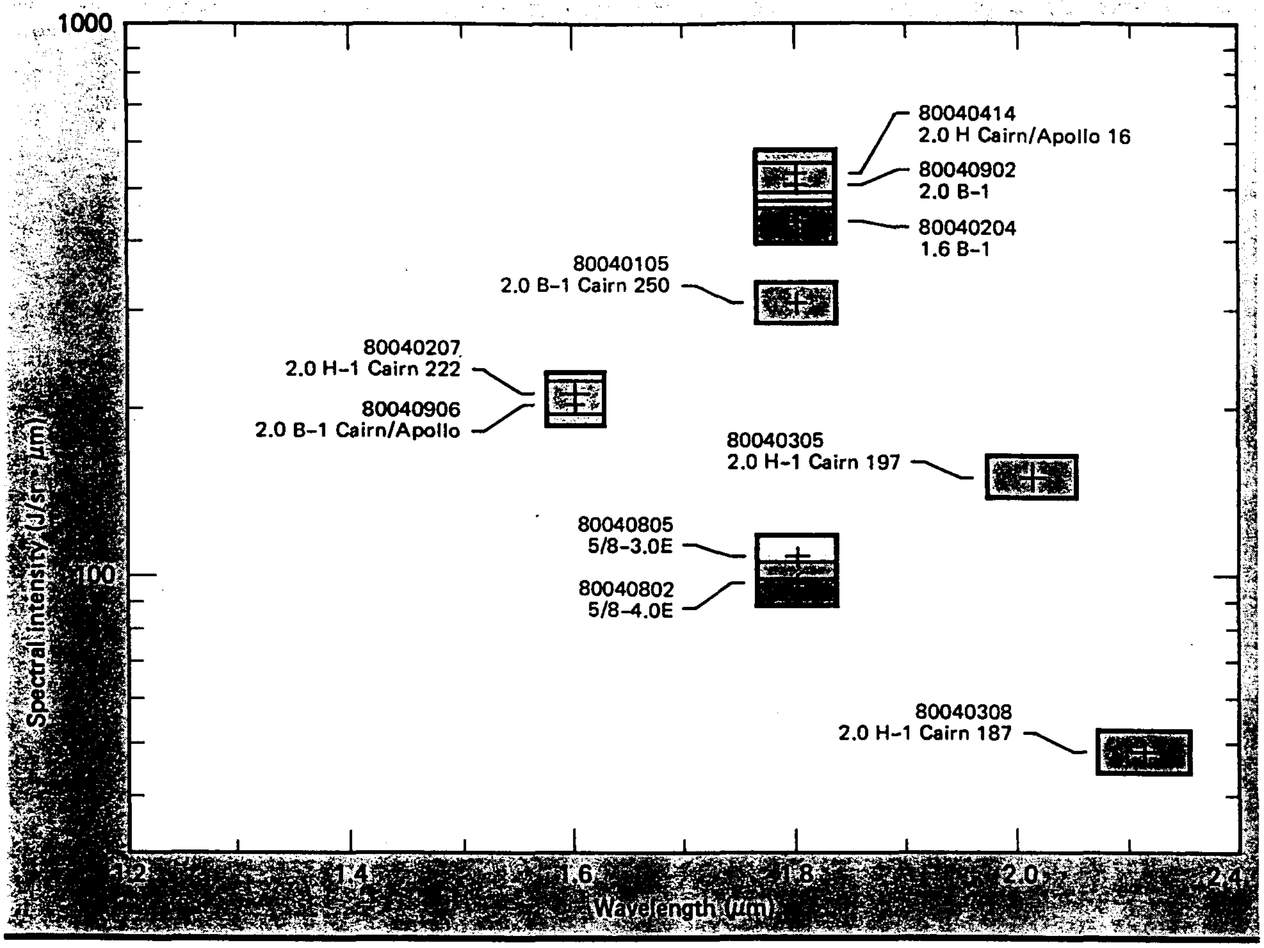
Fig. 5-88. Raman emission from Cairn hohlraums irradiated by 600-ps pulses with energies of 8 kJ.

scaling of preheat levels on laser pulse width—a relationship that was not determined with the 600-ps-to-2-ns range of pulse widths used in the experiments described here. The short-pulse experiments will yield data under conditions at which resonance absorption probably predominates, while the long-pulse experiments will indicate STE production rates under conditions at which a significant plasma density exists in the hohlraum. Furthermore, the long-pulse experiments have pulse durations proposed for Nova targets and thus would provide crucial target design data.

Authors: J. M. Auerbach and K. R. Manes

Major Contributor: D. W. Phillion

References

27. K. G. Estabrook, E. J. Valeo, and W. L. Kruer, "Two-Dimensional Relativistic Simulations of Resonance Absorbtion," *Phys. Fluids* **18**, 1151 (1975).
28. A. B. Langdon and B. F. Lasinski, "Filamentation and Subsequent Decay of Laser Light in Plasmas," *Phys. Rev. Lett.* **34**, 934 (1975).
29. W. L. Kruer, K. G. Estabrook, B. F. Lasinski, and A. B. Langdon, *Raman Backscatter in High-Temperature Inhomogeneous Plamsa*, Lawrence Livermore National Laboratory, Livermore, Calif., UCRL-82394 (1979).
30. A. B. Langdon, B. F. Lasinski, and W. L. Kruer, "Nonlinear Saturation and Recurrence of the Two-Plasmon Decay Instability," *Phys. Rev. Lett.* **43**, 133 (1979).
31. B. L. Pruett, K. G. Tirsell, H. N. Kornblum, S. S. Glaros, D. E. Campbell, and V. W. Slivinsky, *A 10-Channel Filter Fluorescer Spectrometer*, Lawrence Livermore National Laboratory, Livermore, Calif., UCRL-81477 (1978).
32. K. G. Tirsell, H. N. Kornblum, and V. W. Slivinsky, *Time Resolv osub-keV X-ray Measurements Using Xrray Diodes*, Lawrence Livermore National Laboratory, Livermore, Calif., UCRL-81478 (1979).

Fig. 5-89. Radiation temperature (T_R) vs Marshak wave-scaling parameter for 2-ns hohlraum experiments on Shiva.

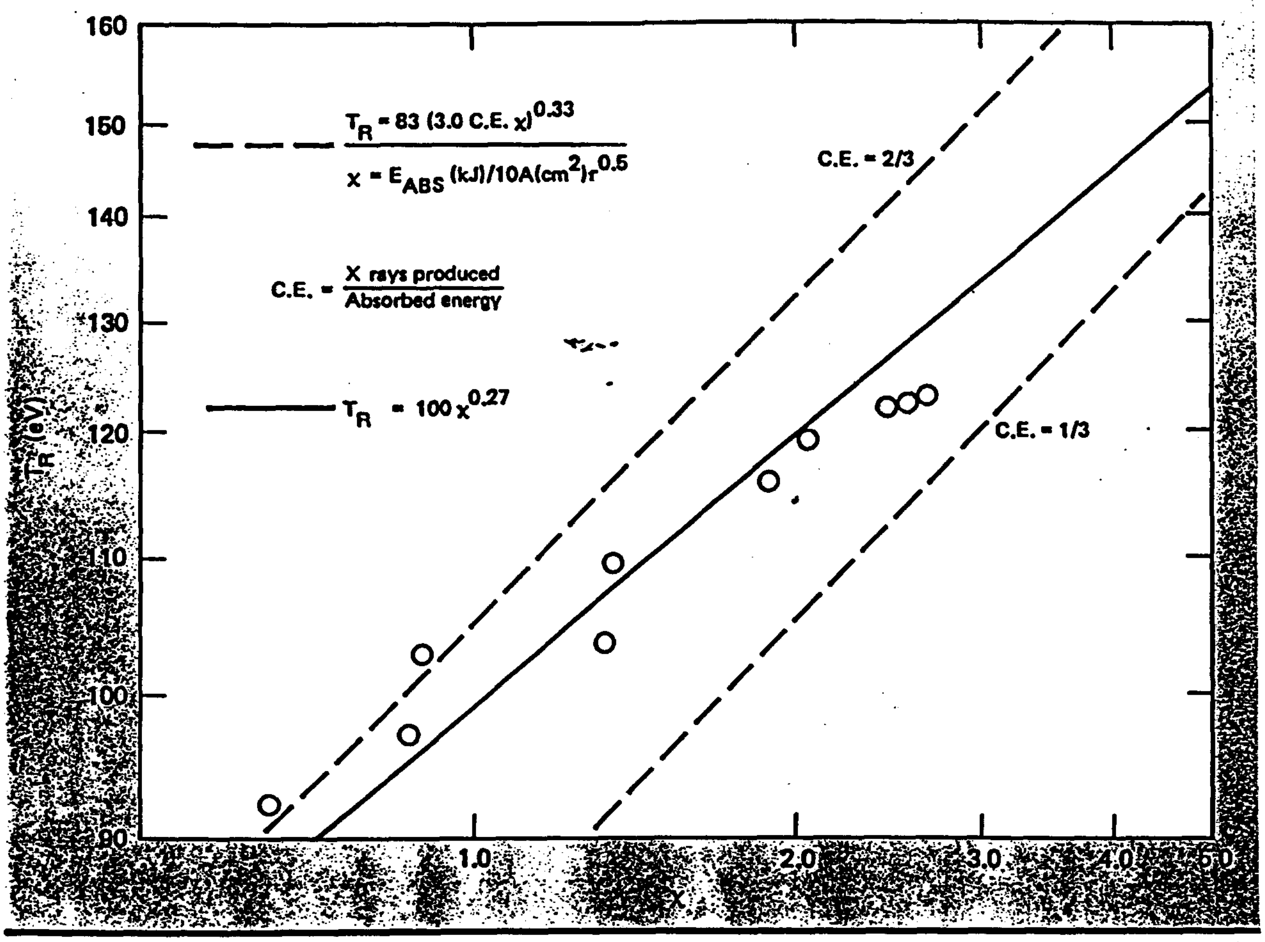

33. P. H. Y. Lee, D. T. Attwood, M. J. Boyle. E. M. Campbell, L. W. Coleman, and H. N. Kornblum, *Time-Resolved X-ray Spectra of Laser-Irradiated High-Z Targets*, Lawrence Livermore National Laboratory, Livermore, Calif., UCRL-79783 (1978).

34. *Laser Program Annual Report—1978*, Lawrence Livermore National Laboratory, Livermore, Calif., UCRL-50021-78 (1979), p. 5-22, Sect. 5.5.2.

Cairn Hohlraum Scaling Study—Analysis of Two-Nanosecond Experiments

In analyzing these experiments, we will argue that plasma phenomena occurring between one tenth and one quarter critical density have a dramatically increased effect in closed geometries, as compared to open geometries. The properties of these phenomena, including the Raman and $2\omega_{pe}$ instabilities, are important in explaining both the number and high energy of suprathermals in a laser-driven hohlraum. This view of the hot-electron problem in hohlraums is used to arrive at scaling laws for the number of suprathermals as a function of laser energy, pulse length, wavelength, and hohlraum size.

Fig. 5-90. Radiation temperature vs Marshak wave-scaling parameter for 2-ns hohlraum experiments on Shiva and 600-ps experiments on Shiva and Argus.

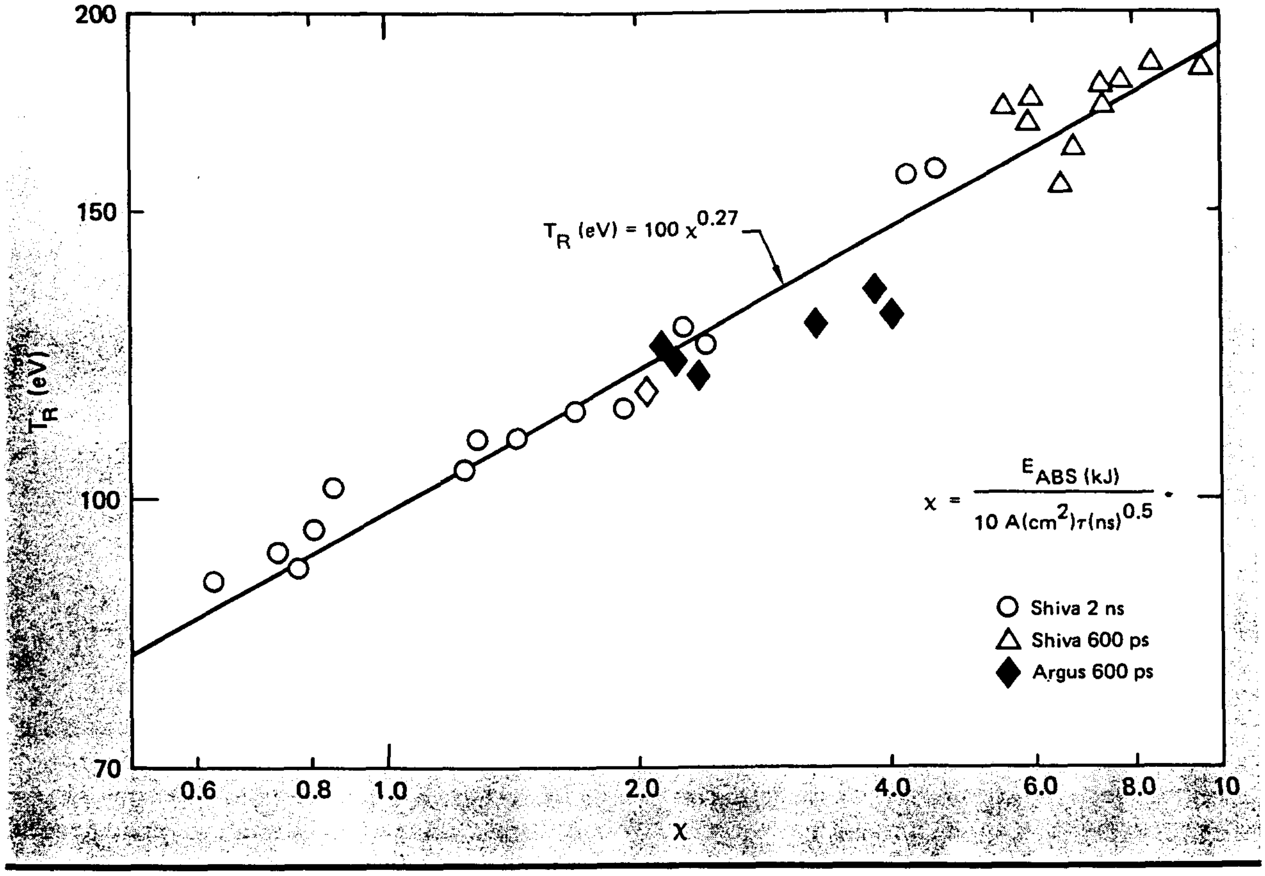

The critical features of laser-driven hohlraums for inertial-confinement fusion (ICF) are laser absorption, hole closure, the thermal x-ray fluxes or temperatures produced, hot-electron generation, and x-ray flux uniformity for capsule implosions. Over the past three years, we have had substantial success in achieving laser absorption of about 80% and in demonstrating that hole closure is a soluble problem for subnanosecond pulses. We have also been able to accurately predict hohlraum temperatures, using x-ray conversion efficiencies measured on disks. The major discrepancy between an open disk and a closed geometry has been the number and energy or temperature of the hot electrons.

The experiments at 2 ns have allowed us to extend the data to the longer-pulse, lower-intensity regime in which Nova targets will operate. They also provide the first systematic data on hot-electron variation as a function of energy and hohlraum size.

Measured thermal x-ray temperatures for the 2-ns experiments are consistent with Marshak wave-scaling (Fig. 5-89) using x-ray conversion efficiencies measured on disks and imply an x-ray conversion efficiency proportional to intensity $I^{-(0.15-0.20)}$.

The dashed lines in Fig. 5-89 show hohlraum radiation temperature as a function of the Marshak scaling parameter $X = E/A\tau^{1/2}$ for constant conversion efficiencies of one- and two-thirds. Here E is the laser energy absorbed in kilojoules, A is the wall area of the hohlraum in square centimetres, and τ is the laser pulse in nanoseconds, following the analysis of M. Rosen.[37] The data clearly cut between these two curves. The points below X = 1 are experiments for which the first-bounce intensity inside the hohlraum is 3 to 5 × 10^{13} W/cm^2. At these intensities, 2-ns pulses on gold disks result in approximately 60% conversion of laser light to x rays, consistent with the x-ray conversion efficiency necessary to explain the hohlraum temperatures. For $\chi > 5$, disks have a conversion efficiency of 33 to 40%, again consistent with the hohlraum temperature. LASNEX calculations also predict an intensity dependence of the conversion efficiency proportional to $I^{-(0.1-0.2)}$, depending on the modeling.

If we assume that conversion efficiency scales as $I^{-0.18}$ and is equal to one-third at $I = 3 \times 10^{14}$ W/cm^2, the Marshak wave analysis gives the solid curve in Fig. 5-89. Figure 5-90 extends these data to include the 600-ps Cairn data from Shiva and the 600-ps data for half-Cairns on Argus. All of these data fit the Marshak wave analysis, using an intensity-dependent conversion efficiency of $I^{-(0.15-0.20)}$.

To match the experimentally inferred hohlraum temperature of 250 to 300 eV, the wall losses have to be increased a factor of two to three above that which would occur with the XSNB opacities. Various mechanisms have been proposed to explain this loss, including a thirtyfold reduction of opacity, or fluid instability on the hohlraum walls. If the disk modeling inside laser-driven hohlraums is correct, there is no such increased loss at 200 eV on Shiva. We must point out, however, that the number of x rays actually produced inside a laser-driven hohlraum is not really measured. Further, two-thirds of the energy is not converted to x rays in the disk model at the incident laser intensities required to produce 200 eV on Shiva. This energy is ignored in the Marshak wave analysis, and it may be fortuitous that such an analysis agrees with the data. At temperatures of about 100 eV, the situation is clearer. Since a conversion efficiency of two-thirds matches the data, XSNB opacities must also be near the calculated values.

Detailed analysis of the hot-electron production in a hohlraum produces numerous uncertainties because we have no direct experimental measure of the number of hot electrons or their temperature. The high-energy x-ray-detection techniques used with good results in open geometries are more uncertain for the hohlraums because of spectral attenuation effects caused by the gold case, which strongly affect all x rays much below about 50 keV. Nonetheless, several observed characteristics can be used to reach a preliminary conclusion about the mechanisms responsible for producing the superthermal electrons and to suggest scaling relations for their numbers and energy.

1. Data from the high-energy x-ray streak camera show that the temporal width of the emission is narrower than that of the laser pulse and that the onset of hard x rays is increasingly delayed, relative to that of the soft x rays, as the level of hard x-rays drops.

2. Zone-plate images from the Heinz series[38] are consistent with a production mechanism that is primarily a volume-production process rather than a hot-spot emission.

3. The level of Raman backscatter measured in hohlraum experiments is orders of magnitude higher than that on disks and has been measured to be at several percent of the incident laser energy for Cairns on Argus. This puts a lower level on the fraction of light affected by the Raman process. Most of this light would never get outside the hohlraum because the reflected wave is near its critical density if it is produced near quarter-critical density for one-micron light.

A variety of effects could cause the observed difference between closed and open geometries. Raman instability, decay of the incident electromagnetic wave into a plasma wave and a backscattered electromagnetic wave, occurs up to quarter-critical density for the incident wave. The number of spatial e-foldings Q_R for this instability is given by

$$Q_R = 2\pi(10^{-3})\left(\frac{\alpha 2}{\alpha - 1}\right) I_{16}\lambda(\mu) L(\mu) \quad , \tag{8}$$

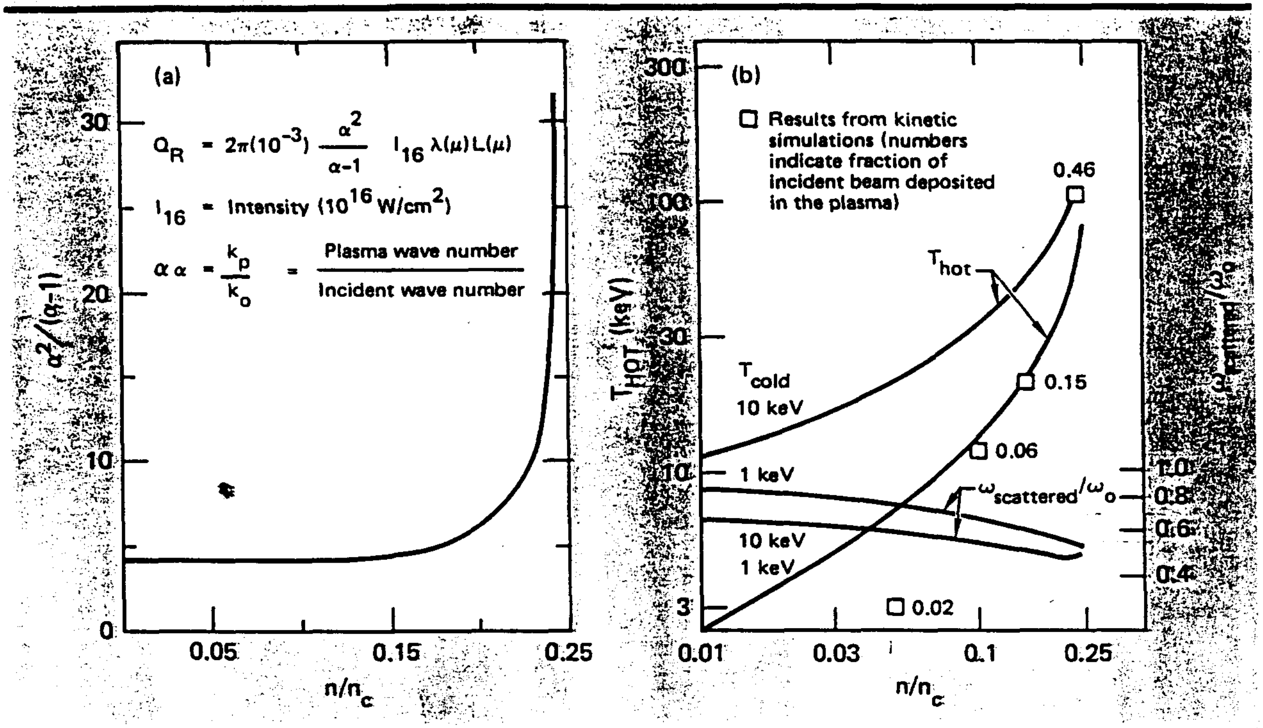

Fig. 5-91. (a) Raman quality factor. (b) Theory and simulation results of stimulated Raman scatter. $T_{hot} \approx \frac{m_e}{2}\left(\frac{\omega^2}{k^2}\right)$ increases with density and cold-electron temperature. Frequency of scattered light decreases with increasing density.

where $\alpha = k_p/k_0$ and is the ratio of the wave number of the plasma wave to that of the incident electromagnetic wave. $\alpha^2/(\alpha-1)$ is plotted in Fig. 5-91(a). I_{16} is the laser intensity in units of 10^{16} W/cm^2. Because of the large dimension of underdense plasma, the number of spatial growth lengths for Raman can start to become significant even at very low densities. For example, at $n/n_c = 0.1$ and $I = 10^{15}$ W/cm^2 for $L = 2000\mu$, $Q_R \sim 5.5$. However, as seen in Fig. 5-91(b) from Estabrook,[39] only about 6% of the light involved in the Raman instability at $n/n_c \sim 0.1$ ends up in the plasma. Further, the T_{HOT} of this energy is fairly low. T_{HOT} from Raman sidescatter could be up to a factor of $\sqrt{2}$ larger. However, the situation changes qualitatively near $n/n_c = 0.25$. There α is approximately equal to 1, and the instability becomes absolute. The growth length can be estimated by $\ell = c\gamma$, where c is the speed of light and $\gamma = K_e V_{os}/4$ is the growth rate for Raman. This gives $\ell \sim 20\mu$ to 50μ. If this number were off by an order of magnitude, Raman would still have a large effect if a substantial volume of the hohlraum fills to quarter critical. Further, half the energy of the incident light ends up in the plasma as high-energy electrons with a temperature of 40 to 100 keV (Fig. 5-91(b))—a temperature that is dependent only on the kinetic wave matching conditions. This would be seen in the hohlraums as a marked increase in the number and energy of hot electrons when a large fraction of the volume reached quarter critical.

The $2\omega_{pe}$ instability, decay of the incident electromagnetic wave into two plasma waves, occurs for $0.2\,\rho_c < \rho < 0.3\,\rho_c$. This instability has a very large growth rate and produces very energetic electrons, with spectra comparable to or hotter than that of Raman near quarter critical. It does not produce a large number of superthermals in open geometries because it is easily saturated by steepening of the density profile near quarter critical, thus removing the area of instability. But in a closed geometry, with a large volume near quarter critical, it can be an effective mechanism for generating electrons.

Laser-beam filamentation is another mechanism for producing very energetic electrons.

Fig. 5-92. (a) LASNEX zoning for 3.0-scale Cairn hohlraum irradiated by 2-ns pulse with 6-kJ incident laser energy 100 ps before peak of pulse. (b) Trajectory of light for inner and outer beam clusters on Shiva 100 ps before peak of pulse. (c) Density contours 100 ps before peak of pulse. (d) Density contours 600 ps after peak of pulse.

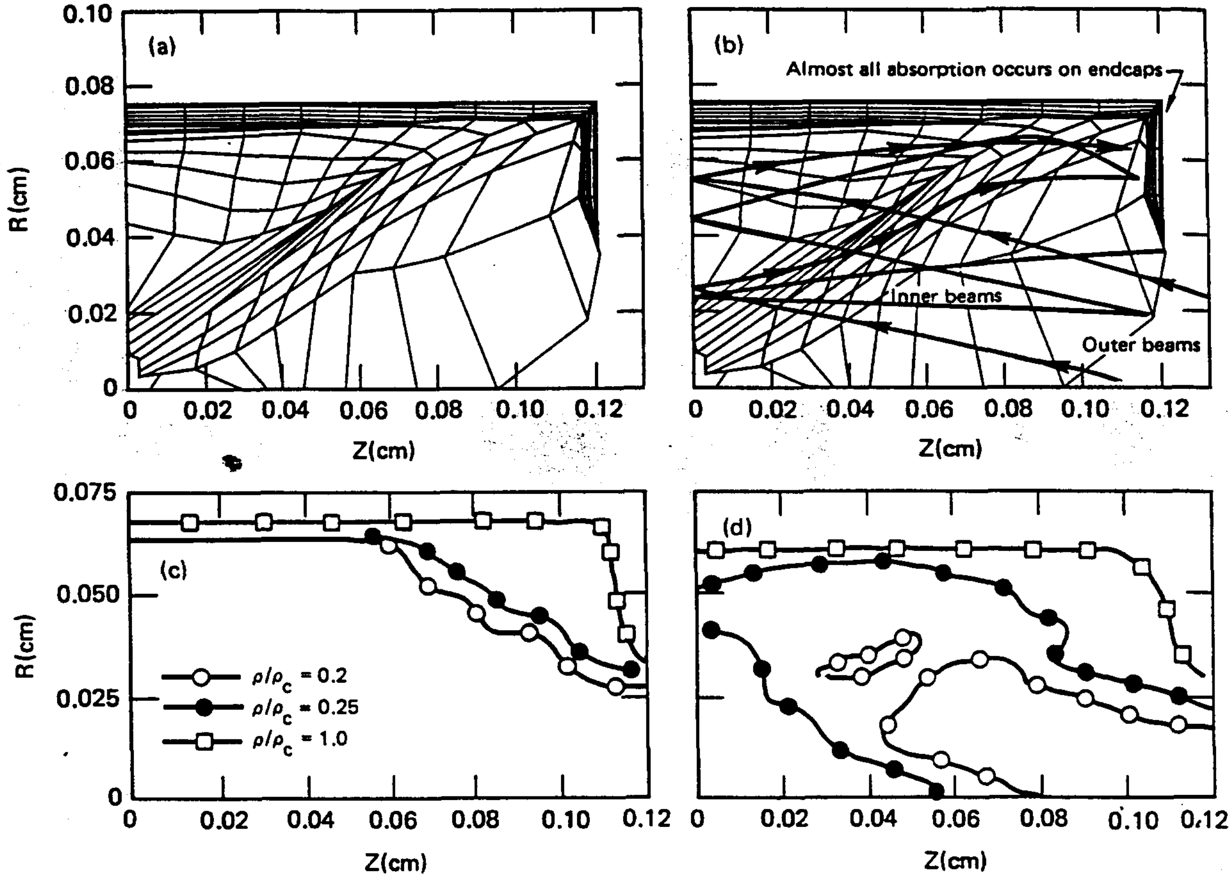

It starts with either an intensity fluctuation on the laser beam or a density fluctuation in the plasma. If local intensity increases, the increased light pressure expels plasma from that region, causing a local increase in the index of refraction. This, in turn, causes an intensification of the local light maximum.

The number of spatial growth lengths Q_f for this instability is given by

$$Q_F = 4(n/n_c)\,(I_{14}/T_e)\,L\,(\mu)\,\lambda(n) \quad . \qquad (9)$$

This factor can be quite large in typical hohlraum situations. If we take $I = 5 \times 10^{14}\ \mathrm{W/cm^2}$, $n/n_c = 0.2$, $T_c = 4$ keV, and $L = 2000\ \mu$, the $Q_f = 20$. What happens here is that the beam filaments to high intensity (much higher than the incident intensity) and then travels through the hohlraum in the filamented state until it hits a critical density surface. Resonance absorption at the critical surface then produces more-energetic electrons than would have been expected because of the large intensification. Zone-plate images of the high-energy x rays do not show evidence of the high-contrast regions of emission that would be the signature of this process. In fact, enclosed geometries with high levels of suprathermal electrons show less constrast in high-energy x-ray emission than geometries with reduced levels of hot electrons.

Finally, if the hohlraum fills above critical density, the laser light is absorbed closer to the beam focus and the effective intensity increases. Since we do not measure density inside a hohlraum, this effect cannot be ruled out entirely; however, LASNEX calculations predict a density much less than critical. Also, the experiments show no

Fig. 5-93. Density contours vs time for one-dimensional, cylindrical LASNEX calculation (3.0-scale hohlraum irradiated by 2-ns pulse with 6-kJ incident laser energy).

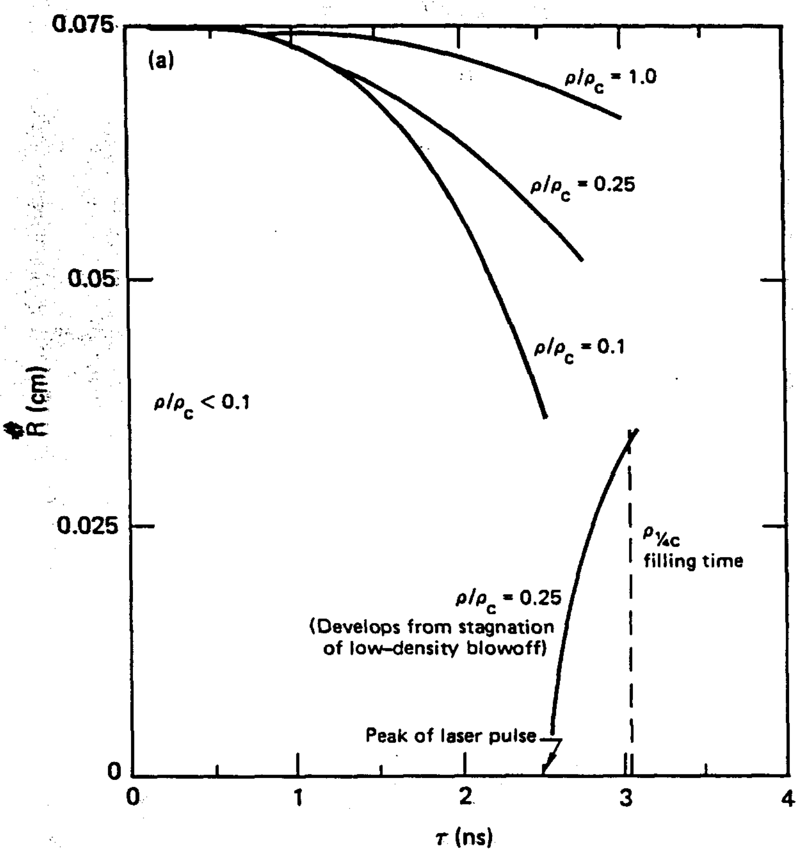

evidence of closure, such as reduced absorption for longer pulses.

We will concentrate on quarter-critical phenomena because they fit the qualitative features of the observed hohlraum hot-electron production. Theoretically, they have a dramatic onset near quarter-critical density. Also, LASNEX calculations predict that most of the hohlraums, although they do not reach critical density during the pulse, will reach quarter-critical density.

Although LASNEX does not yet model the plasma instabilities that occur at or near quarter-critical density, we can run a calculation until the channel fills to that density, using the energy remaining in the laser pulse at that time as a measure of the amount of energy that could be turned into hot electrons. Figure 5-92 shows the results of a two-dimensional LASNEX calculation for a scale-three hohlraum with 6 kJ incident energy in 2 ns. Figure 5-92(a) shows the LASNEX mesh in one-quarter of the cylindrical hohlraum, 100 ps before the peak of the pulse, and Fig. 5-92(b) shows the mesh with typical light-ray trajectories superimposed. The outer beams, which were focused onto the walls of the hohlraum, have an incident angle of 68° or more and a turning point at 0.14 n_c or less. Hence, there is almost no absorption on the hohlraum walls. The rays refract until they hit the end caps, where all of the absorption occurs. Because the Shiva beams are necessarily incident at a shallow angle in all Cairn geometries, absorption must occur on the end caps. Hence, the incident intensity is much larger than one gets from a mere projection onto the walls, and refraction effects start occurring at $n/n_c \sim 0.1$ or less.

Figure 5-92(c) shows the 0.2 and 0.25 ρ_c contours 100 ps before the peak of the pulse. Very little

Fig. 5-94. Experimental f_{hot} (assuming thick target bremsstrahlung at 50 keV) vs fraction of energy left in pulse at time of quarter-critical density ($1/4\,\rho_c$) filling (from LASNEX one-dimensional cylindrical calculations).

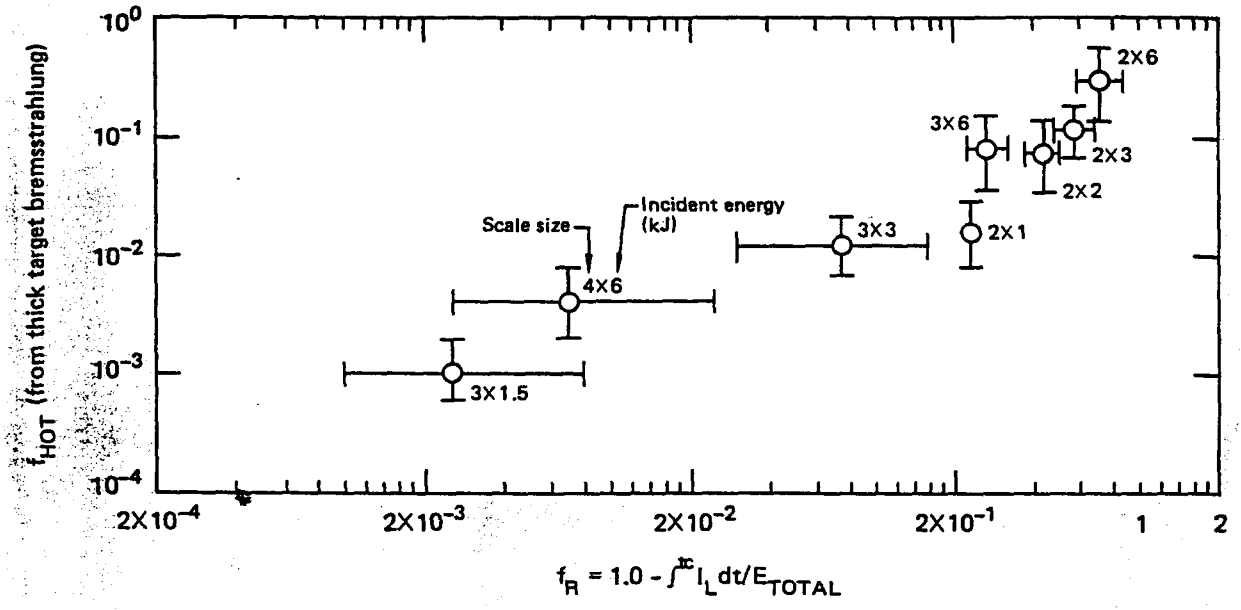

of the channel volume has filled to this density. Critical density is very near the original case-wall location. By 600 ps after the peak of the pulse, however, most of the total channel volume is near $1/4\,\rho_c$; see Fig. 5-92(d).

One obtains nearly the same $1/4\,\rho_c$ closing time from one-dimensional cylindrical calculations. Figure 5-93 shows the radius versus time history of the $\rho = \rho_c$, $\rho = 0.25\,\rho_c$ and $0.1\,\rho_c$ surfaces. At about the peak of the pulse, a second $\rho = 0.25\,\rho_c$ surface starts outward from the axis as the blowoff stagnates and accumulates. Between 300 and 600 ps after the peak of the pulse, all of the incident beam energy would intersect large volumes of plasma near quarter-critical density. The timing is very near that of the two-dimensional problem.

To determine the number of suprathermal electrons in the various hohlraums, we make a number of assumptions that will necessarily make the answer crude. First, since all of the spectra are qualitatively similar in shape, although their amplitudes vary by more than three orders of magnitude, we assume that the temperature of the hot electrons is the same in all cases. Second, we assume that the spectrum of the superthermal tail is approximated by a Maxwellian distribution and that the number of hot electrons can be inferred by assuming that the x rays we measure are produced by thick target bremsstrahlung from this electron spectrum. Then, we can use the formula

$$E_{hot}(\text{Joules}) = \frac{E(h\nu = T_{hot})\,(\text{keV/keV}/4\pi)\,(79/z)}{5 \times 10^{11}} \qquad (10)$$

utilizing the 4π x-ray fluence at the hot-electron temperature. We only have three experimental points on the spectrum: 47 to 54 keV, 61 to 69 keV, and 80 to 88 keV. The point from 61 to 69 keV has gold fluorescence lines in it and must be discounted in determining a temperature from the x-ray slope, leaving little information from which to infer a temperature. We expect a temperature of 40 to 100 keV from the Raman instability, near $\rho = 1/4\,\rho_c$ and we have used the level of the 47-to-54-keV channel to infer a fraction of energy in hot electrons. A slope through the 47-to-54-keV channel and the 80-to-88-keV channel gives a temperature of 20 to 30 keV for most of the 2-ns spectra. If the temperature is lower than 50 keV, the number of hot electrons will be higher than had been inferred from the 50-keV point. Using this procedure, Fig. 5-94 gives the inferred fraction of the laser energy in hot electrons, f_{hot}, for each hohlraum versus the fraction of energy left in the laser pulse f_R at the LASNEX-calculated $1/4\,\rho_c$ closing time. The ordering of data points in

Fig. 5-95. High-energy-electron time delay vs energy for 2.0-scale hohlraum (2-ns pulse).

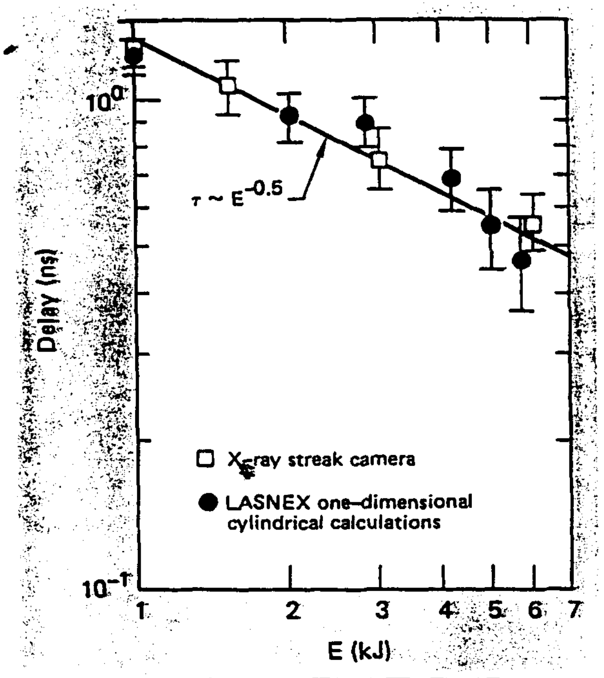

Fig. 5-96. LASNEX quarter-critical closing time ($\tau_{1/4}$) vs scale size for 6 kJ incident laser energy.

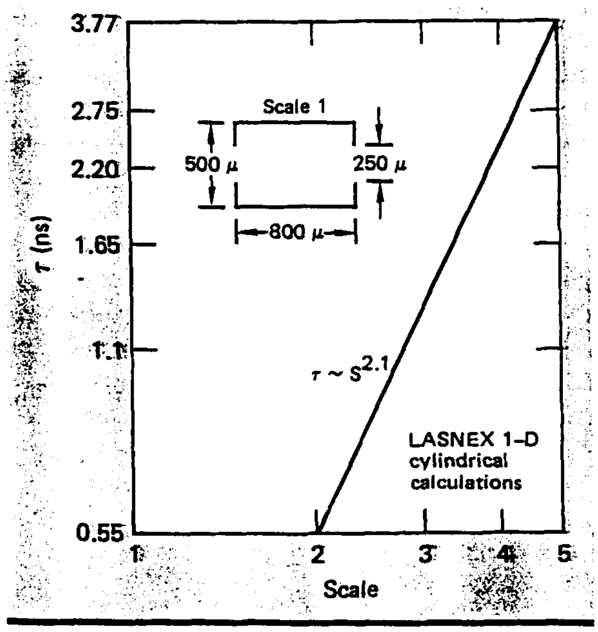

Fig. 5-94 is consistent with the model discussed here. The error bars on the f_R represent the difference in energy determined between the time the $1/4\ \rho_c$ surface has filled to one-third and one-half of the radius in the one-dimensional calculations.

We have obtained data from the high-energy, x-ray streak camera to support the hohlraum filling closing hypothesis. On most shots, the streak camera viewed the hohlraum through a laser entrance hole. The lower energy channels and an unfiltered channel could view the early onset of low-energy x rays, while the silver channel, which was sensitive to x rays mainly above 25 keV, showed a delayed response. The time delay between the half heights of the low energy x-ray signal and the silver channel versus incident laser energy for the scale-two series is plotted in Fig. 5-95. Also plotted are the delays between the half height of the laser pulse and the $1/4\ \rho_c$ closing for one-dimensional LASNEX calculations. The agreement is excellent and shows a time delay $\tau \sim E^{-0.5}$. We did not obtain data for all of the scale-three series, but LASNEX calculations show a similar scaling as a function of incident energy. One can also keep the energy constant, but vary hohlraum size. Figure 5-96 plots the LASNEX delay times versus hohlraum scale size, showing that $\tau_{1/4} \sim S^{2.1}$. This gives a scaling of $\tau_{1/4} \sim (S^2/E^{1/2})$.

One can obtain a similar scaling for an isothermal blowoff. Below critical density, the laser heats the blowoff to near isothermal conditions. The time required for sufficient material to accumulate to reach $1/4n_c$ scales as $\tau_{1/4} \sim S/V_s$, where V_s is the isothermal sound velocity. If $V_s \sim (Z\,T_e)^{1/2}$ and $Z \sim (T)^{1/2}$, then $V_s \sim T^{3/4}$. If the temperature is determined by the electron flux limit, then

$$I \sim n_c\theta V_e \sim n_c\theta^{3/2} \sim (1/\lambda^2)\theta^{3/2} \quad , \qquad (11)$$

$$\theta \sim (I\lambda^2)^{2/3} \quad , \qquad (12)$$

$$V_S \sim (I\lambda^2)^{1/2} \quad , \qquad (13)$$

and

$$(\tau_{1/4}/\tau_L) \sim \frac{S}{(I\lambda^2)^{1/2}\tau_L} \sim \left(\frac{S^4}{\lambda^2 E\tau_L}\right)^{1/2} \quad , \qquad (14)$$

where τ_L is the laser pulse length. For closure times at the peak of the pulse or later, the fraction of energy left in the laser pulse is proportional to the error function and scales approximately as

Fig. 5-97. Plots of f_{hot} vs (a) S^4/Et and (b) S^3/Et for 2-ns Cairn experiments on Shiva.

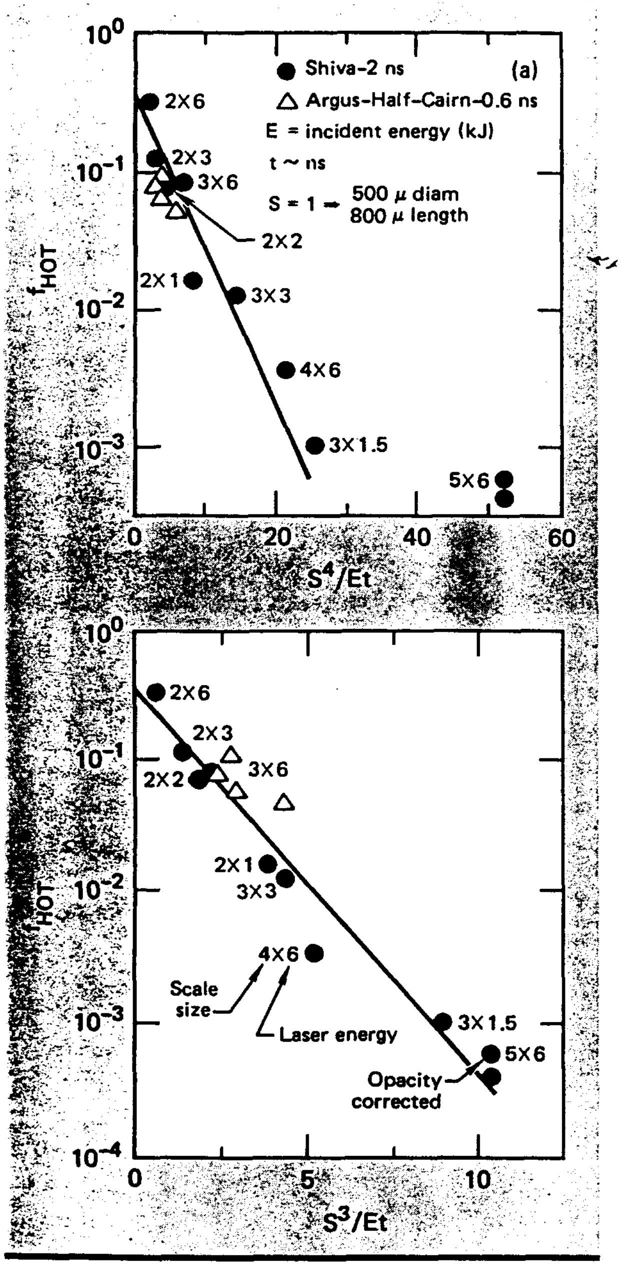

$\mathrm{EXP}(-\tau_{l/4}^2/\tau_L^2)$. Figure 5-97(a) is a semilog plot of f_{hot} versus S^4/E for the various 2-ns experiments. The data are not convincing enough to choose between an S^4/E and an S^3/E scaling, as shown in Fig. 5-97(b).

The above argument also has f_{hot} scaling as $1/\tau_L$ and $1/\lambda^2$. In other words, more energy can be put into a hohlraum with a given level of hot electrons, at either shorter wavelength or shorter pulse length. We should be able to test the shorter-wavelength hypothesis on Argus at 0.53 μm at the current level of 35 J. Pulse-length scaling is more complicated. Although shorter pulses would result in less filling, the intensities are increased and the inherent geometric focusing of a hohlraum provides further intensification. Longer-pulse operations using one of the hohlraums with relatively low levels of superthermal electrons, such as a scale-three or -four hohlraum at 6 kJ would probably provide a better test of pulse-length scaling. In Fig. 5-97, we have placed points for the half-Cairn experiments on Argus at 600 ps and 800 J, scaled as S^3/Et and S^4/Et. Although they seem to fit reasonably well on the curves, more data are needed. Also, until more-direct evidence of certain key quantities such as hohlraum density, hot-electron temperature and hot-electron number are obtained, we must rely on tenuous inference. Settling this hot-electron scaling issue is important because of its implication for future laser systems. The hohlraum radiation temperature scales as $(E/S^2\sqrt{\tau_L})^{1/3}$. If the hot-electron fraction scales more rapidly with size, energy, and pulse length than this, one can increase the driving temperature for a given f_{hot} as the size of the hohlraum increases. Also, if f_{hot} scales as $1/\lambda^2$, shorter wavelengths also reduce f_{hot} at a given size and radiation temperature. So far, the data are incomplete, but they bode well for Nova with a green-light conversion capability and for short-wavelength reactor drivers.

Author: J. D. Lindl

References

37. See "Theoretical Modeling" in Section 2 of this report.
38. See "Suprathermal Electron Generation in Laser-Fusion Target Geometries" earlier in this section.
39. LLNL Laser Fusion Monthly, Lawrence Livermore National Laboratory, Livermore, Calif., MM 79-6 (1979).

Investigations of ICF Target Physics: Preheat, Shock, and T_R Scaling Experiments with Half-Cairn Hohlraums

Introduction

The "Theoretical Modeling" section of this annual (see Section 2) shows that, from first principles, we can derive simple scaling laws (1) for the radiation temperature in a laser-irradiated hohlraum and (2) for the radiatively driven shock in a pusher material, to mention just two of many laws derived there. Here we compare all those predictions with 1979 experiments on Argus and Shiva and, in general, find excellent agreement between theory and data.

Fig. 5-99. Radiation temperature T_r vs the figure of merit for Marshak-wave wall penetration: $E_{abs}/A_W\tau^{0.5}$. Solid line is the theoretical prediction.

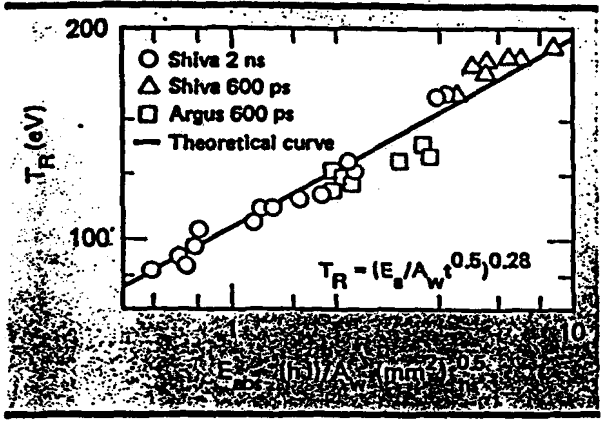

T_R Scaling

Equation (21) of "Theoretical Modeling" (see Section 2) states that

$$T_r \sim (E_A/A_W\,\tau^{0.5})^{0.28} \qquad (15)$$

In Fig. 5-99, we compare this prediction with data taken on both Shiva and Argus. The laser pulses varied from 600 ps to 2 ns in length and from 600 to 6 kJ in energy, and the hohlraum scale sizes varied from 1.2 (wall area of 2 mm^2) to 5.0 (wall area of 40 mm^2). Over this broad range of parameter space (factor of 15 in the $E/A\tau^{0.5}$ figure of merit), the T_R formula seems to hold quite well; however, certain caveats should be restated.

The theory leading up to the T_R formula does not include realistic time dependence (such as the Gaussian nature of the laser pulse), which could introduce a serious systematic error. STE contributions to wall heating are not included, which makes the upper part of the curve of Fig. 5-99 suspect since there, typically, $E_{rad} \approx E_{sup} \approx 1/3\ E_{abs}$. Finally, as shown in "Theoretical Modeling," (see Section 2), other losses (diagnostic hole and ball) that lower T_R somewhat (typically a few electron volts) are not included in the simple formula presented here. The experimental points are determined by measuring

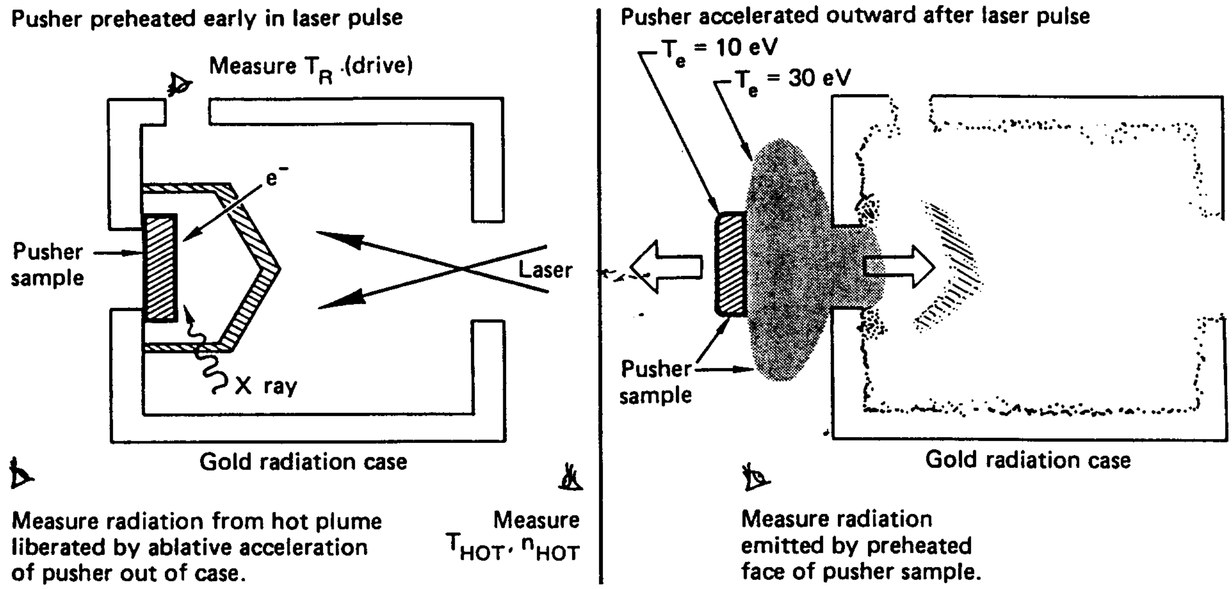

Fig. 5-100. Half-Cairns relate drive conditions (T_R, E_h, and T_h) to pusher-sample response. Early in time, the pusher is preheated and then shocked. Late in time, the "cork pops" out of the can, releasing hot radiating gas.

radiation flux emitted from a diagnostic hole in the target can. Since these holes are subject to closure, systematic errors may be introduced in the experimental determination of T_R. Nonetheless, the agreement between theory and experiment in Fig. 5-99 is quite impressive.

Half-Hohlraum Experiments

Two other aspects of classified-target performance covered in "Theoretical Modeling" (see Section 2) are (1) suprathermal electron preheat and (2) shock plus ablative acceleration driven by radiation. To test these issues we have used half-Cairn hohlraums, with test samples inside of them to mock up target-ball pusher material. These half-Cairns are shown schematically in Fig. 5-100. We monitor the drive, T_R, in the usual way and measure the suprathermal E_h and T_h from the hard x rays produced as the electrons stop in the gold case. Early in time, the cold side of the pusher (visible through a diagnostic hole in the end cap) is preheated by the suprathermals. Later, the pressure produced by the radiation drive on the front of the sample produces a shock which propagates through the sample, arriving at the back and heating it further. Because heated material radiates, we can detect these heating effects with soft x-ray detectors (Dante-L, 15 eV $\leqslant h\nu \leqslant$ 500 eV) and with optical streak cameras (blue and orange light). The Dante-L detector has 200- to 500-ps time resolution and is not spatially resolved. The optical camera is spatially resolved, has 15-ps resolution, and is calibrated absolutely to deduce the temperature of the emitting surface from the intensity of emission. Much later, the sample moves out of the diagnostic hole (the can "pops its cork"), releasing hot ablation plasma that radiates copiously and gives a large signal on both Dante-L and the optical streak camera.

We shot 800 J of Argus laser energy in a 600-ps FWHM pulse into a 1.4-size half-Cairn hohlraum that contained a 12.4-μm-thick sample of glass. The T_R measured was 120 eV (to be expected, see Fig. 5-99). Roughly 60 J (less than 10% of E_{abs}) went into a hot-electron spectrum of 70 keV. The lowest of five Dante channels and data from the optical streak camera's data are shown in Fig. 5-101. We see a preheat signal of one to two electron volts following the temporal behavior of the laser pulse, followed by about a 10-eV shock that rises sharply near the peak of the laser pulse. Finally, we see large "cork-popping" signals for each instrument. We now analyze each component separately.

Preheat. The work in "Theoretical Modeling" (see Section 2) showed how 100 suprathermal electrons with energy E_0, created in the primary of the

Fig. 5-101. Optical streak camera shows preheat, shock, and cork-popping. Dante, not as well resolved temporally, shows shock and cork-popping. Experimental conditions: 12.4-μ-thick glass sample in a 1.4-size half-Cairn; Argus laser pulse of 800 J for 600 ps; $T_R \approx$ 120 eV; $T_h \approx$ 70 keV; and $E_h \approx$ 60 J. The two instruments show different cork-popping times because of their differing lines of sight and different late-time temperatures because of different definitions (see text).

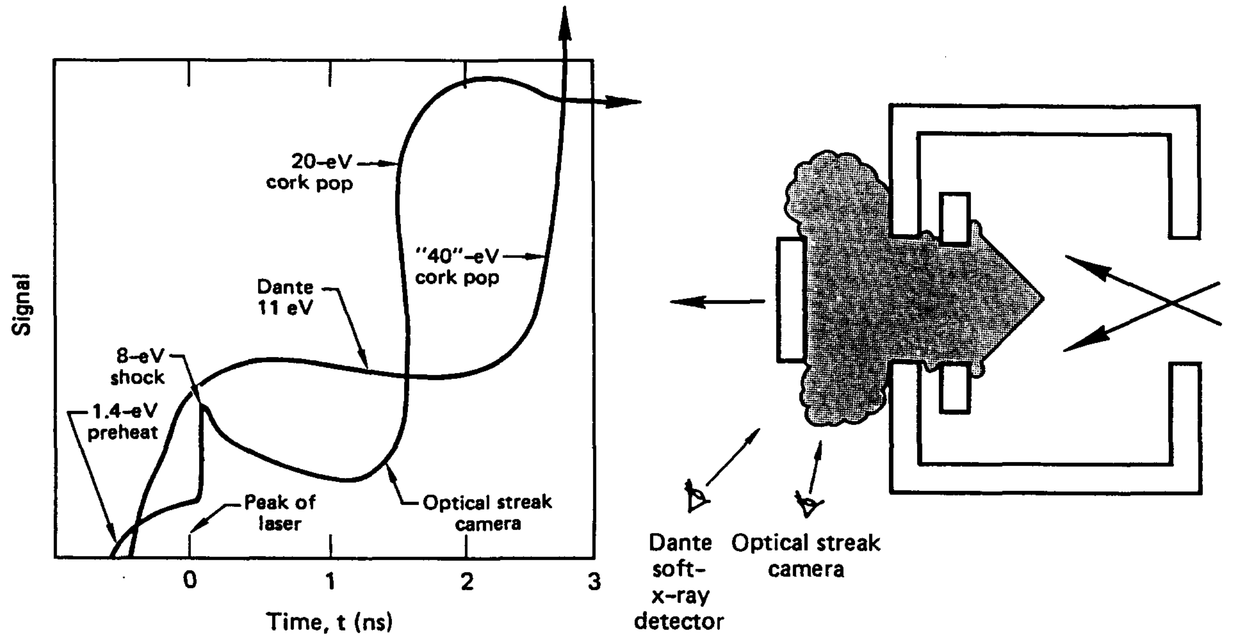

1.4-size half-Cairn, become 1.2 electrons with energy E_o and 0.8 electrons with energy 0.7 E_o deposited in the glass sample. Multiplying these numbers by 0.6 will give the conversion to joules since only 60 J were created in this experiment. We have derived formulae for the preheat temperature in a material, given T_h and E_h and the thickness of the material.[46] Combining the results there we have, for glass,

$$T_{ev}(0.8\,T_{ev}^{1/2} + 1) = \frac{7 \cdot 10^{-5}\,E_h(J)}{2\,A(cm^2)\,\lambda_h(cm)}\ , \qquad (16)$$

where λ_h for 70 keV is 60 and A is the sample area, 7×10^{-4} cm^2. This formula yields a preheat temperature of about three electron volts, within a factor of two of the measured value. The factor of two can be explained by noting that we only see the signal until the peak of the pulse (when the shock breaks through), thus only half of the suprathermal energy should be used in the calculation (30 J, not 60). This brings T_{ev} down to 1.5 eV, as observed.

Similar agreement can be found when analyzing the 1- to 3-eV preheat signals seen through 12- and 4-μ-thick gold samples in 1.6-size half-Cairns, which had even less energy in suprathermals (50 J). In the high-Z material, one must remember to effectively take half the temperature predicted from the ideal equation of state since the energy expended in ionization is typically as much as the ideal internal energy. One must also remember to include the gold sample's albedo in the "suprathermal-transport-around-the-cone" calculation. Otherwise, the analysis proceeds as before and predicts the experimentally observed signals.

One interesting feature of the gold preheat signals is their late arrival times—300 to 400 ps after the peak of the 600- to 800-ps FWHM pulse. At that late time, only 10 to 15% of the energy is left in the incident pulse. If 50% of that remaining energy were absorbed into the very hot electron spectrum observed, we would arrive at an E_h of 6% of the incident energy, which is precisely what is observed. This points to a scenario in which the can fills at late time to quarter-critical density. Under those conditions Raman instabilities can play a strong role in absorption and in the creation of very hot electrons. This scenario is studied in greater detail in "Cairn Scaling Study" (earlier this section). Before filling time, a "mere" 20-keV spectrum is produced, which would not significantly preheat the thick gold samples. However, such a "cool" spectrum would preheat glass samples to 10 eV, which may be one explanation for the 10-eV signal seen in Fig. 5-100. A radiation-driven shock may offer an alternative explanation.

Shocks. The magnitude and timing of the 5- to 10-eV shock observed near the peak of the laser pulse can also be explained in terms of previously discussed theoretical modeling. The radiation-driven ablation shock pressure, P_A, scales in glass as Eq. (22) of "Theoretical Modeling" (see Section 2).

$$P_A = 7\, T_{\mathrm{hev}}^{3}\, \tau_{\mathrm{ns}}^{-.43}\ \mathrm{MB} \quad . \tag{17}$$

Under our present experimental condition (T = 1.2, τ = 0.6), we find a 15-Mbar shock produced in the glass by the radiative drive. For an ideal gas shocked to four times its initial density (strong shock relations, $\gamma = 5/3$) we find that

$$T_{\mathrm{ev}}\,(Z + 1) = \frac{A}{4\rho_0}\, P(\mathrm{MB}) \quad . \tag{18}$$

Thus, for glass ($Z \approx 0.8\,\mathrm{Tev}^{1/2}$) we find P_A = 15 implies T_e = 9.5 eV, in reasonable agreement with the 8- to 11-eV shock observed. Thus, the shock-magnitude prediction is as observed.

As for the timing of the shock, the strong shock relations relate the shock velocity V_s to the pressure P_a by Eq. (32) in "Theoretical Modeling" (see Section 2)

$$V_s^2 = 4P_A/3\rho_0 \quad , \tag{19}$$

giving $V_s = 3 \times 10^6$ cm/s in glass. Since the glass is 12 μ thick, the shock takes 400 ps to traverse it. Because this is less than the FWHM of the pulse, we expect the shock to arrive at the back of the glass near the peak of the pulse, as observed.

We have seen preheat and shock signals in gold samples as well; see Fig. 5-102. For radiation drive into gold, the pressure scales somewhat differently [Eq. (27) of "Theoretical Modeling" (see Section 2)], yielding a 6-Mbar shock in gold (T = 1.2, t = 0.8). Equation (19) predicts a shock speed of 6×10^5 cm/s. This shock would propagate through 12 μ of gold in two nanoseconds, and the strength of the shock [Eq. (18)] would be about 3.5 eV, as observed.

Thus, for both glass and gold, the strength and timing of the shocks confirm experimentally the important radiation-driven pressure-scaling laws derived in "Theoretical Modeling" (see Section 2).

Fig. 5-102. Preheat (late arrival) and shock (very late arrival) signals through a 12-μ-thick sample of gold.

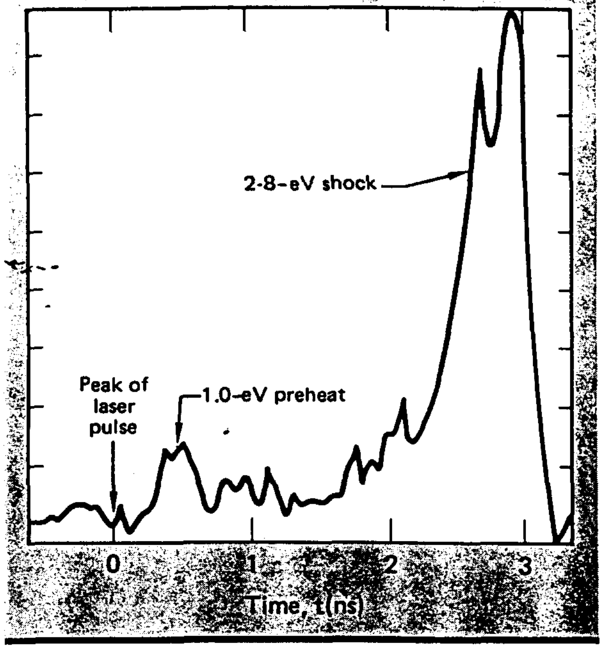

Ablative Acceleration. The final signal components in Fig. 5-101 are late-time "cork-popping" signals; as the sample is pushed out of the hohlraum, it liberates hot ablation plasma that radiates copiously. This process is quite complex since the hot plasma cools as it expands and radiates. However, as a simple model of the process, we predict a cork-popping signal will arise when an instrument's line of sight just clears the edge of the popping disk and is able to see the center of the now-vacated diagnostic "exit" hole. Thus, a Dante looking at 45° to the normal sample will see the cork-popping signal when the 100-μm-radius disk moves 100 μm out from the exit hole. In contrast, the optical streak camera, which looks at 55° from the sample's normal, will see the signal sooner since the disk must move only 70 μm out from the exit hole for the streak camera to see past it into the center of the exit hole. The speed of the popping cork has been calculated via a simple model (see "Theoretical Modeling" in Section 2). There, Eqs. (34), (35), and (20) imply (for glass) that

$$V_P = \frac{P_A(\mathrm{MB})\,\tau_L}{\left[P_0(\Delta x)_0 - 910^{-4}\,T^{2.25}\tau^{.57}\right]}\ \mathrm{cm/s} \tag{20}$$

where τ is in nanoseconds and T is in kiloelectron volts. The denominator simply corrects for the fact that just the unablated portion (the cork) of the sample is popped. Putting in $P_A = 15$, $\tau = 0.6$, $T = 1.2$, $X_o = 12.4 \times 10^{-4}$ cm, we find $V_p = 5 \times 10^6$ cm/s. Thus the optical streak camera should see the popping signal at 70 µm/5 × 10^6 cm/s, or 1.4 ns after the peak of the pulse, while the Dante should see the signal at 100 µm/5 × 10^6 cm/s, or 2 ns after the peak of the pulse. Comparison with Fig. 5-101 shows that these predicted times are as observed.

The "temperatures" that the two detectors observe can also be explained. As will be shown later, the LASNEX code predicts that the temperature of the hot liberated gas is about 20 to 30 eV. The spatially resolved optical streak camera confirms this prediction (see Fig. 5-101). The hot liberated gas is opaque and expands so that its surface area is much larger than that of the exit hole. The Dante detector, which is not spatially resolved, sees the entire plume, and the radiation it detects is that of a 20- to 30-eV blackbody radiating over a large area (compared to the exit hole). However, as a formal way to quantify its signal, the Dante temperature quoted ("40 eV") arbitrarily presumes that this large amount of detected radiation is emitted solely from that small area of the exit hole. Hence, it "must" have been so hot (40 eV) to emit so much from such a small hole. In reality, it is cooler but emits from the larger area. Thus, the quoted temperature of 40 eV does not disagree with the 20-eV result from the optical measurement. On the contrary, it supports the same physical picture of a large, 20- to 30-eV opaque plume of liberated ablation gas.

The agreement of the predicted cork-popping times with experiment adds even more credence to the simple scaling laws (for T_R, P_A, and V_p) on which the predictions were based. As a final check, we present detailed LASNEX calculations of these half-Cairn experiments, which agree both with these simple theories and with the data.

LASNEX Simulations

Figure 5-103 is a schematic portrayal of a one-dimensional LASNEX study of the half-Cairn experiments. The correct amount of laser energy impinges on the gold end cap of a cylinder, whose other end cap is the glass sample. The radiation temperature produced by the code is indeed 120 eV, as observed in the experiment and as predicted by the theory. We put 60 J of hot electrons (70 keV temperature) into the calculation, as observed in the experiment. However, since the one-dimensional zoning does not include the shadow-shielding effects of the scattering cone, we reduce the 60 J to 20 J. Also shown in Fig. 5-103 is the time history of the temperature at the back (cold side) of the glass

Fig. 5-103. (a) Setup for one-dimensional LASNEX study of half-Cairn experiments. (b) T_e vs time at back of glass samples. Preheat and shock signals compare favorably with the experimental results of Fig. 5-101.

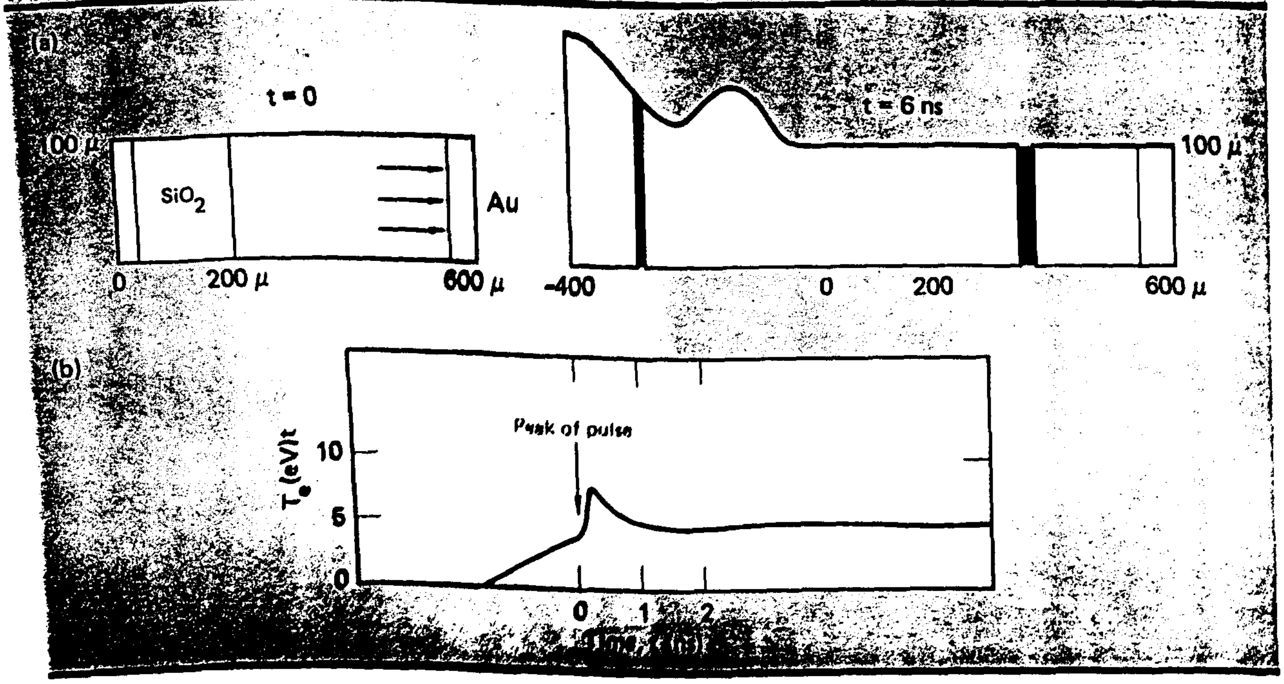

Fig. 5-104. LASNEX one-dimensional calculation of cork-popping motion, showing dense part of sample moving 5×10^6 cm/s, as predicted by theory and inferred from experiment.

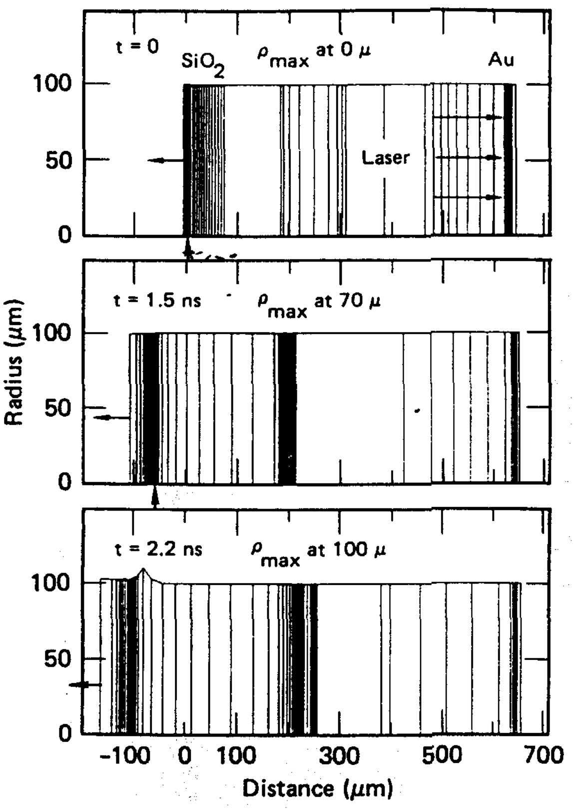

sample, as predicted by LASNEX under these conditions. There is a clear 2- to 3-eV preheat signal followed by an 8-eV shock near the peak of the pulse, as observed experimentally and as predicted by the theory presented here. Figure 5-104 shows the "cork-popping" motion of the sample. Indeed, at 1.5 ns the sample has moved out 70 μm, and at 2.2 ns it has moved out 100 μm. These numbers are essentially the same as those inferred from the cork-popping signals of the two detectors (Fig. 5-101), as well as from the simple theory. Figure 5-105 shows a two-dimensional LASNEX result that compares the time history of the lowest Dante channel with a TDG post-processor mockup of that channel according to LASNEX. Despite the complexity of the cork-popping process, the agreement of code and experiment is quite good. Note that both predict a temperature of "44 eV," despite the fact that (according to the two-dimensional LASNEX simulation) the emitting plasma has a temperature of only 25 eV. Recall that this difference in temperature results from the emitting area being much larger than the artificially presumed emitting area—namely, the exit hole.

Fig. 5-105. TDG post-processor to LASNEX simulates Dante channel with lowest energy and compares favorably with actual signal vs time.

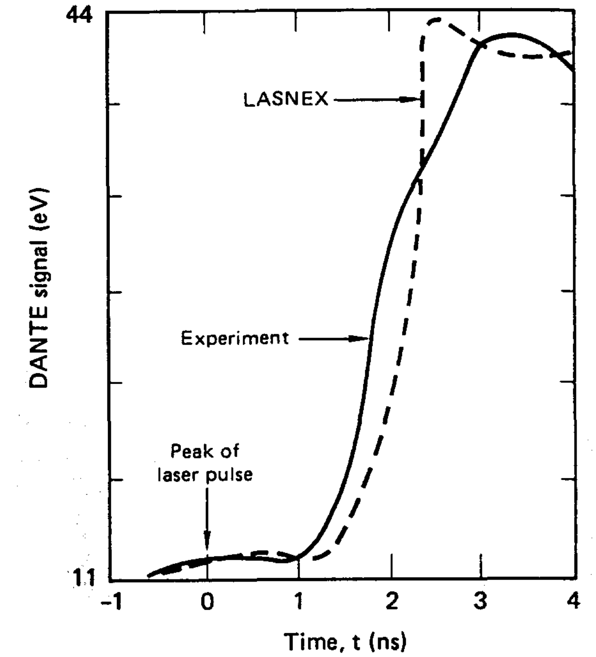

Summary

In conclusion, there is remarkable agreement between predictions of simple theory (and/or complex one- and two-dimensional LASNEX code work) and experimental data. The experiments are the first of their kind to measure shocks and ablative accelerations produced by soft x-ray drive. Together with the analysis presented here (based on the theory presented in "Theoretical Modeling" in Section 2), they will play a great role in the future in helping us to understand the physics of radiation-driven ICF targets.

Author: M.D. Rosen

Major Contributors: D. Phillion and G. Tirsell

References

46. M. D. Rosen, *Laser Program Annual Report—1979*, Lawrence Livermore National Laboratory, Livermore, Calif., UCRL-50021-79 (1980), p. 3-6 to 3-10.